# FIRST PRINCIPLES ELECTRONIC STRUCTURE CALCULATIONS OF $BaF_2$ AND GENERATION OF PARAMETRIZED POTENTIAL FOR MOLECULAR DYNAMICS STUDY OF THE SUPERIONIC PROPERTIES OF c-$BaF_2$

BY

PHILLIP W. OTIENO NYAWERE

B.Sc.(Kenyatta University), MPhil (Moi University)

A THESIS SUBMITTED IN PARTIAL FULFILMENT OF THE REQUIREMENTS OF THE DEGREE OF DOCTOR OF PHILOSOPHY OF UNIVERSITY OF ELDORET

Kenya.

OCTOBER, 2013

## DECLARATION

This thesis is my original work and has not been presented for a degree in any other university. No part of this thesis may be reproduced without prior written permission of the author and/or University of Eldoret.

**Phillip W. Otieno Nyawere**

SC/PhD/P/06/08

Signature: ..... Date: .....

## APPROVAL BY SUPERVISORS

This thesis has been submitted to the School of Science, University of Eldoret with my approval as supervisor.

**Prof. George O. Amolo,**

Department of Physics,

University of Eldoret,

Eldoret, Kenya.

Signature: ..... Date: .....

**Dr. Nicholas W. Makau,**

Department of Physics,

University of Eldoret,

Eldoret, Kenya.

Signature: ..... Date: .....

# DEDICATION

Wife; Helen Adhiambo Otieno;

For loneliness while I was away doing research

Children; Faith Shemida Akoth and Caleb Shimron Oluoch;

My gifts from God

***LORD Jesus Christ who lifts common men from dust and makes them sit and dine with kings. To Him alone be ALL glory.***

# CONTENTS

## ABSTRACT

The electronic structure and defects of barium fluoride, $BaF_2$, have been studied using the denstiy functional theory, DFT and density functional perturbation theory, DFPT. Lattice parameter of 6.10 Å was calculated comparable to experimental value of 6.20 Å for the cubic phase. Orthorhombic and hexagonal phases also give values close to experimental. Band gap of 7.20 eV in this work appears closer to experimental value of 10 eV in comparison to other theoretical results. Phonons and phononic properties have also been investigated and are discussed in this work. Elastic contants of cubic, orthorhombic and hexagonal phases of $BaF_2$ are calculated and discussed and do show good comparison with both experiment and other calculations. Stability parameters are also presented for all the three phases. Calculations using *ab initio* methods to find the defect formation energy and vacancy migration energies in barium flouride have been done for both anion and cation. Interstitial and Frenkel defects have also been studied and their effect on the band gap width analyzed. Migration of an anion and cation was found to show good agreement with experimental data and migration paths were also considered. Anion migration energy is easiest in the $V_F\langle 100\rangle$ at 0.53 eV comparable to experimental value of 0.59 eV. Migration energies for anion in the other low index directions $V_F\langle 110\rangle$ and $V_F\langle 111\rangle$ were calculated as 1.17 eV and 1.15 eV, respectively. The migration energy was highest at 2.22 eV for the cation in the $V_{Ba}\langle 100\rangle$ direction, while the other paths were found to be unfavourable for the cation. It was found that the interstitial formation energies for cation and anion were 3.14 eV and -0.62 eV, respectively. Vacancy formation energies were 15.64 eV and 8.73 eV for the anion and cation, respectively. This is slightly higher than 8.34 eV for anion and 13.75 eV for cation in $CaF_2$. Frenkel defect energies were also determined at near and infinite distances and were found to be 8.11 eV and 18.78 eV for the anion and cation, respectively. Potential parametrization was also considered in this study and it was found to improve the previously used pair potentials in the molecular dynamics study of $BaF_2$. Molecular dynamics and thermodynamics properties were investigated using a classical inter-atomic force field parametrized using the forces, stresses and energies obtained from the *ab initio* calculations. Using the parametrized potentials developed in this study, the superionic properties of cubic $BaF_2$ were studied through the phase transition diagram (energy versus temperature), where it was found out that the superionic transition of $BaF_2$ occured at about 1000 K, while melting temperature was established at about 1700 K. This shows a great improvement which this new potential brings into the understanding of the superionic properties of $BaF_2$ over previous works. Radial distribution functions and mean square displacements of cations with $BaF_2$ have also been studied where it was established that at around 800 K, both cation and anion are still at their mean positions, whereas at 1000 K, the anion ($F^-$) starts diffusing. The anion on the other hand was found to move from its mean position at about 1700 K confirming this as the melting temperature of c-$BaF_2$. Diffusion constant was found to be in the range of $4.55\times\ 10^{-5}$ $cm^2/s$ at around 500 K to $1.52\times\ 10^{-4}$ $cm^2/s$ at 1000 K which is typical of superionic conductivity.

## LIST OF TABLES

## LIST OF FIGURES

## SYMBOLS AND ABBREVIATIONS

| | |
|---|---|
| $\Psi$ | Full or many body wave function |
| $E$ | Hamiltonian total energy |
| $M_I$ | Nuclei masses |
| $Z_I$ | Nuclei charges |
| $\hbar$ | Reduced Plank's constant |
| $\bigtriangledown^2$ | Second derivative of gradient |
| $e$ | Electronic charge |
| $m$ | Electron mass |
| $\vec{R}_I$ | Nuclei positions |
| $H$ | Total Hamiltonian |
| $H_e$ | Electron Hamiltonian |
| $r_i$ | Electron position |
| $\psi_e$ | Electron wave-function |
| $\psi_{nucl}$ | Nuclei wave-function |
| $n_{\vec{r}}$ | Charge density |
| $v_{\vec{r}}$ | Ground state potential |
| $E_{xc}$ | Exchange correlation energy |
| $F[n(r)]$ | Universal functional |
| $T$ | Kinetic energy |
| $\epsilon_k$ | Lagrange multiplier |
| $\epsilon_{xc}^{hom}$ | Homogeneous exchange correlation |
| $T_m$ | Melting point temperature |
| $T_c$ | Phase transition temperature |
| $\sigma$ | Ionic conductivity |
| $\Delta E$ | Defect formation energy |
| $k_B$ | Boltzmann constant |
| $\epsilon$ | Strain tensor |

| | |
|---|---|
| $C'$ | Shear modulus |
| $E_a$ | Energy of single atom |
| $E_c$ | Energy of crystal without defect |
| $E_F$ | Frenkel defect energy |
| $E_i$ | Energy of crystal with interstitial |
| $H_B$ | Born-Oppenheimer Hamiltonian |
| $u_{n\vec{k}(\vec{r})}$ | Modulation function |
| $\rho_c$ | Density of charged systems |
| $\alpha$ | Madelung Constant |
| $\bigtriangledown$ | Partial differential |
| $D_\alpha$ | Diffusion Constant |
| $v_{xc}^{LDA}$ | Exchange correlation potential (Local Density Approximation) |
| $p_i$ | Dipole moment on ion i |
| $p_i^{sr}$ | Short-range dipole moment on ion r |
| $E(r_i)$ | Electric field at position $r_i$ |
| $B$ | Bulk modulus |
| $\tau$ | Stress tensor element |
| $V_0$ | Volume of the unstrained box |
| $E_i^f$ | Interstitial formation energy |
| $E_v^f$ | Vacancy formation energy |
| $E_{disp}$ | Energy of crystal with atom displaced |
| $\Gamma$ | Summation of forces, stresses and energies |
| $z*$ | Value of effective charge of a system |
| $\Psi^*$ | Pseudo wavefunction |
| $DFT$ | Density functional theory |
| $KS$ | Kohn-Sham |
| $HK$ | Hohenberg-Kohn |
| $IFC$ | Interatomic force constant |
| $PAW$ | Projector augmented wave |

| | |
|---|---|
| $USPP$ | Ultrasoft pseudopotentials |
| $LAPW$ | Linearized augmented plane waves |
| $NVE$ | Number, Volume and Energy |
| $LDA$ | Local density approximations |
| $LSDA$ | Local Spin Density Approximations |
| $GGA$ | Generalized gradient approximations |
| $PBEGGA$ | Perdew-Burke-Ernzerhof GGA |
| $PW91$ | Perdew and Wang 91 |
| $c - BaF_2$ | Cubic Barium Flouride |
| $GEA$ | Gradient Expansion Approximation |
| $E_c^{PBE}$ | GGA correlation energy function |
| $H^{PBE}$ | Gradient contribution to $E_c^{PBE}$ |
| $\bigtriangledown n$ | Charge density variation |
| $F_x(s)$ | Enhancement factor for local exchange |
| $L_{Nose}$ | Nosé Langragian |

## ACKNOWLEDGEMENTS

A PhD thesis is a contribution of countless people and this one is no exception. Supervisors, friends, family, church and strangers at conferences and schools can bring in new thoughts that can set the research rolling. This means that I will be forgetting someone, but with a little hope that they will never read this introduction and that makes me safe. The order of acknowledgment should not be an issue since I will not obey any order in listing my acknowledgments.

Allow me to thank God for His divine connection that allowed me to meet all the people on the way to this work and while on this work. He ensured that all things were at the right place and at the right time for me. Though some may have delayed of which patience was being tested and experience being developed, but eventually in His wisdom all the necessary requirements came at His perfect timing. So all things worked for my good. God is the great discoverer and the wise teacher declares that "Whatever is, has already been, and whatever will be, already is. God repeats what has passed." (Eccl 3:15).

University of Eldoret, thank you for giving me the opportunity to undertake this program in your institution. Also I will not forget the department of Physics for allowing me in their department. Dr. N.W. Makau was patient in every step of this work. From its inception, through its development to full maturity he was available. Discussions with Nic always brought out deep details that at some stage were overlooked. This was true mentor-ship. Thank you sir. Prof. G.O. Amolo was always available. His suggestion to apply for Sandwich Training Programme in Education in The Abdus Salam International Centre for Theoretical Physics will remain in the memory for the rest of my career. Your hard work will be rewarded by the Almighty. Prof. S. Sandro is an amazing teacher. Our discussions were always productive. His insights and experience have lifted this research to beyond initial perspective.

Sandwich Training in Education Programme of The Abdus Salam Interna-

tional Centre for Theoretical Physics, thank you. The opportunity I got in this institution and the discussions I had with the group at the Condensed Matter Physics; just to mention a few, Dr. Ghosh, Dr. Somesh, Dr. Inam, Dr. P. Carlos, Dr. Raji, Dr. Omolulu among others can not be measured. Without this funding I could have missed the challenge that I got in my work from these great people. STEP secretary Dory Calligaro you are a wonderful communicator. Thank you for all your correspondences. Prof. Bingelli, thanks a lot for the headship of STEP programme.

African School on Electronic Structure Methods and Applications (ASESMA) was such a great team. The school in Cape Town South Africa in the month of July 2010 added friends who catapulted this work higher. Dr. Kris Delaney, thank you for the discussions on the elastic constants and defects. Dr. Alison Hatt was an inspiration and a challenge in this school. All the other mentors and participants gave a renewed energy for work and a push to the edge in this research. The network has continued to vibrate along way and may we continue in that spirit of a family.

Many thanks also goes to Emerging Nations Science Foundation (ENSF) for paying my thesis examination fees. This gesture has made my study faster and better.

May I thank my patient and lovely wife Helen for taking care of our children Faith and Caleb while I was away for a duration of 20 months and two weeks because of research. My dear, you are special to me and I have you always in my heart and mind. Remain a blessing to us all in our family.

Bishop Dr. George Gichana (G.G.) of Deliverance Church Eldoret was an inspiration in all his sermons. He disqualified my one degree and disoriented my thinking to reorient it for higher thought and vision. Your message on VISION is the root course of all this ”mess”. You remain a spiritual father always.

Space and time will not allow me to mention all that Kabarak University has done for me, but I will not forget to mention the study leave and research

funding, as well as collegues at Kabarak University; Dr. C. Maghanga, R. Rotich, Mumbua P. S., Elizabeth O. and the entire department staff of Computing and Mathematics, you have been my cheer peers and have always urged me to run on. Prof. R. Gateru (currently Principal Kenya Methodist University - Nairobi Campus) thank you for inspiring me to continue in my thirst for knowledge.

Finally, I want to appreciate Plane Wave Self-consistent field (PWSCF)_forum team of Quantum Espresso, you are too diverse and numerous to be listed here, and too spread out over the globe to fit in one category. Let us keep Quantum Espresso code moving on.

# CHAPTER ONE

# INTRODUCTION

## 1.1 Background on Barium Flouride, $BaF_2$

Barium fluoride ($BaF_2$) falls in the family of compounds referred to as alkaline-earth fluorites. In general, fluorites constitute a large family of compounds with interesting physical properties, crystallizing in a variety of structures [1, 2]. $BaF_2$ crystallizes into cubic, orthorhombic and hexagonal phases with the cubic phase being the most stable of the three phases at room temperature. Many of the fluorides such as $CaF_2$ are already employed in technological applications such as optical coatings [3, 4]. $BaF_2$ is a high-density luminescent material (radiation hard material) used in gamma ray and elementary particle detectors. In the process of irradiation, there is formation of defects and the more difficult the formation of defects, the better is the material for such an application [5].

$BaF_2$ has also been found to exhibit superionic property and this property can be improved by doping it by a small amount of appropriate impurities to create redistribution of ions in the space charge region [6]. Superionic materials or fast ions are conductors that ions are highly mobile. For this reason, $BaF_2$ is considered as a material that can be used in the high-temperature batteries, fuel cells, chemical filters and sensors [6].

Specifically, materials crystallizing in the fluoride structure have been studied extensively [7]. However, several questions pertaining to structure-property relationships still remain unanswered. The clarification of these questions to a great extent relies on first principles or *ab initio* calculations. In this study, a quantum mechanical study on electronic structure (i.e. band structure, density of states and phonons) and the independent elastic constants of $BaF_2$ was carried out.

Elastic constants of solids give important information about their mechanical and dynamical properties and they also provide important details concerning the

nature of the forces at play in the solids [8, 9]. The single crystal elastic constant of solids help in interpreting seismic wave velocities and their lateral variations. A study of elastic constants can help in the understanding of inter-atomic interactions, mechanical stability of solids, material strength and the general internal structure of materials. Elastic properties are also related to the thermal properties according to Debye theory [10]. When elastic constants are studied for different phases of a solid, they can help in the understanding of phase transition properties of the material. Elastic constants of the cubic phase of $BaF_2$ have so far been studied extensively [8] since it is the most stable phase at room temperature and low pressure. In this study, the elastic constants of the cubic phase were studied at room temperature and low pressures by using first principles with periodic boundary conditions. Calculations of elastic constants for the orthorhombic and hexagonal phases have also been done. These later states are known to be metastable [11].

Superionic properties of $BaF_2$ were studied using molecular dynamics approach. While in the previous studies simple interaction potentials such as Buckingham potential were used [12], here, a more comprehensive potential was developed for $BaF_2$. The potential was generated from the first principles calculations to capture the electronic properties and hence improve on the results in comparison to what has been done so far regarding $BaF_2$. The first principle methods were done under the framework of density functional theory, DFT, which is discussed in chapter 3.

## 1.2 Examples of Superionic Compounds

Some of the most studied superionic materials are silver iodide, AgI and lead flouride, $\beta$-$PbF_2$. While lead flouride superionic behaviour resembles that of barium flouride, AgI behaves in a totally different way. AgI exists as both $\beta$ and $\gamma$ phases in ambient conditions and these possess the hexagonal wurzite ($P\bar{6}_3mc$ [13]) and cubic zincblende ($F\bar{4}3m$ [14]) crystal structures, respectively. AgI under-

goes an abrupt superionic transition at 420 K [15]. Within the superionic phase, the ionic conductivity is majorly by $Ag^+$, and the electronic component $\sigma_e$ being about $10^7$ times lower [16]. The $I^-$ was found to be located at a body-centred cubic arrangement. This anion sublattice contains a number of empty sites available as sites for $Ag^+$ to diffuse to.

Lead fluoride ($\beta$-$PbF_2$) shows a rapid ionic conductivity though continuous with increase on heating. It is the anions that diffuses through the crystal of $\beta$-$PbF_2$. This has been confirmed to be true also for a large variety of flourite-structured compounds [17, 18]. In these compounds, the diffusion of the anion is easier than the energy required for the cation defect formation [18]. They also have a large electronic band gap which will need large amount of energy to cross. The transition to the superionic state is accompanied by a $\lambda$-peak in the specific heat $C_p$, whose maximum is generally taken to define the superionic transition temperature which is 711 K for $\beta$-$PbF_2$. Ealier reports of the ionic distribution within superionic $\beta$-$PbF_2$ proposed a molten anion sublattice [19]. However, while there is still no conclusive agreement on this fact, analysis of the $C_p$ data, diffraction studies [20, 21] and molecular dynamics simulations [22] all suggest that the anion defect concentration is less than $\sim 10\%$ at temperature above $T_c$. This is probably a consequence of repulsive interactions between defects [23], which suppress the development of complete sublattice disorder of the type observed in $\beta$-$AgI_2$.

The development of models to describe the inter-ionic interactions allows the possibility of varying the properties of the ions within the simulations and assess the role of, for example, the ionic charge or polarizability in the development of superionic properties.

### 1.3 Factors affecting superionicity

Factors affecting superionic properties of materials can be listed as;

1. Ionic polarizability: Highly polarizable ions in the immobile sublattice can

deform to allow diffusing ions to pass through smaller gaps.

2. Bonding character: Mixed bonding character like ionic-covalent is suggested to be an important characteristic of good superionics by allowing the mobile ion to be stable in several different co-ordinations in diffusion process [24].

3. Concentration of mobile ions: An increase in the concentration $n$ of mobile ions within the expression $\sigma = nZe\mu$ is an advantage though it also depends on the available vacant sites.

4. Ionic charge: Lower charge results in lower Coulomb energies during diffusion.

5. Ionic radius: A small mobile ion is better than a large ion. The small ion is able to diffuse through the gaps.

These factors are not independent but are linked to each other. However, no single factor can stand alone as the most preferred one to explain the presence of high ionic conductivity [25].

### 1.4 Statement of the Problem

$BaF_2$ remains the fastest luminescent material known, making it an ideal high-density luminescent material for applications in gamma ray and elementary particle detectors.

However, most literature on $BaF_2$ has not considered its superionic properties in detail, but have majorly focused on characters such as band structures, phonon transmission and other properties. This work seeks to understand in details the basic properties which include their mechanical, electronic, vibrational and transport properties, as well as defect formation energies and vacancy migration energies.

Another aspect of this work includes the generation of empirical potential for $BaF_2$, which is expected to give more accurate results with regard to the properties of c-$BaF_2$ unlike the classical potential that have been used previously.

## 1.5 Objective of the Study

The objectives of this study include:

- The study of electronic structure properties of $BaF_2$ using density functional theory (DFT) calculations. Some of these properties include ground state electronic and mechanical properties of $BaF_2$, phonon calculations and elastic constants of cubic, orthorhombic and hexagonal phases.
- To study the defects in $BaF_2$ such as interstitial, vacancy and Frenkel, using density functional theory. The effect of defects on the band gap on the stable cubic phase of $BaF_2$ is also studied.
- To generate empirical force field for $BaF_2$ from *ab initio* methods.
- To use molecular dynamics calculations to study some of the properties of cubic $BaF_2$ such as superionic transition and melting temperatures using the newly generated classical force field.

## 1.6 Significance of the Study

The study of the electronic structure has been undertaken to understand the suitable industrial applications of materials and the same has been considered here to establish the appropriate application of $BaF_2$ in industry. Some of the applications of $BaF_2$ are the manufacture of energy conserving batteries and vacuum ultra-violet windows. The mechanical properties such as elastic constants of the cubic, orthorhombic and hexagonal phases of $BaF_2$ are key to the understanding of the stability of each phase. Other mechanical properties such as bulk modulus, anisotropy parameters and stiffness constants $\xi$ have also been studied to help understand the general stability of $BaF_2$ at different phases, which is important in the application of the material in various ways.

In nuclear radiations, defect formation is common when hard materials are bombarded by radioactive elements. $BaF_2$, is radiation-hard and the nature of

defects formation of this material are calculated to bring a clear understanding of the energy necessary for the formation of these defects. Migration energies establish the exact nature and paths that the cation and anions would take in actual migration experiments, an aspect that has not been addressed conclusively before.

Molecular dynamics simulations play a key role in understanding the nature of mobility of molecules at different temperatures. Given that $BaF_2$ is a superionic material, the exact temperature at which this transition takes place has not been clear and the use of this new potential is expected to bring in a new insight on the superionic transition and melting point, which are both expected to be more accurate than those reported earlier.

# CHAPTER TWO

# LITERATURE REVIEW

## 2.1 Introduction

$BaF_2$ has been extensively studied because of its intrinsic optical properties as pointed out earlier in chapter one. Rubloff [26] did an extensive work on far-ultraviolet reflectance spectra of ionic crystals including $BaF_2$, using synchroton radiation as a light source. Other experimental studies include characteristic energy loss spectra [27], photoelectron spectroscopy [28] among others. These works somehow confirmed existence of excitation peaks which was first observed in the reflectance spectra. The observed $BaF_2$ electronic excitation peaks were then interpreted by comparing the results with those of KCl and $CaF_2$ [29] since there were no theoretical studies on $BaF_2$ by then.

Some of the recent works on the theoretical electronic structure of $BaF_2$ are reported by Jiang et al [11] where the electronic structure of the three phases are reported. Schmalzl [30] has done an extensive work on the electronic structure but included also the volume and temperature relationships. For processing, fabrication and application, it is important to know the volume and temperature-dependent effects by inducing stresses and strain in the material [30]. Jia et al [31] have reported some findings on the atomic and electronic structure of $CaF_2$ and $BaF_2$ with H-centres. In another separate, work Shi et al [32] have also looked at the F-centres in $BaF_2$ using the first-principles approach employing CASTEP computer code. Electronic and elastic properties are reported by Xyang et al [33] for the cubic phase of $BaF_2$.

Reduction of thickness in photolithography is limited by the cutoff wavelength of the ultraviolet (UV) transmission. A decrease in wavelength raises problems in making lenses to focus the radiation. For vacuum ultraviolet (VUV) radiation, the lens material of choice is either $CaF_2$ or $BaF_2$ since both are wide-band-gap

insulators (10 eV and above). Some of these optical properties are also studied by Jiang et al [11].

The superionic transition temperature $T_c$ of $BaF_2$ is located at about 1233 K and the melting temperature, $T_m$, is at about 1593 K by Jiang et al. Superionic conductivity is associated with a disorder of the anion sub-lattice and mobile defects at a temperature ($T_c$) well below the general melting temperature, $T_m$. However, inspite of these changes, the cation lattice remains stable until melting point is reached [34]. A large thermal motion is therefore associated with the anions which also happen to be the lighter ions. Ivanov [12] has done some molecular dynamics study on $BaF_2$ using potentials of Born-Mayer-Huggins potential and also established that the molten state of $BaF_2$ allows the anions to diffuse more than cations. Molecular dynamics of other fluorites such as $CaF_2$, $SrF_2$, $PbF_2$ and $SrCl_2$ have also been studied as reported in [35].

The alkaline earth fluorides usually undergo a series of pressure-induced phase transitions to highly coordinated $AX_2$ structures. At ambient conditions $BaF_2$ crystallizes in the cubic fluorite structure ($Fm\bar{3}m, Z = 4$) with three atoms in the primitive face-centred cubic unit cell and twelve atoms in the conventional simple-

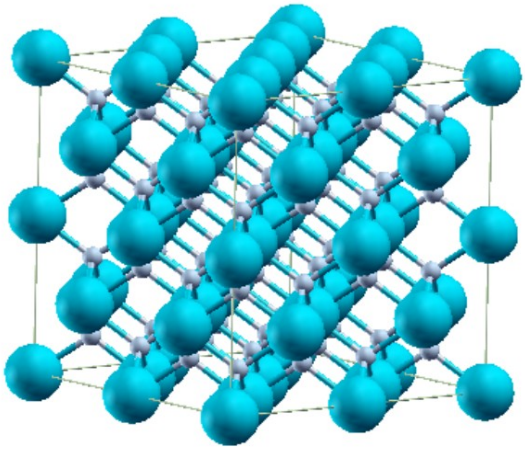

**Figure 2.1: Super-cell crystal structure of $BaF_2$. The cell contains 96 atoms which has eight cubes of four formula units each. Blue (large) circles are the barium atoms and the gray (small) ones are the fluorine atoms.**

cubic cell. In this phase, the cations are at (0,0,0), ($\frac{1}{2}$,$\frac{1}{2}$, $\frac{1}{2}$), ($\frac{1}{2}$,0,$\frac{1}{2}$), ($\frac{1}{2}$,$\frac{1}{2}$,0) and anions at ($\pm\frac{1}{4}, \pm\frac{1}{4}, \pm\frac{1}{4}$) in units of the lattice parameter, *a*. Fig 2.1 shows a 96-atom supercell of cubic $BaF_2$.

$BaF_2$ transforms to the orthorhombic cotunnite-type structure ($Pnam, Z = 4$) at about 5 GPa then to a hexagonal phase at between 10 and 15 GPa. The high pressure phase transition at zero temperature makes the orthorhombic and hexagonal phases metastable [36].

## 2.2 Superionics

A number of solids exhibit ionic conductivities comparable to those found in molten salts and are referred to as superionic conductors, fast-ion or solid electrolytes. The conductivities of these materials reach values of the order of 1 $\Omega^{-1}cm^{-1}$ which is comparable to those observed in the molten state [25]. $BaF_2$ as one of the flourites is known to exhibit superionic properties. Dynamical structural disorder characterizes superionic conduction and is a major challenge to their study. Neutron scattering and molecular dynamics simulation have been recently used to help understand these materials [37, 38]. Availability of large single crystals and the accessible temperature regime at which the phenomena occurs allows a wide range of experimental techniques to be employed in the study of fluorites. The simple structure with disorder and transport being virtually restricted to the anion sub-lattice, make the fluorites exceptionally good test-beds for theoretical calculations.

One property of superionics is that they can go through solid to solid phase transition just before reaching melting point. This transition is subdivided into type I and type II superionics. Type I superionics evolve to highly conducting state abruptly and type II evolve continuously [39]. Superionic conductors are not only of scientific curiosity but there is need to identify new highly conducting solids for the rapidly expanding technological applications within lightweight solid state batteries, high power fuel cells and fast response gas sensors [40]. It is generally

accepted that the specific heat jump and high-temperature conductivity behaviour are due to a diffuse phase transition at which there is a relative disordering of the anion sub-lattice. Nominal pure crystals are known to demonstrate a 'normal' behaviour under ordinary conditions i.e to have a rather low ionic conductivity which is described in terms of a classical approach and is due to the formation and motion of isolated anti-Frenkel defects. At the same time, for a number of fluorite-type compounds ($SrCl_2$, $CaF_2$ and $BaF_2$) the presence of a broad peak in the heat capacity curve has been observed at a temperature $T_C$ (specific heat maximum) essentially below the melting point $T_m$. According to Derrington et al [41], the electrical conductivity of crystalline salts ($SrCl_2$, $CaF_2$, $SrF_2$) increases continuously with temperature and in the premelting region becomes comparable to that of the melts. Precision measurements carried out later for $SrCl_2$ [42] and $\beta$-$PbF_2$ [42, 43] have allowed the peculiarity to be revealed that the ionic conductivity, starting from the intrinsic region grows not linearly but according to a sigmoid-like curve so that the apparent activation energy has a maximum at a temperature close to that for heat capacity jump.

According to classical molecular dynamics study done in Ref.[12], $BaF_2$ becomes superionic at a temperature of about 1250 K. In this present work we will show that indeed this material is superionic using custom-made parametrized potential method which is more accurate. A phase shift of solid-solid phase transition is reported giving further evidence that the anions sub-lattice undergoes disorder, well before melting.

# CHAPTER THREE

# THEORY

## 3.1 The Density Functional Theory, DFT

### 3.1.1 Introduction to DFT

Density Functional Theory (DFT) is currently the most widely used framework for the simulation of electronic structure of materials and molecules. DFT is primarily a theory for investigating the electronic structure and molecules in condensed matter. It is capable of covering the prediction of properties at the ground state of any system of electrons. DFT has relativistic extensions and extension to electromagnetic fields has also been achieved. There are a number of approximations which are usually made in order to enable the computations to be accessible to current computers since more precision comes with more computation hours and hence more computational cost.

DFT is usually preferred in the study of solid state systems over other approaches since it uses the electronic density $n(\vec{r})$ of the system which is much simpler to work with than the 4N-dimensional wavefunction [44]. Another advantage of DFT is the fact that it can also be used in the study of both periodic and non-periodic systems of infinite sizes.

### 3.1.2 Fundamentals of DFT

The many-body theory describes the interaction of electrons of a large system ($\sim 10^{23}$) with atomic nuclei. This large number of interactions makes the theoretical calculations difficult to solve exactly, and hence some approximations are required. These interactions govern most of the observed properties of matter such as mechanical, electrical, thermal and optical properties among others. The

Schrödinger equation for such a system is given as;

$$H\Psi = E\Psi. \tag{3.1}$$

In this expression, $\Psi$ is the full or "many-body" wave-function for all the particles in the interaction (electrons, nuclei and also electromagnetic field). $E$ is the energy eigenvalue corresponding to the wave-function $\Psi$ and $H$ is the total Hamiltonian given as;

$$H = -\sum_i \frac{\hbar^2}{2m}\nabla_i^2 + \frac{1}{2}\sum_{i\neq j}\frac{e^2}{|\vec{r}_i - \vec{r}_j|} - \sum_{i,I}\frac{Z_I e}{|\vec{r}_i - \vec{R}_I|} - \sum_I \frac{\hbar^2}{2M_I}\nabla_I^2 + \frac{1}{2}\sum_{I\neq J}\frac{Z_I Z_J e^2}{|\vec{R}_I - \vec{R}_J|}. \tag{3.2}$$

In eqn.(3.2), the first, second and third terms on the right hand side are the kinetic energy of the electrons, the electron-electron Coulomb interaction and the electron-nuclei interaction, respectively. The fourth term is the kinetic energy of the nuclei and the last term is the nucleus-nucleus interaction. The symbols $\vec{r}_i$ denote the electron position, $\vec{R}_I$ refers to nuclei positions, $m$ is the electron mass, $e$ is the electron charge, $M_I$ are the nuclei masses, $Z_I$ are the nuclei charges and $\hbar$ is the reduced Plank constant.

The Born-Oppenheimer approximation simplifies the many-body problem by assuming that since the nuclei are far much heavier than the electrons, they will move slowly so that electronic and nuclear motion can be separated. Nuclei are treated to be stationary and the electrons move relative to them. Eq.(3.1), can be separated into two independent eigenvalue problems such that the wave function is written as the product of the electron and nuclei wave functions

$$\Psi(\vec{r}, \vec{R}) = \psi_e(\vec{r}, \vec{R}) \times \psi_{nucl}(\vec{R}), \tag{3.3}$$

where the electron wave function depends on the nucleus co-ordinates. Given that the nuclei are now treated to be stationary, we neglect the nuclei problem since it

can be incorporated later. The Schrödinger equation for the electron is now

$$H_e\psi_e = E_e\psi_e, \tag{3.4}$$

and the electron Hamiltonian is

$$H_e = -\sum_i \frac{\hbar^2}{2m} \bigtriangledown_i^2 + \frac{1}{2}\sum_{i\neq j} \frac{e^2}{|\vec{r}_i - \vec{r}_j|} - \frac{1}{2}\sum_{i,j} \frac{Z_I e}{|\vec{r}_i - \vec{R}_I|}. \tag{3.5}$$

The first term on the right hand side of eqn. (3.5) is the kinetic energy of the interacting electrons and the wave function $\psi$ depends on the all-electron co-ordinates which is still a very difficult many-body problem. Hartree [45] suggested that one-electron approximation could be used, and in this case a many-body problem is transformed into a set of one-particle equations for an electron moving in an average potential created by the other electrons. The potential of this non-interacting system is the sum of the potential energy of the ions plus the potential energy of all the electrons. For such a non-interacting system, the $N$-electron wavefunction becomes the product of the one-electron wavefunctions;

$$\Psi = \psi_1(\mathbf{r}_1)\psi_2(\mathbf{r}_2)...\psi_N(\mathbf{r}_N), \tag{3.6}$$

where the variables $\mathbf{r}_i$ include both co-ordinates and spin. The wavefunction is antisymmetric with respect to an interchange of any two electron positions. This assumption ignored the Pauli exclusion principle which requires that the wave function should be antisymmetric under permutation of two co-ordinates. This problem was solved by Hartree-Fock by writing the total wave function as a Slater

determinant of one-electron wave functions;

$$\Psi = \begin{vmatrix} \psi_1(x_1) & \psi_1(x_2) & ...\psi_1(x_N) \\ \psi_2(x_1) & \psi_2(x_2) & ...\psi_2(x_N) \\ . & . & \\ . & . & \\ . & . & \\ \psi_N(x_1) & \psi_N(x_2) & ...\psi_N(x_N) \end{vmatrix}, \tag{3.7}$$

where $\psi_i(x_j)$ are the one-electron wavefunctions. Minimizing the expectation value of the Hamiltonian $\hat{\mathbf{H}}$ with respect to the one-electron wavefunctions gives the Hartree-Fork equations. But the correlation energy which is the sum of all the other quantum effects is beyond the Hartree-Fock theory and requires a more general approach as described in subsection 3.2.

### 3.2 Hohenberg-Kohn (HK) Theorems

The foundation of density functional theory was laid in 1964 by Hohenberg and Kohn [46]. They showed that there is a direct relationship between the potential $V_{ext}(\vec{r})$ and the ground state electron density $n(\vec{r})$, in such away that the infinitely complex many-body problem of solving the Schrödinger equation for $N$-particles can be replaced by an equation for the charge density $n(\vec{r})$. This theorem states that for any system of interacting electrons in a general external potential $V_{ext}(r)$, the ground state electron density $n(\mathbf{r})$ uniquely determines $V_{ext}(r)$ to within a constant:

$$n(\mathbf{r}) \rightarrow V_{ext}(r). \tag{3.8}$$

According to Hohenberg and Kohn, no two different potentials acting on the electrons of a given system can give rise to same ground-state electronic charge density $n(\vec{r})$. This implies that the HK theorem applies to non-degenerate ground states only. The complete many-body Hamiltonian is then implied by $n(\vec{r})$. Hence all the

excited states and their energies are also implied by $n(\vec{r})$. The Hohenberg-Kohn theorem therefore confirms that by using $n(\vec{r})$ rather than wave-functions, the details of many-body Physics can be understood [47]. Consider two different external potentials $V_{ext}^{(1)}(r)$ and $V_{ext}^{(2)}(r)$ which are different by more than a constant but give the same ground state density $n(\mathbf{r})$. These external potentials have corresponding Hamiltonians $\hat{H}_1$ and $\hat{H}_2$ with different ground state wavefunctions, $\Psi_1$ and $\Psi_2$ which are supposed to have the same ground state density $n(\mathbf{r})$. Given that $\Psi_2$ is not the ground state wavefunction of $\hat{H}_1$, then from Rayleigh Ritz variational principle

$$E_1 = \langle \Psi_1 | \hat{H}_1 \Psi_1 \rangle < \langle \Psi_2 | \hat{H}_1 \Psi_2 \rangle, \tag{3.9}$$

where

$$\langle \Psi_2 | \hat{H}_1 \Psi_2 \rangle = \langle \Psi_2 | \hat{H}_2 \Psi_2 \rangle + \int d^3r [V_{ext}^{(1)}(\mathbf{r}) - V_{ext}^{(2)}(\mathbf{r})] n(\mathbf{r}), \tag{3.10}$$

and

$$E_1 < E_2 + \int d^3r [V_{ext}^{(1)}(\mathbf{r}) - V_{ext}^{(2)}(\mathbf{r})] n(\mathbf{r}). \tag{3.11}$$

The inequality in eqn.(3.11) is due to the variational principle for non-degenerate ground states and it can also be shown that

$$E_2 < E_1 + \int d^3r [V_{ext}^{(2)}(\mathbf{r}) - V_{ext}^{(1)}(\mathbf{r})] n(\mathbf{r}). \tag{3.12}$$

Adding eqns.(3.11) and (3.12) gives,

$$E_1 + E_2 < E_1 + E_2, \tag{3.13}$$

which is not true and therefore the desired result is obtained. Thus, the density uniquely determines the external potential to within a physically irrelevant additive constant [44, 48].

Hohenberg and Kohn also showed that there exists a universal functional $F[n(r)]$ (i.e. it is same for all electron systems) which is a functional of electron density $n(\vec{r})$ only, such that the actual ground state energy $E[n(\vec{r})]$ is given

by eqn. (3.14).

$$E[n(\vec{r})] = F[n(\vec{r})] + \int n(\vec{r}) V_{ext}(\vec{r}) d^3r. \tag{3.14}$$

The energy $E[n(\vec{r})]$ is minimized under the constraint that the integral of $n(\vec{r})$ equals the total number of electrons. Furthermore, the value of the minimum coincides with the ground-state energy. Hence, based on these theorems the expectation value of the Hamiltonian in eqn.(3.5) (section 3.1.2) can be written as

$$\langle \psi | H | \psi \rangle = E[n(\vec{r})], \tag{3.15}$$

where $E[n(\vec{r})]$ is the ground state total energy functional and $n(\vec{r})$ is the electron density. Therefore, if one knows the correct density, all ground state properties of the system can be calculated. To find the correct ground state density one minimizes the energy functional with respect to charge density;

$$E_0 = \frac{\delta}{\delta n} E[n(\vec{r})] = E[n_0(r)]. \tag{3.16}$$

This theorem provides the foundation of density-functional theory [49]. It allows an enormous conceptual simplification of the quantum-mechanical problem of searching for the ground-state properties of a system of interacting electrons, for it replaces the traditional description based on wave functions (which depend on $3N$ independent variables, $N$ being the number of electrons) with one which depends only on three variables and charge density. However, there are two major challenges to the straight forward application of this theorem. Firstly, the form of the functional $F$ is unknown and secondly the conditions to be fulfilled for a function $n(\vec{r})$ to be considered an acceptable ground-state charge distribution (and hence the domain of the functional $F$) are poorly characterized. The second problem is hardly addressed at all, and usually the proper normalization of the charge density by the use of Lagrange multiplier is imposed. Levy and Lieb constrained

approach and Kohn and Sham discussed below tried to solve the first question.

### 3.3 Levy and Lieb Constrained Approach

The variational problems can be written explicitly as

$$E_0 = \min_{n(\mathbf{r})} E[n(\mathbf{r})], \tag{3.17}$$

where $E[n(\mathbf{r})] = T[n(\mathbf{r})] + U[n(\mathbf{r})] + V_{ext}(n(\mathbf{r}))$ is the energy functional composed of kinetic $T[n(\mathbf{r})]$, electron-electron potential $U[n(\mathbf{r})]$ and the external potential functional $V_{ext}[n(\mathbf{r})]$. HK theorem and its variational problem has restricted field of applicability i.e electron density $n(\mathbf{r})$ must be $v-$representable (it is the ground state density for some potential $v(\mathbf{r})$). This implies that the density $n(\mathbf{r})$ is the density corresponding to an antisymmetric wavefunction of the ground state of a Hamiltonian [50]. It then follows that the correct formulation of the variational problem becomes

$$E_0 = \min_{n(\mathbf{r})} E_v[n(\mathbf{r})], \tag{3.18}$$

where $v$ represents the $v-$representability of $n(\mathbf{r})$. A generalization of the HK theorem which does not require $n(\mathbf{r})$ to be $v-$ representable is found in the idea of Levy [51] and Lieb [52] and is called Levy-Lieb constrained search approach. In this approach one identifies between ground state wavefunction, $\psi$, and a wavefunction $\psi_\lambda$, which also integrates to the ground state electron density $n(\mathbf{r})$. Since $\psi$ is the ground state wavefunction, we write

$$\langle \psi_\lambda | H_N | \psi_\lambda \rangle \geq \langle \psi | H_N | \psi \rangle = E_0. \tag{3.19}$$

This can also be written as

$$\langle \psi_\lambda | T + U | \psi_\lambda \rangle \geq \langle \psi | T + U | \psi \rangle. \tag{3.20}$$

The wavefunction $\psi$ minimizes the kinetic and the electron-electron repulsion energy and integrates to $n(\mathbf{r})$. This is therefore a double minimization procedure which allows for searching among all the $n(\mathbf{r})$ which are $N$-representable. This formulation can be written as

$$E_0 = \min_{n(\mathbf{r})}[\min_{\psi_{\lambda\to n(\mathbf{r})}} \langle\psi_\lambda|T+U|\psi_\lambda\rangle + \int v(\mathbf{r})n(\mathbf{r})d\mathbf{r}] \tag{3.21}$$

$$\equiv F[n(\mathbf{r})] + \int v(\mathbf{r})n(\mathbf{r})d\mathbf{r},$$

where

$$F[n(\mathbf{r})] = \min_{\psi_{\lambda\to n(\mathbf{r})}} \langle\psi_\lambda|T+U|\psi_\lambda\rangle. \tag{3.22}$$

This defines Levy-Lieb functional. Eqn.(3.22) defines the meaning of a functional and gives an operational definition as the minimum of the sum of kinetic plus interaction energies for all possible wavefunctions with same density $n(\mathbf{r})$ [44]. This functional applies to a wide class of densities derived from wavefunction $\psi$ for $N$ electrons including degenerate states. But still the constrained approach just like the HK approach does not give any method of calculating the functional. This is addressed by Kohn and Sham [53] as discussed below.

### 3.4 Kohn-Sham Approach ($\mathbf{E}_{xc}$)

Kohn and Sham (KS) showed that the way to construct the Hohenberg-Kohn functionals is through the single particle kinetic energy $\mathrm{T}_s[n]$ or independent electrons (i.e. electrons without mutual Coulomb repulsion) in their ground state under the action of an external potential such that their ground state density is $n(\vec{r})$. This theorem states that all the physical properties of a system of interacting electrons are uniquely determined by its ground-state charge-density distribution and is independent of electron-electron interaction. When electron-electron interaction vanishes, $F[n(\vec{r})]$ defines the ground-state kinetic energy of a system of non-interacting electrons as a functional of its ground-state charge-density distri-

bution $T_o[n(\vec{r})]$. Kohn and Sham suggested a non-local functional to be the major part of kinetic energy component $< \hat{T} >$. In this case, if $\Psi_k(\vec{r})$ is taken to be a one-particle wavefunction of this external potential then,

$$n(\vec{r}) = \sum_{k=1}^{N} |\Psi_k(\vec{r})|^2 \tag{3.23}$$

and

$$T_s[n] = \sum_{k=1}^{N} \int d^3r \frac{\hbar^2}{2m} | \bigtriangledown \Psi_k(\vec{r})|^2. \tag{3.24}$$

This kinetic energy is near the exact $< \hat{T} >$ in the ground state. $E[n]$ can then be written as the sum of large external potential energy PE, single-particle KE and Hartree PE terms, plus a remainder $E_{xc}$ as shown in eqn.(3.25).

$$E = \int v(\vec{r})n(\vec{r})d^3r + F[n] = \int v(\vec{r})n(\vec{r})d^3r + T_s[n] + \frac{e^2}{2} \int \frac{n(\vec{r})n(\vec{r'})}{|\vec{r} - \vec{r'}|} d^3r d^3r' + E_{xc}[n]. \tag{3.25}$$

$E_{xc}$ is called exchange-correlation energy and it has both potential and kinetic energy characteristics. $E_{xc}$ is the part of the energy functional that we do not know how to calculate. Minimization of the expression in eqn.(3.25) with respect to the wavefunction $\Psi_k(\vec{r})$ which is equivalent to minimizing energy with respect to density $n(\vec{r})$ gives Schrödinger eqn.(3.26).

$$\left( -\frac{\hbar}{2m} \bigtriangledown^2 + v_{eff}(\vec{r}) \right) \Psi_k(\vec{r}) = \epsilon_k \Psi_k(\vec{r}), \tag{3.26}$$

where $\epsilon_k$ is a Lagrange multiplier for normalization. $v_{eff.}(\vec{r})$ contains external potential, Hartree energy (electrostatic energy) and exchange-correlation terms which is given by eqn.(3.27) as;

$$v_{eff}(\vec{r}) = v(\vec{r}) + e^2 \int \frac{n(\vec{r'})}{|\vec{r} - \vec{r'}|} d^3r' + v_{xc}(\vec{r}). \tag{3.27}$$

The exchange-correlation potential is defined as;

$$v_{xc}(\vec{r}) = \frac{\delta E_{xc}}{\delta n(\vec{r})}. \tag{3.28}$$

Eqns.(3.27) and (3.28) give the exact ground-state energy and density for non-degenerate systems. Variation of the energy functional with respect to $n(\vec{r})$ with the constraint that the number of electrons be kept fixed leads formally to the same equation as would hold for a system of non-interacting electrons subject to an effective potential, also called the self-consistent field, (SCF). The potential $v_{eff}$ of eqn.(3.27) is local and so makes the KS equations easily solved computationally than Hartree-Fock scheme. Local as applied here implies that $v_{eff}$ only acts on the wavefunctions at the point $\vec{r}$. But $v_{xc}$ which is also called exchange-correlation potential in KS equations has a non-local dependence on the density $n(\vec{r})$.

The $\epsilon_k$ term appearing in eqn.(3.26) is only for normalization of the orbitals of $\Psi_k$ during variational procedure and are not excitation energies as in the normal Schrödinger equation. This is because KS theory is purely a ground-state theory. KS equations are solved through an iterative procedure until self-consistency is reached. If $E_{xc}$ was known, it would be possible to solve for the exact ground state energy and density. However, this is not the case, and therefore approximations have to be made in determining ground state energy.

### 3.5 Local Density Approximations (LDA)

The exchange-correlation functional, $E_{xc}$, does not depend on $V_{ext}$ but is a 'universal' functional. Its exact dependence on $n(\vec{r})$ is not known and is normally approximated in calculations. The KS method does not lead to a better approximation as it stands, because the term $E_{xc}[n]$ is still present. To overcome this, Kohn and Sham proposed a local-density approximation (LDA) given as;

$$E_{xc} = \int n(\vec{r})\epsilon_{xc}^{hom}(n(\vec{r}))d^3r, \tag{3.29}$$

in which $\epsilon_{xc}^{hom}$ is the exchange-correlation energy per particle of a homogeneuos electron gas with density $n(\vec{r})$. The $E_{xc}$ energy is thus calculated by assuming that in the vicinity of the point $\mathbf{r}$ the properties of the inhomogeneous electron gas of density $n(\mathbf{r})$ can be approximated by those of a uniform electron gas of that density. The electrons are moving on a positive background charge distribution such that the total ensemble is electrically neutral [54, 55].

The exchange-correlation potential is then given as [54];

$$v_{xc}^{LDA}[n(\vec{r})] = \frac{\delta E_{xc}}{\delta n(\vec{r})} = \epsilon_{xc}[n(\vec{r})] + n(\vec{r})\frac{\partial \epsilon_{xc}[n(\vec{r})]}{\partial n(\vec{r})}. \tag{3.30}$$

In LDA calculations, it is common to split $\epsilon_{xc}[n(\vec{r})]$ into exchange and correlation potentials i.e; $\epsilon_{xc}[n(\vec{r})] = \epsilon_x[n(\vec{r})] + \epsilon_c[n(\vec{r})]$. The exchange potential is given by the Dirac functional [56];

$$\epsilon_x[n(\vec{r})] = -\frac{3}{4}\left(\frac{3}{\pi}\right)^{\frac{1}{3}} n(\vec{r}). \tag{3.31}$$

Accurate values for $\epsilon_x(n(\vec{r}))$ can be determined from Quantum Monte Carlo (QMC) calculations [57]. The values are then interpolated to provide an analytic form for $\epsilon_x(n(\vec{r}))$ [58]. Although LDA works very well for many systems, sometimes it is necessary to use other approximations. There are many attempts to go beyond LDA by expanding the exchange-correlation functional in a power series including higher order terms [59].

### 3.6 Generalized Gradient Approximation

For non-uniform charge densities, the $\epsilon_{xc}$ term can deviate significantly from the uniform result. This deviation can be expressed in terms of the gradient and higher spatial derivatives of the total charge density. In this expansion, if we consider the gradient of the electron density, $\bigtriangledown n(\vec{r})$, we get the generalized gradient approximation (GGA). For systems where the charge density is slowly varying, GGA should be better than LDA though not in all systems. Therefore, a test should be

done on any of these approximations before they are used. The parametrization we have used in our discussions are as described in ref.[60].

The gradient expansion approximation (GEA) suggested in the original work of Kohn and Sham [53] was found by considering the LDA as the first term of a Taylor expansion of the $E_{xc}[n_\uparrow, n_\downarrow]$ about the uniform density, and adding corrections to the next term in the density gradients. But this does not give an improvement of GEA over LDA (or LSDA) because it violates the sum rules and is therefore less accurate than LDA [61, 62]. The basic problem in real materials is that the gradients are so large that the expansion breaks down [44].

The basic idea of GGA's is to express the exchange-correlation energy in the form

$$E_{xc}^{GGA}[n_\uparrow, n_\downarrow] = \int d^3r f(n_\uparrow(\vec{r}), n_\downarrow(\vec{r}), \bigtriangledown n_\uparrow(\vec{r}), \bigtriangledown n_\downarrow(\vec{r})). \tag{3.32}$$

The functional $f$ must be a parametrized analytic function, in order to facilitate practical applications. GGA normally is more accurate in comparison to LDA especially for molecular binding energies [63], which are severely overestimated by LDA. In the solid state, the GGA's expand and soften bonds, leading to larger lattice constants that are sometimes more and sometimes less accurate than those of LDA [47]. Typically, GGA's are in favour of varying density condition more than LDA.

Construction of a first-principles numerical GGA has been done by starting from the second-order density-gradient expansion for the exchange-correlation hole surrounding an electron in a system of slowly varying density, then cutting off its spurious long-range parts to satisfy sum rules on the exact hole that the LDA respects. An analytic fit to this numerical GGA is the functional proposed by Perdew and Wang (PW91) [64], designed to satisfy several other exact conditions.

The GGA pseudopotential used in this work in electronic structure and defect calculations is that developed by Perdew, Burke and Ernzerhof (PBE) [65]. They solve PW91 problems with a simplified construction of GGA for the exchange and correlation potentials, in which all parameters (other than those in LDA)

are fundamental constants. In their derivation, the GGA correlation function is written in the form

$$E_c^{PBE}[n_\uparrow, n_\downarrow] = \int d^3rn \left[\epsilon_c^{unif}(r_s, \varsigma) + H^{PBE}(r_s, \varsigma, t)\right], \tag{3.33}$$

where $r_s = (3/4\pi n)^{1/3}$ is the local Wigner-Seitz radius, $n =$ the number of orbitals, $\varsigma = (n_\downarrow - n_\uparrow)/n$ is the relative spin polarization and $t = |\bigtriangledown n|/2\phi k_s n$ is a dimensionless density gradient. Here $\phi(\varsigma) = \frac{1}{2}\left[(1+\varsigma)^{2/3} + (1-\varsigma)^{2/3}\right]$ is a spin-scaling factor and $k_s = (4k_F/\pi a_0)^{1/2}$ is the Thomas-Fermi (TF) screening wave number, with $a_0 = \hbar^2/me^2$. The gradient contribution $H^{PBE}$ is defined as

$$H^{PBE} = (e^2/a_0)\gamma\phi^3 ln\left\{1 + \frac{\beta}{\gamma}t^2\left[\frac{1+At^2}{1+At^2+A^2t^4}\right]\right\}, \tag{3.34}$$

where

$$A = \frac{\beta}{\gamma}\left[exp\{-\epsilon_c^{unif}/(\gamma\phi^3 e^2/a_0)\} - 1\right]^{-1}, \tag{3.35}$$

and $H^{PBE}$ satisfies the following three conditions [65]:

- It tends to the correct second-order gradient expansion in the slowly varying limit ($t \to 0$)

$$H^{PBE} \to (e^2/a_0)\beta\phi^3 t^2, \tag{3.36}$$

  where $\beta = 0.066725$ [66].

- It approaches the negative value of the uniform electron gas correlation in the rapidly varying limit ($t \to \infty$),

$$H^{PBE} \to -\epsilon_c^{unif}, \tag{3.37}$$

  hence making the correlation energy to vanish. This result is derived from the correlation sum energy rule.

- It must cancel the logarithmic singularity of $\epsilon_c^{unif}$ in the high-density limit,

thus forcing the correlation energy to scale to a constant under uniform scaling to the high density limit and $E_c^{PBE}$ tends to;

$$-\frac{e^2}{a_0}\int d^3r n\gamma\phi^3 ln\left[1+\frac{1}{\chi s^2/\phi^2+(\chi s^2/\phi^2)^2}\right], \tag{3.38}$$

where $s = |\bigtriangledown n|/2k_F n = (r_s/a_0)^{1/2}\phi t/c$ is another dimensionless density gradient, $c = (3\pi^2/16)^{1/3} \backsimeq 1.2277$ and $\chi = (\beta/\gamma)c^2 exp(-\omega/\gamma) \backsimeq 0.72161$.

The exchange energy $E_x^{PBE}$ on the other hand is derived from four further conditions:

(i.) $E_x^{PBE}$ satisfies the uniform scaling condition such that for $\varsigma = 0$, we have

$$E_x^{PBE} = \int d^3r n\epsilon_x^{unif}(n)F_x(s), \tag{3.39}$$

where $\epsilon_x^{unif} = -3e^2k_F/4\pi$ and $F_x(s)$ is the enhancement factor over local exchange, given by

$$F_x(s) = 1 + \kappa - \kappa/(1+\mu s^2/\kappa). \tag{3.40}$$

The correct uniform gas limit is recovered when $F_x(0) = 1$.

(ii.) It obeys the spin-scaling relationship

$$E_x^{PBE}[n_\uparrow, n_\downarrow] = \frac{1}{2}\left(E_x[2n_\uparrow] + E_x[2n_\downarrow]\right). \tag{3.41}$$

(iii.) It recovers the LDA linear response limit, where

$$F_x(s) = 1 + \mu s^2, \tag{3.42}$$

where $\mu = \beta(\pi^2/3) \backsimeq 0.21952$.

(iv.) It satisfies the local Lieb-Oxford bound [67],

$$E_x[n_\uparrow, n_\downarrow] \geq E_{xc}[n_\uparrow, n_\downarrow]$$

$$\geq -1.679e^2 \int d^3r n^{4/3} \tag{3.43}$$

Eqn.(3.43) holds if $F_x(s) \leq 1.804$, where the value of $\kappa = 0.804$ from eqn.(3.40).

Correct features of LSDA are retained in the PBE GGA and these features are supplemented with gradient-corrected nonlocality. It has been shown in Ref.[65], that the PBE functional yields essentially the same results as the PW91. But PBE is in a simple form and easy to understand. In this thesis all calculations are done using PBE generated by the Vanderbilt code as is stated in the methodology chapter.

### 3.7 Bloch functions and plane waves

The calculations presented here are periodic and the natural basis for representing all functions is a set of plane waves. Bloch [68] proved that the solutions of the Schrödinger equation (total wave-function) with periodic potential are of the form

$$\Psi_{n\vec{k}}(\vec{r}) = u_{n\vec{k}}(\vec{r}) exp(i\vec{k}.\vec{r}), \tag{3.44}$$

where $u_{n\vec{k}}(\vec{r}) = u(\vec{r} + n_1\vec{a}_1 + n_2\vec{a}_2 + n_3\vec{a}_3)$ is the periodic part of the wave-function and the sum is performed over a set of vectors $\vec{a}$ which belong to the primitive vectors. The basis vectors of the reciprocal lattice are defined as being orthogonal to two unit cell vectors, and normalized so that the scalar product with the third is unity. The solutions of Bloch functions are traveling plane waves modulated by the function $u_{n\vec{k}}(\vec{r})$ with the periodicity of the crystal potential, that is, with the period of the lattice. The electrons in the periodic potential are thus non-local.

The periodic part of eqn.(3.44), $u_{n\vec{k}}(\vec{r})$, is invariant under translation by a

vector $\vec{R}$ given as;

$$u_{n\vec{k}}(\vec{r}) = u_{n\vec{k}}(\vec{r} + \vec{R}), \tag{3.45}$$

and it can be expanded in terms of a discrete plane-wave set whose wave vectors are the reciprocal lattice vectors of the crystal,

$$u_{n\vec{k}}(\vec{r}) = \sum_{G} c_{\vec{k},\vec{G}} e^{i\vec{G}.\vec{r}}, \tag{3.46}$$

where $\vec{G}$ are the reciprocal lattice vectors [59]. Therefore each electronic wave-function can be written as a sum of plane waves,

$$\psi_{\mathbf{k}}(\mathbf{r}) = \sum_{G} c_{\vec{k},\vec{k}+\vec{G}} e^{i(\vec{k}+\vec{G}).\vec{r}}, \tag{3.47}$$

where the coefficients $c_{\vec{k},\vec{k}+G}$ in eqn.(3.47) are associated with plane waves of kinetic energy $(\hbar^2/2m)|\mathbf{k}+\mathbf{G}|^2$. The KS equations have now been reduced to solving a finite number of electronic wavefunctions at an infinite number of **k**-points within the first Brillouin zone of a periodic cell. The methods of grid sampling such as Monkhorst-Pack [69] are then used to obtain an accurate approximation for the electronic potential and the total energy of an insulator or a semiconductor by calculating the electronic states at a very small number of special **k**-points. In a metallic system, a denser **k**-point grid is necessary to define the Fermi surface precisely and to reduce the magnitude of total energy error which arises from poor sampling of **k**-points. Since the total energy varies with increase in k-points, there is always a need to optimize **k**-points with total energy.

The plane waves with a smaller kinetic energy are typically more important than those with large kinetic energy. Introduction of an energy cutoff will lead to an error in the total energy of the system, but it is possible to reduce the error magnitude by increasing the size of the basis set by allowing a larger energy cutoff. The cutoff energy should therefore be optimized with respect to the total energy of the system until the cutoff value calculated converges to within the required

margin of error.

## 3.8 Density-Functional Perturbation theory, DFPT

### 3.8.1 Introduction to DFPT

The formalism which calculates the response functions of a DFT system is known as density functional perturbation theory or DFPT [70]. If the perturbation strength is characterized by a parameter $\lambda$, then the energy, potentials, and wave-functions have an expansion as a function of lambda;

$$E = E_0 + \lambda E_1 + \lambda^2 E_2 + ... \tag{3.48}$$

The forces and stresses are in $E_1$, and many experiments probe $E_2$ for parameters such as Raman and infra-red spectroscopy, linear optics and elastic constants.

To decouple vibrational from the electronic degrees of freedom, the Born and Oppenheimer approximation discussed in Section 3.1 and given in eqn.(3.2) is used. The equilibrium geometry of the system is given by the condition that the forces acting on individual nuclei will be zero;

$$\mathbf{F}_I \equiv -\frac{\partial E(\mathbf{R})}{\partial \mathbf{R}_I} = 0. \tag{3.49}$$

But the vibrational frequencies $\omega$ are determined by the eigenvalues of the Hessian of the Born-Oppenheimer energy [71], scaled by the nuclear masses $M_I$ and $M_J$ placed at positions $R_I$ and $R_J$, respectively;

$$det|\frac{1}{\sqrt{M_I M_J}}\frac{\partial^2 E(\mathbf{R})}{\partial \mathbf{R}_I \partial \mathbf{R}_J} - \omega^2| = 0. \tag{3.50}$$

Eqn.(3.50) shows that the calculation of the equilibrium state and of the vibrational properties is derived from the computation of the first and second derivatives of its Born-Oppenheimer energy surface. This can be accomplished by using Hellmann-Feynman theorem [72], which states that the first derivative of the

eigenvalues of a Hamiltonian, $H_\lambda$, that depends on a parameter $\lambda$ is given by the expectation value of the derivative of the Hamiltonian:

$$\frac{\partial E_\lambda}{\partial \lambda} = \langle \Psi_\lambda | \frac{\partial H_\lambda}{\partial \lambda} | \Psi_\lambda \rangle, \tag{3.51}$$

where $\Psi_\lambda$ and $E_\lambda$ are the eigenfunction and eigenvalue, respectively for $H_\lambda \Psi_\lambda = E_\lambda \Psi_\lambda$. In the electronic Hamiltonian, the force acting on the $I$th nucleus is given at the ground state as

$$F_I = -\frac{\partial E(\mathbf{R})}{\partial \mathbf{R}_I} = \langle \Psi(\mathbf{R}) | \frac{\partial H_B(\mathbf{R})}{\partial (\mathbf{R}_I)} | \Psi(\mathbf{R}) \rangle, \tag{3.52}$$

where $\Psi(\mathbf{R})$ is the electronic ground-state wave function of the Born-Oppenheimer Hamiltonian, $H_B$, and depends on $\mathbf{R}$ via the electron-ion interaction. The Hellmann-Feynman theorem is given now as;

$$F_I = -\int n_{\mathbf{R}}(\mathbf{r}) \frac{\partial V_R(\mathbf{r})}{\partial \mathbf{R}_I} d\mathbf{r} - \frac{\partial E_N(\mathbf{R})}{\partial \mathbf{R}_I}, \tag{3.53}$$

where $V_{\mathbf{R}}(\mathbf{r})$ is the electron-nucleus interaction, and $n_{\mathbf{R}}(\mathbf{r})$ is the ground-state electron charge density corresponding to the nuclear configuration $\mathbf{R}$. To obtain the Hessian of the Born-Oppenheimer energy surface in eqn.(3.50), the Hellmann-Feynman forces are differentiated with respect to nuclear coordinates as;

$$\frac{\partial^2 E(\mathbf{R})}{\partial \mathbf{R}_I \partial \mathbf{R}_J} = -\frac{\partial \mathbf{F}_I}{\partial \mathbf{R}_J} = \int \frac{\partial n_{\mathbf{R}}(\mathbf{r})}{\partial \mathbf{R}_J} \frac{\partial V_{\mathbf{R}}(\mathbf{r})}{\partial \mathbf{R}_I} d\mathbf{r} + \int n_{\mathbf{R}}(\mathbf{r}) \frac{\partial^2 V_{\mathbf{R}}(\mathbf{r})}{\partial \mathbf{R}_I \partial \mathbf{R}_J} d\mathbf{r} + \frac{\partial^2 E_N(\mathbf{R})}{\partial \mathbf{R}_I \partial \mathbf{R}_J}. \tag{3.54}$$

From eqn.(3.54), calculation of the ground state electron charge density $n_{\mathbf{R}}(\mathbf{r})$ and its derivative with respect to position $\partial n_{\mathbf{R}}(\mathbf{r})/\partial \mathbf{R}_I$, is necessary for the calculation of the Hessian of the Born-Oppenheimer energy surfaces. The Hessian matrix is usually referred to as interatomic force constant (IFC).

Perturbation often takes a given direction $\mathbf{q}$ in reciprocal space. This can be the direction of a phonon or an electric field. Apart from perturbation theory,

a frozen-phonon approach can be applied. This is where a finite perturbation is frozen into the system and energies for different values of $\lambda$ are calculated so that derivatives can be extracted. In the frozen-phonon approach, calculations at $\mathbf{q} \neq 0$ requires a supercell to describe the full fluctuation of the perturbation and can be tricky if $\mathbf{q}$ is not at the correct lattice point of the system. DFPT does not require $\mathbf{q}$ to be at gamma ($\Gamma$) and can work with arbitrary $\mathbf{q}$ values.

### 3.9 Pseudopotentials

Properties of solids depend on the valence electrons. Pseudopotentials are used to approximate the properties of materials by replacing the effects of core ions by a more complicated operator which takes into account not only the potential of the nucleus, but also the screening and repulsion by the core electrons. Pseudopotentials generates wavefunctions which are not varying rapidly close to core states. In the all-electron case the valence wavefunctions have a large number of nodes near the nucleus because of the strong ionic potential. This large number of nodes or high oscillation is necessary for the orthogonality between the valence wavefunctions and the core wavefunctions to be maintained. In fig.3.9, $r_c$ is the cutoff radius and the pseudopotential's bound states will reproduce the valence wavefunctions outside this radius and be smooth inside.

Most pseudopotentials used in electronic structure calculations are generated from all-electron density-functional calculations for spherical atoms. It is important that outside $r_c$, the real and pseudo wavefunctions are identical so that identical charge densities are generated by the wavefunctions. The pseudopotential should therefore satisfy an equation of the form

$$\int_{r_C}^{r} \Psi_{ae}^{*}(\mathbf{r})\Psi_{ae}(\mathbf{r})d\mathbf{r} = \int_{r_C}^{r} \Psi_{ps}^{*}(\mathbf{r})\Psi_{ps}(\mathbf{r})d\mathbf{r}, \tag{3.55}$$

where $\Psi_{ae}(\mathbf{r})$ is the all-electron wavefunction and $\Psi_{ps}(\mathbf{r})$ is the pseudo wavefunction. This equation, together with Fig.3.9 show that all-electron and pseudo wave-

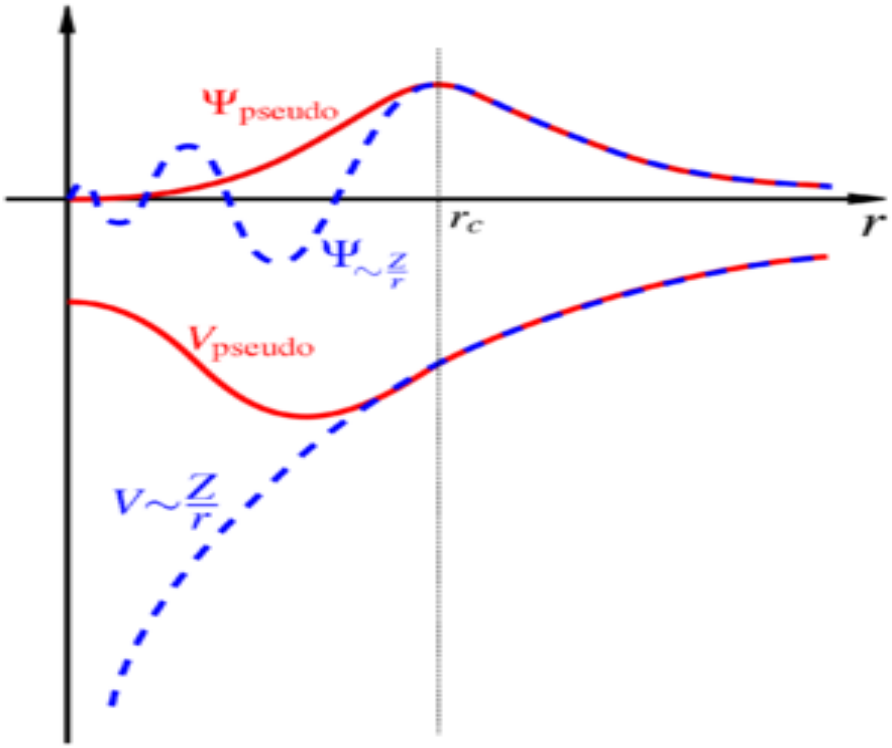


**Figure 3.1: An all-electron in dashed lines and pseudopotential in solid lines. Given is the $r_c$, the cut-off radius for the pseudopotential. Courtesy Ref.[1].**

functions outside the cutoff radius will be the same.

The simplest pseudopotential is a local multiplicative function [73]. In this pseudopotential, it is expected that far from the nucleus it must behave like $Z_{ion}/|\mathbf{r}|$ where $Z_{ion}$ is $Z$ minus the number of none core electrons. But this functional leaves few degrees of freedom to fit the valence states with. This form is sometimes insufficient even for earth and rare earth elements.

In non-local pseudopotential, projector functions are added to the local potential. These projectors are chosen to make the valence states orthogonal to the core states [74]. We then obtain

$$V_{ps} = V_{local} + \sum_c \alpha_c |\psi_c\rangle\langle\psi_c|, \tag{3.56}$$

where $c$ runs over core states. The exact wavefunctions $\psi_c$, which are used and the values of $\alpha_c$ can be chosen to fit the valence eigenstates. An alternative is to write the projectors as a sum over angular momenta, with one projector per $l$ value;

$$V_{ps} = V_{local} - \sum_c \alpha_l |Y_{lm}\rangle\langle Y_{lm}|. \tag{3.57}$$

Pseudopotentials of this form are reported in the work of Bachelet, Hamann and Schlüter [75]. In situations where the overlap between core and valence electrons is necessary, the standard frozen-core pseudopotential approximations may not be appropriate. Louie et al [76] showed that introducing a model core charge into the pseudopotential could correct this. The fitted core charge is added to the valence charge to give a better estimate of the density in the calculation of the exchange correlation energy or what is called semi-core electrons (which is a complex, non-linear functional of the density). The pseudopotential of cations in this work has been developed using this approach.

### 3.9.1 PAW and Ultrasoft Pseudopotentials

A hard pseudopotential requires many plane waves to represent the pseudo wavefunctions and it is soft when few plane waves are used to represent the pseudo-wavefunctions. In norm-conserving pseudopotentials (e.g. non-linear core corrections approach), the charge contained inside the cut-off radius for the pseudo and all-electron wavefunctions must be the same (beyond the cut-off the wavefunctions should be identical). Vanderbilt [77] and Blöchl [78] introduced similar formalisms (ultrasoft pseudopotentials (USPP) and the projector augmented wave (PAW) method respectively) which relax this condition. The PAW method is more general, and encompasses both pseudopotential theory and the linearized augmented plane waves (LAPW) [79] method. The additional degrees of freedom gained from relaxing the norm-conserving condition can be used to make much smoother pseudopotentials, requiring a smaller plane-wave basis set.

Vanderbilt's USPP approach requires the determination of a number of parameters whose choice is important and should be properly tested in order to obtain an accurate and highly transferable pseudopotential. In the PAW method, the construction of pseudopotential is easier since the pseudization of augmentation charges is avoided. This implies that PAW works directly well with the full all-electron wavefunctions and all-electron potentials. The PAW method has also advantage that the total energy expression is simpler. The PAW method does not depend on a reference point like an isolated atom as in pseudopotential method. Instead, PAW uses the full density potential and its convergence is more rapid compared to norm-conserving pseudopotentials [78].

## 3.10 Phonons

Phonons are calculated as second derivatives of energy $E$ with respect to the displacements of two atoms. This derivative gives the inter-atomic force constants (IFC) [80], which can be understood as the change in the force on an atom if

another atom is displaced from its original position. The IFC can be defined as;

$$C_{I,J}(a,b) = \frac{\partial^2 E(\mathbf{R})}{\partial \mathbf{R}_I^a \partial \mathbf{R}_J^b}, \tag{3.58}$$

where $a$ and $b$ label unit cells and $\mathbf{R}_I^a$ and $\mathbf{R}_J^b$ are the atomic positions. In most systems, the IFC dies slowly as the distance between atoms increases. The motion of an atom can influence another atom many atoms away i.e.(these forces are long-range).

The Fourier transform of $C_{I,J}(a,b)$ with respect to the unit cell lattice gives the dynamical matrix $D_{I,J}(\mathbf{q})$ with additional factor of $1/\sqrt{M_\kappa M_{\kappa'}}$. Diagonalizing $D$ gives the phonon frequencies squared, $\omega^2_{m\mathbf{q}}$ and the phonon polarization vectors. The squared phonon frequencies can be compared to experiment such that if $\mathbf{q} = 0$ then it compares to Raman and infra-red frequencies. The full phonon band structure can be obtained by methods such as inelastic X-Ray scattering. Sometimes the eigenvalue of $D$ can become negative and if such a structure is in equilibrium then this corresponds to an atomic displacement which lowers the total energy, and hence characterizes an unstable phonon mode. Unstable, or soft phonons occur in phase transitions and when symmetry is broken. By convention, the soft phonon frequencies are plotted in phonon band structures with a negative frequency, $-\sqrt{|\omega^2_{m\mathbf{q}}|}$.

When $\mathbf{q} = 0$ in a wide band gap materials and semiconductors, an additional non-analytical term intervenes if the crystal is polar (if the material is composed of more than one type of atom). In this case, the displacement due to a phonon can create a finite electrical polarization, and this field can then create forces on the atoms. The perturbation of the systems by this residual electric field must therefore be calculated. This has been implemented in Quantum Espresso Code which is to be used in this study through the implementation of acoustic sum rule and has been applied in phonon calculation of phonon modes in Sec. 5.3.

## 3.11 Defects

### 3.11.1 Point defects and defect migration

Ionic conductors are poor conductors of electricity but their conductivities increase drastically at melting point. At room-temperature, conductivity of ionic crystals is about twenty-two orders of magnitude smaller than the conductivity of typical metallic conductors. This large difference in conductivity can be understood from the fact that the wide band gap in insulators allows only extremely few electrons to become excited from the valence band into the conduction band. Their conductivity is caused by the drift of ions and although their drifts are in orders smaller than in the liquid phase, the ions are able to diffuse from site to site through the lattice. This drift is due to thermally created lattice defects [35]. The ionic conductivity is given as;

$$\sigma_{ion} = N_{ion} e \mu_{ion}, \tag{3.59}$$

where $N_{ion}$ is the number of ions per unit volume that can change their positions, $\mu_{ion}$ is the mobility of these ions and $e$ is the charge of the ion. In order for ions to move through a crystalline solid, they must have sufficient energy to pass over an energy barrier as shown in figure 3.11.1. Further, an equivalent lattice site next to a given ion must be empty in order for an ion to be able to change its position. Thus, $N_{ion}$ depends on the vacancy concentration in the crystal (i.e., on the number of Schottky defects). In short, the theory of ionic conduction contains essential elements of diffusion theory.

The predominant point defects are anion-Frenkel pairs, i.e. anion vacancies and interstitial anions in the cube-centre sites, with ionic transport occurring via the migration of the defects [81]. At temperatures just below melting point, $T_m$, the fluorites exhibit a broad specific heat anomaly which passes through a maximum at a temperature, $T_c$. Ionic conductivity, $\sigma$, increases with temperature which in turn is increased by the presence of Schottky defects. This is the defect where vacancies allow other atoms to easily diffuse through them since less energy is

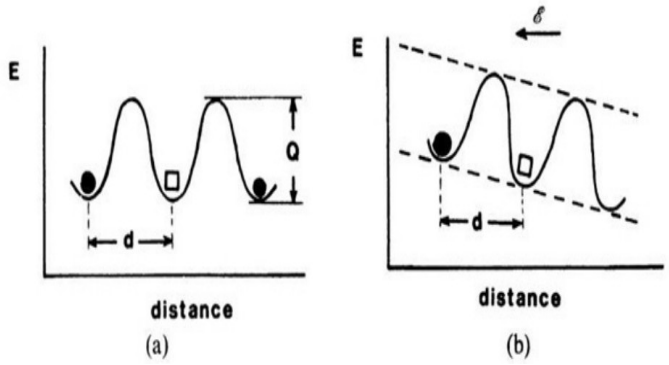


**Figure 3.2: Schematic representation of a potential barrier, which an ion has to overcome to exchange its site with a vacancy. The barrier height increases with introduction of electric field. (a) Without an external electric field; (b) with an external electric field. $d$ = distance between two adjacent, equivalent lattice sites; $Q$ = activation energy. Courtesy Ref.[2].**

required to move the electrons and in the process, the vacancies migrate in the opposite direction. This migration is referred to as diffusion and it is an important property which helps in understanding whether it is likely that the defect can be incorporated during growth and processing. It also helps in the understanding of impurity diffusion, which is always mediated by native defects [82]. Diffusion plays an important role in device degradation and increases electrical conductivity too. In order to interpret the results and compare with experiments, it is necessary to have a knowledge of defect formation energy, $\Delta E$. This is the energy required to create a defect and is related to the concentration of defect $c$ by the expression;

$$c = N_t exp(-\Delta E/k_B T), \tag{3.60}$$

where $N_t$ is the total number of sites in the lattice (per unit volume) where the impurity can be incorporated, $k_B$ is the Boltzmann's constant, and $T$ is the temperature. In most ionic crystals, $\Delta E$ is much greater than $k_B T$ even at the melting point, so that the defect concentration is always very small, and consequently the increase of conductivity on melting is usually very large. In other words, the num-

ber of vacancies increases with increase in temperature. Vacancies are normally created in pairs (e.g. interstitial anion and anion vacancy) to allow the material to be neutral. Materials that contain large numbers of defects, so that the ions can migrate easily (at high temperature $T$) can have a high ionic conductivity [83]. In some ionic materials, this high ionic conductivity (about 1 $\Omega^{-1}cm^{-1}$) with liquid-like values are reached before the crystal melts and such materials are referred to as *superionic conductors*. Superionic conduction can occur through change of the lattice structure: at low temperatures the material has a structure which makes it a normal ionic crystal, but at some elevated temperature it undergoes a discontinuous change to another structure in which the conductivity is liquid-like. Alternatively, the material can become superionic simply because the defect concentration becomes large before melting point.

It is now widely accepted that at high temperature, fluorite compounds undergo a continuous (diffuse) transition to a state of relatively heavy, but far from massive dynamic disorder of the anion sub-lattice, and the ion transport occurs via a hopping mechanism. However many aspects of the superionic behavior of pure fluorites such as the exact nature and the extent of the disorder, the defect structure, and the mechanisms of conduction have not been fully clarified.

Direct experimental studies of point-defect motion have been performed using self-diffusion in isotope structures, electron paramagnetic resonance (EPR) and positron annihilation [82]. Theoretical study of these defects has been done successfully in $CaF_2$. In Chapter three section 3.10, we describe the density functional theory (DFT) approach for defect calculation, and then apply the method described in the calculation of point defects within $BaF_2$.

### 3.11.2 Defects in charged species

A charged crystal is treated as an aperiodic system because there is no periodic unit cell but the calculation is carried out in a section of the system of interest then this calculation is periodically repeated in the supercell. This is different from the

periodic calculation where calculation on one unit cell gives all the information needed [84].

In this study, charged systems calculations were treated as an aperiodic systems with an infinitely large supercell. Such systems are similar to those obtained from similar systems immersed in a jellium background which fills the supercell and neutralizes the charge so that the net charge is zero [85]. The energy of such a system converges slowly showing the decrease in the interaction between the charged system and the jellium background as the supercell size increases. The charge density of the immersed system consists of the density of the charged species, $\rho_c(\mathbf{r})$ and the jellium density, $n_0$;

$$\rho(\mathbf{r}) = \rho_c(\mathbf{r}) + n_0. \tag{3.61}$$

Assuming a charge $q$ on a charged species, then $n_0 = -q/V_c$ to ensure charge neutrality. In eqn.(3.61), the density is split into two parts which are obtained by adding and subtracting a point charge $q$ at position $r_0$ i.e.,

$$\rho(\mathbf{r}) = [q\delta(\mathbf{r} - \mathbf{r}_0)] + [\rho_c(\mathbf{r}) - q\delta(\mathbf{r} - \mathbf{r}_0)]. \tag{3.62}$$

Eqn.(3.62), has two densities which can be written as;

$$\rho(\mathbf{r}) = \rho_1 + \rho_2, \tag{3.63}$$

where $\rho_1$ is the first term in the right hand side and $\rho_2$ is the second term of eqn.(3.62). Position $r_0$ is chosen at the centre of the unit cell where the dipole is zero. The first term $\rho_1$ contributes energy $E_{11}$ which is known as the Madelung energy of a lattice of point charges immersed in neutralizing jellium [86]

$$E_{11} = -\frac{q^2\alpha}{2L}, \tag{3.64}$$

where $\alpha$ is the Madelung constant and is a lattice dependent parameter. $L$ is the

lattice parameter here taken as 11.529 Bohr. The Madelung constant for $BaF_2$ has been approximated to that of a simple cubic structure taken in this work as 1.76267 [87].

### 3.12 Molecular Dynamics

Molecular dynamics is a computer simulation method which involves calculating motion of interacting atoms in the system using Newton's law,

$$F_i = m_i \mathbf{a}_i, \tag{3.65}$$

where each atom $i$ interacts with $N$ atoms in the system, $m_i$ is the atom mass and $\mathbf{a}_i$ is its acceleration. $F_i$ is the force acting on the atom as a result of interaction with other atoms. The force applied on each ion is the superposition of all the forces exerted on it by all the ions in the system. These forces can be derived from specified interionic potentials. A potential is a function $V(r_1, ..., r_N)$ of the ionic positions and it represents the potential energy of the system when the atoms are arranged in that specific configuration [88]. From the potentials, forces are obtained as the gradients of the potentials with respect to the atomic positions;

$$F_i = - \bigtriangledown_{r_i} V(r_i, ..., r_N). \tag{3.66}$$

The simplest form of potential $V$ is written as a pairwise interaction

$$V(r_1, ..., r_N) = \sum_i \sum_{j>i} \phi(|r_i - r_j|). \tag{3.67}$$

Where $j > i$ is to ensure that summation of an atom pair is not repeated. In such an interaction, a trajectory in a $6N$-dimensional phase space is calculated. By solving the equations of motion, trajectories are obtained of all the particles in the system. From these trajectories the required thermodynamic and kinetic characteristics of the system can be derived. It is now well known that pairwise interactions do not give proper approximations of the many properties of materials especially metals and semiconductors.

In a molecular dynamics calculations (MD), it is possible to consider a small

number of particles and neglect the surface effect by using the periodic boundary conditions (PBC). In this scheme, particles are enclosed in a box and the box is repeated to infinity by rigid translation in all the three cartesian directions. The particle $i$ is now made not only to interact with particle $j$ in the same box but also with their images in nearby boxes. Box boundaries are now replaced and the surface effects are also eliminated. In evaluating the interactions in the system, only pairs separated by a distance less than some cut-off radius $R_c$ beyond which the interaction is negligible, are considered. The box can be seen as infinite in size.

At thermal equilibrium the relation

$$\langle v_\alpha^2 \rangle = k_B T/m, \tag{3.68}$$

should hold, where $v_\alpha$ is the $\alpha$ component of the velocity of a given particle. Instantaneous temperature at time $t$ can then be given as;

$$k_B T(t) \equiv \sum_{i=1}^{N} \frac{m v_{\alpha,i}^2(t)}{N_f}. \tag{3.69}$$

The instantaneous temperature $T(t)$ can be adjusted by scaling all velocities with a factor $(T/T(t))^{1/2}$.

In order to solve Newton's equations of motion in molecular dynamics simulations, positions of all particles are used rather than their velocities. Position at the present $(x)$ and previous $(xm)$ time steps with the forces (f) acting on the particles is used to predict the positions at the next time step. At initial stage, the positions of the particles are generated approximately as the previous positions.

### 3.12.1 The force calculation

The net force acting on an ion can be derived from specified interionic potentials. Hamilton's variational principle requires that the phase space trajectory followed by a mechanical system is the one for which the time integral $\int L dt$ is an

extremum, where $L$ is the Lagrangian [89]. Given a set of $N$ independent generalized coordinates and velocities $\{q_i, \dot{q}_i\}$ that describe the state of a conservative system (one in which all forces derive from some potential energy function U), so that $L = L(\{q_i, \dot{q}_i\}$,t), then $L$ can be shown to satisfy the Lagrangian equations

$$\frac{d}{dt}\left(\frac{\partial L}{\partial \dot{q}_i}\right) - \frac{\partial L}{\partial q_i} = 0, i = 1, ..., N. \tag{3.70}$$

If $q_i$ denotes a component of the Cartesian coordinates for one of the atoms then;

$$L = \frac{1}{2}m\sum_i \dot{q}_i^2 - U(\{q_i\}), \tag{3.71}$$

so that eqn.(3.70) becomes

$$m\ddot{q}_i = -\frac{\partial U}{\partial q_i} = F_i, \tag{3.72}$$

where $F_i$ is the corresponding force component.

### 3.12.2 Equations of motion

When forces between particles have been established, then Newton's equations of motion are integrated. There are many schemes of doing this and one of this is Verlet algorithm.The Taylor expansion of the coordinate of a particle around time $t$ can be written as,

$$r(t + \Delta t) = r(t) + v(t)\Delta t + \frac{f(t)}{2m}\Delta t^2 + \frac{\Delta t^3}{3!}\dddot{r} + O(\Delta t^4).$$

Also,

$$r(t - \Delta t) = r(t) - v(t)\Delta t + \frac{f(t)}{2m}\Delta t^2 - \frac{\Delta t^3}{3!}\dddot{r} + O(\Delta t^4).$$

Adding the two equations gives

$$r(t + \Delta t) + r(t - \Delta t) = 2r(t) + \frac{f(t)}{m}\Delta t^2 + O(\Delta t^4),$$

or

$$r(t+\Delta t) \approx 2r(t) - r(t-\Delta t) + \frac{f(t)}{m}\Delta t^2. \tag{3.73}$$

The new position estimate has an error of order $\Delta t^4$, where $\Delta t$ is the time step in Molecular Dynamics. The scheme above does not use the velocity but from trajectories we can write;

$$r(t+\Delta t) - r(t-\Delta t) = 2v(t)\Delta t + O(\Delta t^3)$$

or

$$v(t) = \frac{r(t+\Delta t) - r(t-\Delta t)}{2\Delta t} + O(\Delta t^2). \tag{3.74}$$

The velocity is only accurate to order of magnitude $\Delta t^2$ although the Verlet scheme can be made to achieve better accuracy. The old position at time $(t - \Delta t)$ is discarded and the new position now becomes the old position in the next run. After each time step, the current temperature, the current potential energy and the total energy are calculated, under the constraint that the total energy should be conserved.

### 3.12.3 Initialization

In order to start a molecular dynamics calculation, the atoms are assigned initial positions and velocities. The chosen positions are the positions of the structure that is to be simulated [90]. The structure in this work is the face-centred cubic box of 96 atoms. Each particle is put at its lattice site then we assign a velocity component to every particle, a value that is drawn from a uniform distribution. This initial velocity distribution is a Maxwell distribution kind in shape. All velocities are then shifted such that the total momentum is zero and we scale the resulting velocities to adjust the mean kinetic energy to the desired value.

### 3.12.4 Thermalization

In classical molecular dynamics, simulations are done at NVE ensemble i.e. control is done on the number of particles (N), the volume (V) and the energy (E). But in reality, the temperature is controlled instead of energy. There are many approaches that can be used to control temperature. In the Andersen approach, constant temperature is achieved by stochastic collisions with a heat bath [90]. In this work, molecular dynamics have been done at NVT ensemble (i.e. molecules number (N), volume (V) and temperature (T) are controlled). This implies that pressure was kept constant. To achieve thermal equilibrium, the Nosé thermostat was used [91].

Nosé thermostat is used to keep the temperature in a molecular dynamics calculation around an average value. The method was introduced by Nosé and developed by Hoover [91, 92]. In this approach, a heatbath is introduced in the Hamiltonian with an extra degree of freedom $s$. To achieve an isothermal molecular dynamics calculation, Nosé Langragian is considered different from the normal classical Langragian, and is now written as;

$$L_{Nose} = \sum_{i}^{N} \frac{m_i}{2} s^2 \dot{\mathbf{r}}_i^2 - U(\mathbf{r}^N) + \frac{Q}{2}\dot{s}^2 - L\frac{lns}{\beta}, \tag{3.75}$$

where $L$ is a parameter that is to be fixed and $Q$ is an effective "mass" associated to $s$. The momenta conjugate to $\mathbf{r}_i$ and $s$ follow directly from eqn.3.75;

$$\mathbf{p}_i \equiv \frac{\partial L_{Nose}}{\partial \dot{\mathbf{r}}} = m_i s^2 \dot{\mathbf{r}}_i \tag{3.76}$$

$$p_s \equiv \frac{\partial L_{Nose}}{\partial \dot{s}} = Q\dot{s}. \tag{3.77}$$

It then follows that the Hamiltonian for the extended system of $N$ particles is

$$H_{Nose} = \sum_{i=1}^{N} \frac{\mathbf{p}_i^2}{2m_i s^2} + U(\mathbf{r}^N) + \frac{p_s^2}{2Q} + L\frac{lns}{\beta}. \tag{3.78}$$

In real variable formulation $L = 3N$, where $N$ is the total number of particles, $Q$

is a parameter that should be chosen carefully and it depends on the frequency of the system under simulation. In Nosé equations, the Langragian eqn.(3.75) is required to have a logarithmic term ($lns$) necessary for the correct scaling of time. Any other scheme that does not have such a logarithmic term does not describe the canonical ensemble correctly.

The conventional Nosé-Hoover algorithm only generates the correct distribution if there is a single constant of motion. Normally, the total energy defined by $H_{Nose}$ (eqn.(3.78)), is always conserved. It therefore implies that there should be no other conserved quantity. In most cases, if the momentum is not conserved then the sum of forces $\sum_i \mathbf{F} \neq 0$. If a system is simulated without external forces, $\sum_i \mathbf{F} = 0$, implying that additional conservation law is added, the Nosé-Hoover scheme is still correct because of the additional heatbath provided that the centre of mass remains fixed. This can be achieved by ensuring that during equilibration, the velocity of the centre of mass is set to 0. If the system being simulated has a varying centre of mass or if there is more than one conservation law, then Nosé-Hoover chains are used to obtain the correct canonical distribution [93].

### 3.12.5 Diffusion Constant

When the position of an ion is traced in a mobile sublattice, it is found to drift further and further away from its starting point. The mean square distance the ion travels is given as $\langle \Delta r_\alpha(t)^2 \rangle$. For practical purposes, this quantity is proportional to $t$ at sufficiently long times. The equation connecting $\langle \Delta r_\alpha(t)^2 \rangle$ and $t$ is given as;

$$\langle \Delta r_\alpha(t)^2 \rangle = B_\alpha + 6D_\alpha|t|, \tag{3.79}$$

where $D_\alpha$ is diffusion constant and $B_\alpha$ is some constant [94]. Suppose we want to know the position of $\langle \Delta r_\alpha(t)^2 \rangle$ for a particular value of $t$ from the simulation record. We choose an ion of type $\alpha$ and note its position $r(t_1)$ at some time step $t_1$; then we go forward and record a number of time steps corresponding to our time $t$ and find the new position of that ion $r(t_1 + t)$. The squared difference

$|r(t_1 + t) - r(t_1)|^2$ gives us a value for $\Delta r_\alpha(t)^2$. The same procedure is repeated for the same ion for as many time steps $t_n$ as possible, keeping always the same time difference $t$. The same procedure is repeated for all the ions of the same type. This gives us a large sample of values of $\Delta r_\alpha(t)^2$, whose mean represents the statistical average $\langle \Delta r_\alpha(t)^2 \rangle$ for our chosen time difference $t$. In order to get this as a function of time, many different values of the time difference $t$ need to be determined.

Such an extensive operation is involved in the calculation of not only $\langle \Delta r_\alpha(t)^2 \rangle$, but also in the calculation of radial distribution function. This method is a reliable way of obtaining objective and reliable results from molecular dynamics simulation. According to eqn.(3.79), the diffusion constant, $D_\alpha$, can be obtained directly from the slope of a plot $\langle \Delta r_\alpha(t)^2 \rangle$ against time steps. The mean square displacement $\langle \Delta r_\alpha(t)^2 \rangle$ is an example of a quantity which on the one hand characterizes the single-particle trajectories and on the other hand makes contact with experiment. As discussed later, the good qualitative agreement provides a strong indication that the simulated system closely resembles the real material for $BaF_2$ which is used in this study. This has also been confirmed for other superionic materials discussed by Gillan [35].

### 3.12.6 Polarizable Potentials

Most of the molecular dynamics simulations use the pairwise potentials as shown in eqn.(3.67). Pair potential of Born-Mayer-Huggins is among some of the potentials that have been used in MD of $BaF_2$ simulations [12]. This potential is of the form

$$V_{ij} = \frac{q_i q_j e^2}{r_{ij}} + A_{ij} e^{(-r/\alpha_{ij})} - \frac{C_{ij}}{r^6}, \tag{3.80}$$

where $q_i$, $q_j$ are the charges on the atoms $i$ and $j$, respectively, $r_{ij}$ =|$r_i$-$r_j$| is the distance between the atoms $i$ and $j$, $e$ is the electron charge, while $A_{ij}$, $\alpha_{ij}$, $C_{ij}$ are constants and $r$ is the dipole-dipole distance. The first term in eqn.(3.80) is the Coulombic interaction, the second term is the repulsive interaction of the overlap-

ping shells, while the third term is the van-der-Waals (dipole-dipole) interaction. Ivanov [12] used the "rigid-ion" model [38] in MD of $BaF_2$, where the potential energy of the lattice is obtained as a sum of pair potentials.

Accurate pair potentials which can reproduce selected properties may be appropriate for molecular dynamics. However, ionic systems are not properly characterized with such potentials. In these systems, there are high densities of charged species, thereby creating multipoles. Therefore, many-body interactions might be decisive in determining the structure and dynamics of both the solid and liquid phases. $BaF_2$ is polarizable and is therefore in the category that requires a polarizable potential model. Some of the properties of a good polarizable model include the following. Firstly, it should be transferable from one environment to another, that is, when the state of the system is changed, it should still be applicable. Secondly, its calculated parameters should be able fit to those extracted from *ab-initio* methods. Lastly, it should be fast [95]. Fast implementation in computer codes has been made possible by use of additional degrees of freedom which are included in the simulations. These extra degrees of freedom represent the mobility of the charge density of a given ion due to interactions with its neighbours. To implement this, an imaginary mass is added to the degrees of freedom which is updated together with the ionic coordinates by following their own equation of motion. This reduces computer time because the new coordinates follow their own shorter time scale. The atomic ionic systems may have extra variables such as dipoles, quadrupoles, the ionic radius or the charged shells. The more the variables, the more accurate will be the parametrization, but also the more difficult is the parametrization.

### 3.12.7 Force field model

The potential of Morse-Stretch [96] is a pairwise interaction between ions and is given as;

$$U_{ij} = \frac{q_i q_j}{r_{ij}} + D_{ij}[e^{\gamma_{ij}[1-(r_{ij}/r_{ij}^0)]} - 2e^{(\gamma_{ij}/2)[1-[r_{ij}/r_{ij}^0]}], \tag{3.81}$$

where the interaction between atom types $i$ and $j$ is given by the parameters $q_i, q_j, D_{ij}$, $\gamma_{ij}, r_{ij}^0$ and $r_{ij}$. The second term in eqn.(3.81), is the short range part of the potential. This potential is more transferable between different phases compared to Born-Mayer potential [97]. This potential is improved by inclusion of polarization effects. In this force field model, dipole moments both by electrostatic forces and the short-range repulsive forces between anions and cations are introduced. The short-range contribution is described by the approach of Madden et al [98] and is given as;

$$\mathbf{P}_i^{sr} = \alpha \sum_{j \neq i} \frac{q_j \mathbf{r}_{ij}}{\mathbf{r}_{ij}^3} f_{ij}(r_{ij}), \tag{3.82}$$

where

$$f_{ij}(r_{ij}) = c_{ij} \sum_{k=0}^{4} \frac{(br_{ij})^k}{k!} e^{-br_{ij}} \tag{3.83}$$

and $\mathbf{r}_{ij}$=$\mathbf{r}_i - \mathbf{r}_j$, $b$ and $c$ are parameters of the model [99]. The dipole moments are charge-dipole and dipole-dipole interactions and are calculated using the Ewald summation scheme [100]. The dipoles on each ion are found self-consistently at each step by iterating to self-consistency the equation;

$$\mathbf{p}_i^n = \alpha \mathbf{E}(\mathbf{r}_i; \{\mathbf{p}_j^{n-1}\}_{j=1,N}, \{\mathbf{r}_j\}_{j=1,N}) + \mathbf{p}_i^{sr}, \tag{3.84}$$

where the dipole moment on ion $i$, $\mathbf{p}_i$ depends on the electric field $\mathbf{E}(\mathbf{r}_i)$ at position $\mathbf{r}_i$ which in turn depends on the positions and the dipole moments of all the other ions and on the short-range dipole, $\mathbf{p}_i^{sr}$.

As has been pointed out, most calculations of molecular dynamics for $BaF_2$ have been done using classical molecular dynamics and shell model approaches [12]. In the methodology section we show how the potential for $BaF_2$ was parametrized from *ab-initio* methods. This improved potential which was developed was then used in the study of some of the kinetic and thermodynamic properties of this material.

# CHAPTER FOUR

# METHODOLOGY

## 4.1 DFT Implementation

The calculations of the electronic and dynamical properties reported in this work were performed in the framework of density functional theory (DFT) [101] by employing local density approximation (LDA) and the generalized gradient approximations (GGA)(for the effects of exchange-correlation interaction). We used the pseudopotentials Plane Wave self-consistent field (PWscf) code, distributed with QUANTUM ESPRESSO package [60]. The valence wave functions were expanded in a plane wave basis set truncated at a kinetic energy of 50 Ry (680 eV) for the cubic $BaF_2$ crystal while 30 Ry was used in the orthorhombic and hexagonal phases of $BaF_2$. The electron-ion interactions were described by the ultra-soft pseudo-potential of Perdew-Burke-Enzenhof (PBE) generated by the Vanderbilt code [102]. The tolerance on the total energy convergence in the iterative solution of the Kohn-Sham equations was set at $10^{-8}$ Hartree. The typical configuration for $BaF_2$ is $5s^2 5p^6 6s^2$ and $2s^2 2p^5$ for Ba and F atoms, respectively. Integrations in the Brillouin zone (BZ) were performed using special $k$-points generated with 6x6x6, 2x4x2 and 6x6x3 Monkhorst-pack [69] grids for cubic ($\beta$), orthorhombic ($\alpha$) and hexagonal ($\gamma$) phases, respectively. During structure optimization, the total energy was minimized by varying cell parameters and atomic positions under the restriction of the given symmetry. In the geometrical optimization, all forces on the atoms were converged to less than 0.01 Ry/au. Lattice dynamical response calculations were done with the linear-response approach [71], implemented in the Quantum Espresso code. The code gives response functions of second order derivatives of the total energy with respect to different perturbations like phonon displacements or static homogeneuos electric field as has been explained in Sec.(3.8.1) and Sec.(3.8.2). These responses give physical properties such as phonon dynami-

cal matrices, the dielectric tensor and the Born effective charges. Changing volume by varying lattice constant simulates thermal-expansion and pressure dependence. These give different physical properties like volume-dependent phonon frequencies, elastic constant and high-frequency dielectric constant.

The units used in this thesis are Hartree atomic units i.e. $m_e = \hbar = e = 1$. The unit of energy is Hartree (1 Ha = 27.211 eV), length is in Bohr (1 Bohr = 0.5291 Å), time is expressed in atomic time units a.t.u. (1 a.t.u = 2.4188x10$^{-17}s$, mass in electron masses (9.11x10$^{-31}$kg), forces are in Ry/au, and pressure in Ry/au$^3$ (1Ry/au$^3$ = 1.472 GPa).

## 4.2 Supercell Approach for Defects and Molecular Dynamics

The electronic structure properties of bulk $BaF_2$ considered in this work were carried out with a unit cell of 12 atoms. In the calculations of the defects and molecular dynamics properties, an artificial unit cell (supercell) composed of eight primitive $BaF_2$ unit cells and containing one isolated defect was constructed. The larger the supercell size, the closer the results would be to the case of a single isolated defect, because interactions between impurities in neighbouring supercells are reduced. In the supercell approach for the defect calculation, the defect was surrounded by a finite number of atoms, and the whole structure is repeated periodically. Provided that the defects were separated sufficiently, properties of a single isolated defect could be calculated.

A supercell has an advantage that the electronic structure of the host crystal is the same. That is, the calculation for a supercell which is simply filled with the host crystal without a defect reproduces the same electronic structure properties like band structure of the single crystal.

Convergence as a function of supercell size should however always be checked. In this study, supercell sizes of 24 atoms, 48 atoms, 64 atoms and 96 atoms were tested. While the sizes lower than 96 atoms did not converge properly, a satisfactory convergence was achieved with the 96 atoms. Any size larger than

96 atoms (32 barium and 64 flourine) showed negligible variation. This is also in agreement with the recent study of R. Jia et al [31] on $H$ centres in $CaF_2$ and $BaF_2$. They proved in their work that a 96 atom supercell was large enough for the calculations of $H$ centres. Further more, when the size is extremely large, this becomes expensive computationally.

### 4.3 DFT Methods for Calculating Elastic Constants

The calculations of elastic constants were done by applying the approach of Wang et al [8]. Elastic constants were calculated as the second derivatives of the internal energy with respect to strain tensor ($\varepsilon$). During structural optimization, the enthalpy $H = E + PV$ was minimized by varying the length of the lattice vectors, while the angles between the lattice vectors and the atomic positions in the unit cell were fixed. The volume contribution to total energy was eliminated by using volume conserving strains. Firstly, this conserved the identity of the calculated elastic constants with the strain-stress coefficients, which are appropriate for the calculation of elastic wave velocities. Secondly, the total energy depends on the volume much more strongly than the strain and by choosing volume conserving strains one avoids the separation of these two contributions to the total energy. Lastly, the change in the basis set associated with the applied strain is minimized and hence reducing computational uncertainties. Elastic constants were obtained at the equilibrium relaxed structure at any volume $V$ by straining the lattice, relaxing the symmetry to allow internal degrees of freedom, and evaluating the total energy changes due to the strain as a function of its magnitude, $\delta$ [8]. The system was fully relaxed after each distortion in order to reach the equilibrium state with approximately zero forces on all atoms.

The theoretical elastic constants were calculated from energy variation by applying small strains to the equilibrium lattice configuration. For a solid under

strain, elastic energy is given as,

$$\Delta E = \frac{V}{2} \sum_{i=1}^{6} \sum_{j=1}^{6} C_{ij} e_i e_j, \tag{4.1}$$

where $V$ is the volume of the undistorted lattice cell, $\Delta E$ is the energy increment from the strain with vector $e = (e_1, e_2, e_3, e_4, e_5, e_6)$ and $C_{ij}$ is the matrix of the elastic constants. To obtain the elastic constants, firstly 21 sets of $\frac{\Delta E}{V}$ versus $\delta$ values were obtained by varying the lattice parameter in the range $-0.02 < \delta < 0.02$ in steps of 0.002. The data obtained was fitted by using a quadratic polynomial (shown in the results section 5.4) and then the relevant elastic constants were calculated from the coefficient of the quadratic term of the polynomial using the appropriate equations.

### 4.3.1 The Cubic Phase

The calculation of elastic constants for the cubic phase of $BaF_2$ was less straineous compared to the hexagonal or orthorhombic phases. The cubic phase has three independent elastic constants; $C_{11}$, $C_{12}$ and $C_{44}$. The cubic unit cell is shown in Fig. 4.3.1

The primitive vectors of the cubic phase are defined as;

$$\begin{pmatrix} \vec{a}_1 \\ \vec{a}_2 \\ \vec{a}_3 \end{pmatrix} = \begin{pmatrix} 0 & \frac{\vec{a}}{2} & \frac{\vec{a}}{2} \\ \frac{\vec{a}}{2} & 0 & \frac{\vec{a}}{2} \\ \frac{\vec{a}}{2} & \frac{\vec{a}}{2} & 0 \end{pmatrix}, \tag{4.2}$$

where $\vec{a}$ is the lattice parameter. The primitive vectors $\vec{a_i} = (1, 2, 3)$ are transformed to the new vectors under strain by the relationship;

$$\begin{pmatrix} \vec{a}_1{}' \\ \vec{a}_2' \\ \vec{a}_3' \end{pmatrix} = \begin{pmatrix} \vec{a}_1 \\ \vec{a}_2 \\ \vec{a}_3 \end{pmatrix} .(I + \varepsilon), \tag{4.3}$$

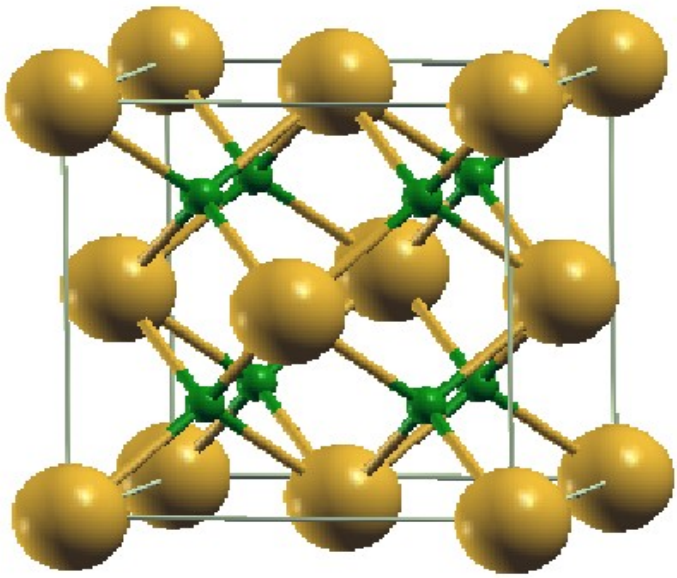

**Figure 4.1: Cubic unit cell crystal structure of $BaF_2$. The unit cell contains four formula units where green colour (small spheres) is flourine and gold (large spheres) is barium atom.**

where $\varepsilon$ is the strain tensor and $I$ is an identity matrix. This links to the strain vector $e$ by

$$\varepsilon = \begin{pmatrix} e_1 & \frac{e_6}{2} & \frac{e_5}{2} \\ \frac{e_6}{2} & e_2 & \frac{e_4}{2} \\ \frac{e_5}{2} & \frac{e_4}{2} & e_3 \end{pmatrix}. \tag{4.4}$$

In the calculation of the lattice constants for the cubic phase, the tri-axial shear strain $e = (0, 0, 0, \delta, \delta, \delta)$ is usually applied to the crystal [103]. Then elastic constant $C_{44}$ can be obtained from the equation;

$$\frac{\Delta E}{V_o} = \frac{3}{2} C_{44} \delta^2. \tag{4.5}$$

Shear modulus $C'$ is calculated from the volume-conserving orthorhombic strain

$e = (\delta, \delta, (1+\delta)^{-2} - 1, 0, 0, 0)$ using the relation;

$$\frac{\Delta E}{V_o} = 6C'\delta^2 + O(\delta^3) \tag{4.6}$$

and $C' = \frac{1}{2}(C_{11} - C_{12})$.

On the other hand, bulk modulus $B$ can be obtained from the strain under hydrostatic pressure $e = (\delta, \delta, \delta, 0, 0, 0)$ [8] using the relation that,

$$\frac{\Delta E}{V_o} = \frac{9}{2}B\delta^2. \tag{4.7}$$

Substituting the values for $C_{44}$ calculated from eqn.(4.5), shear modulus $C'$ and bulk modulus $B$ appropriately, the three elastic constants $C_{11}$, $C_{12}$ and $C_{44}$ can be determined from the respective relations.

### 4.3.2 Elastic Constant of the Orthorhombic Phase

In the recent work of Ravindran et al [10, 104], the method of calculating the elastic constants for the orthorhombic and the hexagonal phases of a fluorite are shown. These methods were used to calculate the elastic constants of orthorhombic and hexagonal phases of $BaF_2$ in this work, since it was focussed on $BaF_2$ and not all flourites.

The face centred orthorhombic phase of $BaF_2$ has three lattice parameters **a**, **b** and **c**. A cut-off kinetic energy of 30 Ry and a k-point grid of 2x4x2 were used to simulate the elastic constants of the orthorhombic phase of this material. Fig. 4.3.2 shows the unit cell of the orthorhombic phase of $BaF_2$.

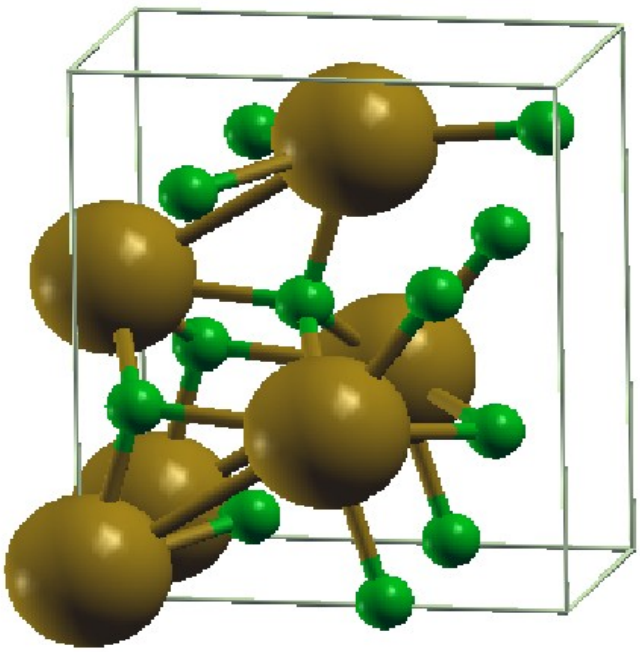

**Figure 4.2: Orthorhombic unit cell crystal structure of $BaF_2$. The unit cell contains four cations (big spheres) and eight anions (small spheres).**

Bravais lattice vectors of the orthorhombic phase have a matrix of the form:

$$\mathbf{R} = \begin{pmatrix} \frac{\sqrt{3}}{2}a & \frac{1}{2}a & 0 \\ -\frac{\sqrt{3}}{2}a & \frac{1}{2}a & 0 \\ 0 & 0 & \frac{c}{a} \end{pmatrix}.$$

**R** can be strained according to the relation **R'**=**RD** where **R'** is the deformed matrix with distorted lattice vectors and **D** is the symmetric distortion matrix, which contains the strain components. In this case small distortions of $\delta = 0.002$ taken between -0.02 to 0.02 were considered.

Since there are nine independent elastic constants, this means that nine different strains are required to determine them. The nine distortion matrices used in the present investigation are described in the distortion matrices $D_1$ to $D_9$. The first distortion matrix is;

$$D_1 = \begin{pmatrix} 1+\delta & 0 & 0 \\ 0 & 1+\delta & 0 \\ 0 & 0 & 1 \end{pmatrix}.$$

This gives compression or expansion to the system and preserves the symmetry but changes the volume. The ratio of energy change to volume is given as

$$\frac{\Delta E}{V_o} = (C_{11} + C_{12})\delta^2. \tag{4.8}$$

The second distortion matrix is

$$D_2 = \begin{pmatrix} (1+\delta)^{-1/3} & 0 & 0 \\ 0 & (1+\delta)^{-1/3} & 0 \\ 0 & 0 & (1+\delta)^{2/3} \end{pmatrix},$$

which gives the volume and symmetry-conserving variation of $c/a$. The ratio of

energy change to volume with this distortion is

$$\frac{\Delta E}{V_o} = (\tau_1 + \tau_2 + \tau_3)\delta + \frac{1}{9}(C_{11} + C_{12} - 4C_{13} + 2C_{33})\delta^2, \tag{4.9}$$

where $\tau_i$ is an element in the stress tensor. The third distortion matrix $D_3$ is

$$D_3 = \begin{pmatrix} \frac{1+\delta}{(1-\delta^2)^{1/3}} & 0 & 0 \\ 0 & \frac{1-\delta}{(1-\delta^2)^{1/3}} & 0 \\ 0 & 0 & \frac{1}{(1-\delta^2)^{1/3}} \end{pmatrix}.$$

This distortion acts on the base of the plane which elongates $a$ and compresses $b$ in a way that the volume is conserved. The related ratio of energy to volume for this distortion is;

$$\frac{\Delta E}{V_o} = (\tau_1 - \tau_2)\delta + (C_{11} - C_{12})\delta^2, \tag{4.10}$$

where $\tau_1$ and $\tau_2$ are still elements of the stress tensor as described in eqn.(4.9). Using the distortions given by eqn.(4.10), the ratio of change in energy to original volume was calculated and eqns.(4.11-4.13) were used to calculate the corresponding elastic constants;

$$\frac{\Delta E}{V_o} = \tau_1\delta + \frac{C_{11}\delta^2}{2}, \tag{4.11}$$

$$\frac{\Delta E}{V_o} = \tau_2\delta + \frac{C_{22}\delta^2}{2}, \tag{4.12}$$

$$\frac{\Delta E}{V_o} = \tau_3\delta + \frac{C_{33}\delta^2}{2}. \tag{4.13}$$

These relations were used to calculate the elastic constants $C_{11}$, $C_{22}$ and $C_{33}$. In this case, symmetry remains orthorhombic with these strains but the volume is changed by the distortion. Using the volume conserving monoclinic shear distortions $D_4$, $D_5$ and $D_6$, the shear elastic constants $C_{44}$, $C_{55}$ and $C_{66}$ were obtained

[10], as,

$$D_4 = \begin{pmatrix} \frac{1}{(1-\delta^2)^{1/3}} & 0 & 0 \\ 0 & \frac{1}{(1-\delta^2)^{1/3}} & \frac{\delta}{(1-\delta^2)^{1/3}} \\ 0 & \frac{\delta}{(1-\delta^2)^{1/3}} & \frac{1}{(1-\delta^2)^{1/3}} \end{pmatrix},$$

$$D_5 = \begin{pmatrix} \frac{1}{(1-\delta^2)^{1/3}} & 0 & \frac{\delta}{(1-\delta^2)^{1/3}} \\ 0 & \frac{1}{(1-\delta^2)^{1/3}} & 0 \\ \frac{\delta}{(1-\delta^2)^{1/3}} & 0 & \frac{1}{(1-\delta^2)^{1/3}} \end{pmatrix},$$

$$D_6 = \begin{pmatrix} \frac{1}{(1-\delta^2)^{1/3}} & \frac{\delta}{(1-\delta^2)^{1/3}} & 0 \\ \frac{\delta}{(1-\delta^2)^{1/3}} & \frac{1}{(1-\delta^2)^{1/3}} & 0 \\ 0 & 0 & \frac{1}{(1-\delta^2)^{1/3}} \end{pmatrix}.$$

The ratio of change in energy to original volume corresponding to the distortions $D_4$, $D_5$ and $D_6$ can then be written as

$$\frac{\Delta E}{V_o} = 2\tau_4\delta + 2C_{44}\delta^2, \tag{4.14}$$

$$\frac{\Delta E}{V_o} = 2\tau_5\delta + 2\frac{C_{55}\delta^2}{2}, \tag{4.15}$$

$$\frac{\Delta E}{V_o} = 2\tau_6\delta + 2\frac{C_{66}\delta^2}{2}. \tag{4.16}$$

The remaining three elastic constants were then calculated using volume conserving orthorhombic distortion matrices of the following types:

$$D_7 = \begin{pmatrix} \frac{1+\delta}{(1-\delta^2)^{1/3}} & 0 & 0 \\ 0 & \frac{1-\delta}{(1-\delta^2)^{1/3}} & 0 \\ 0 & 0 & \frac{1}{(1-\delta^2)^{1/3}} \end{pmatrix},$$

$$D_8 = \begin{pmatrix} \frac{1+\delta}{(1-\delta^2)^{1/3}} & 0 & 0 \\ 0 & \frac{1}{(1-\delta^2)^{1/3}} & 0 \\ 0 & 0 & \frac{1-\delta}{(1-\delta^2)^{1/3}} \end{pmatrix},$$

$$D_9 = \begin{pmatrix} \frac{1}{(1-\delta^2)^{1/3}} & 0 & 0 \\ 0 & \frac{1+\delta}{(1-\delta^2)^{1/3}} & 0 \\ 0 & 0 & \frac{1-\delta}{(1-\delta^2)^{1/3}} \end{pmatrix}.$$

$D_7$ increases $a$ and decreases $b$ with an equal amount but $c$ remains constant. $D_8$ distortion matrix increases $a$ and decreases $c$ with an equal amount and $b$ is kept constant. $D_9$ distortion increases $b$ and decreases $c$ with an equal amount and $a$ remains constant. All these last three distortion matrices are the same as those of the unstrained lattice, and hence the volume is conserved. The ratio of the change in energy to original volume corresponding to these distortions are given as;

$$\frac{\Delta E}{V_o} = (\tau_1 - \tau_2)\delta + \frac{1}{2}(C_{11} + C_{22} - 2C_{12})\delta^2, \tag{4.17}$$

$$\frac{\Delta E}{V_o} = (\tau_1 - \tau_3)\delta + \frac{1}{2}(C_{11} + C_{33} - 2C_{13})\delta^2, \tag{4.18}$$

$$\frac{\Delta E}{V_o} = (\tau_2 - \tau_3)\delta + \frac{1}{2}(C_{22} + C_{33} - 2C_{23})\delta^2. \tag{4.19}$$

The relations given by eqns.(4.17)-(4.19) give the values of the elastic constants

$C_{12}$, $C_{13}$ and $C_{23}$ for the orthorhombic phase with the superposition of the already calculated elastic constants $C_{11}$, $C_{22}$ and $C_{33}$.

### 4.3.3 The Hexagonal Phase

The same approach employed for the orthorhombic phase [104] was used for the hexagonal phase. The hexagonal phase of $BaF_2$ has two lattice parameters $a$ and $c$ (see fig. 3.3) with Bravais lattice vectors in matrix form as,

$$\mathbf{R} = \begin{pmatrix} \frac{\sqrt{3}}{2}a & -\frac{1}{2}a & 0 \\ -\frac{\sqrt{3}}{2}a & \frac{1}{2}a & 0 \\ 0 & 0 & \frac{c}{a} \end{pmatrix}.$$

The k-point grid used in this case was 6x6x3 with a plane wave cut-off energy of 35 Ry. Again **R** can be strained according to the relation **R'**=**RD** where **R'** is the deformed matrix with distorted lattice vectors and **D** is the symmetric distortion matrix, which contains the strain components. Small distortions of between -0.02 to 0.02 at intervals of 0.002 were again considered as in the orthorhombic case. Since there are five independent elastic constants, five different strains are needed to determine them. The first three distortion matrices, $D_1$, $D_2$ and $D_3$ used in the present investigation were the same as those used for the orthorhombic phase, while the remaining two distortions $D_{10}$ and $D_{11}$ are given as,

$$D_{10} = \begin{pmatrix} \frac{1}{(1-\delta^2)^{1/3}} & 0 & \frac{\delta}{(1-\delta^2)^{1/3}} \\ 0 & \frac{1}{(1-\delta^2)^{1/3}} & 0 \\ \frac{\delta}{(1-\delta^2)^{1/3}} & 0 & \frac{1}{(1-\delta^2)^{1/3}} \end{pmatrix}.$$

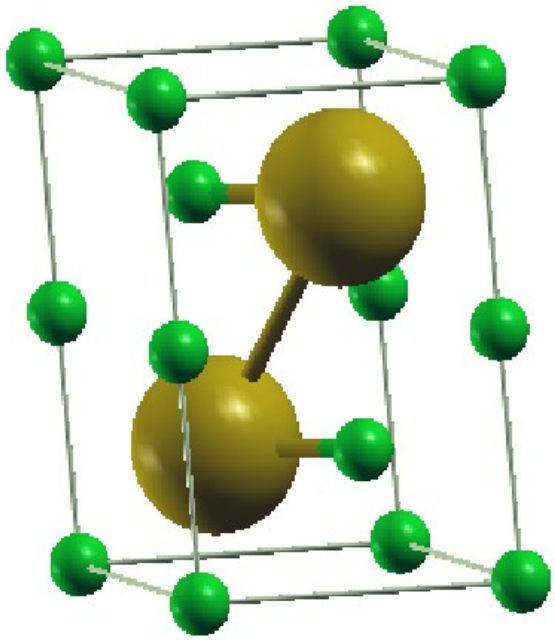

**Figure 4.3: The Hexagonal unit cell crystal structure of $BaF_2$. The unit cell contains two cations (large) and four anions (small).**

$$D_{11} = \begin{pmatrix} 1 & 0 & 0 \\ 0 & 1 & 0 \\ 0 & 0 & 1+\delta \end{pmatrix}.$$

The $D_{10}$ distortion matrix is a volume-conserving triclinic distortion, and the ratio of energy to volume with distortion is;

$$\frac{\Delta E}{V_o} = \tau_5 \delta + 2C_{55}\delta^2. \tag{4.20}$$

The last distortion matrix involves stretching of the $c$ axis while keeping other axes unchanged. Hence the hexagonal symmetry is preserved, but volume is changed. The ratio of energy to volume with distortion is;

$$\frac{\Delta E}{V_o} = \tau_3 \delta + \left(\frac{C_{33}}{2}\right)\delta^2. \tag{4.21}$$

The five elastic constants can therefore be found from eqns., (4.8), (4.9), (4.10), (4.20) and (4.21) [104]. The bulk modulus $K$ is calculated by differentiating the equation-of-state. For hexagonal crystals, $K$ is a combination of elastic constants, i.e,

$$K = [C_{33}(C_{11} + C_{12}) - 2C_{13}^2]/C_S \tag{4.22}$$

with $C_S$ being

$$C_S = C_{11} + C_{12} + 2C_{33} - 4C_{13}. \tag{4.23}$$

The volume dependence of optimized $c/a$ is related to the difference in the linear compressibility along the $a-$ and $c$-axes ($k_a$ and $k_c$). The dimensionless quantity $f$ describes this as

$$f = K(k_a - k_c) = \frac{dln(c/a)}{dlnV}. \tag{4.24}$$

In terms of the elastic constants

$$f = (C_{33} - C_{11} - C_{12} + C_{13})/C_S. \tag{4.25}$$

$C_S$ is calculated by varying the $c/a$ ratio at a given volume, according to the isochoric strain

$$\varepsilon(\delta) = \begin{pmatrix} \delta & 0 & 0 \\ 0 & \delta & 0 \\ 0 & 0 & (1+\delta)^{-2} - 1 \end{pmatrix}. \tag{4.26}$$

### 4.3.4 Stability Parameters

Relative stability of solid structures can be measured from the difference in cohesive energies of the relevant phases. Zener anisotropy $A$ is an indicator of the degree of anisotropy in the solid structure compared to the isotropic material [8]. For the cubic phase, it is given as;

$$A = \frac{2C_{44}}{C_{11} - C_{12}}. \tag{4.27}$$

The optimized coordinates of ions releases internal strain in the deformed lattice configuration. From those optimized coordinates, the Kleinman internal-strain parameter $\xi$ and elastic stiffness constants are given as [105]

$$\xi = \frac{C_{11} + 8C_{12}}{7C_{11} + 2C_{12}}. \tag{4.28}$$

The macroscopic elastic constants, bulk modulus $K$ and elastic shear constant given as ($C_{11}$-$C_{12}$)/2 are related to bond-bending force constant $\varphi$ and bond-stretching force constant $\Gamma$ [106] by the equations;

$$3K = \frac{\sqrt{3}}{4d}(3\Gamma + \varphi) - 0.355C_o, \tag{4.29}$$

and

$$(C_{11} - C_{12})/2 = \frac{\sqrt{3}}{2d}\varphi - 0.053C_o, \tag{4.30}$$

where $C_o$ is the Coulomb contribution. If this latter quantity is neglected, the bond-stretching force constant $\Gamma$ and bond-bending force constant $\varphi$ can be obtained from

$$\varphi = \frac{2d}{\sqrt{3}}\frac{C_{11} - C_{12}}{2} \tag{4.31}$$

and

$$\Gamma = \frac{4d}{\sqrt{3}}K - \frac{1}{3}\varphi, \tag{4.32}$$

where $d$ is the bond length, a parameter that needs to be calculated so as to determine these properties. For the cubic structure of $BaF_2$, $d$ between disimilar ions is 2.642 Å.

Zener anisotropies in the orthorhombic phase are three; Firstly, $A_1$ which is the shear anisotropic factor for the {100} shear planes between the ⟨011⟩ and ⟨010⟩ directions. Secondly, $A_2$ which is the shear factor in the {010} shear planes between ⟨101⟩ and ⟨001⟩ directions. Lastly, for the ⟨001⟩ direction, the shear planes between {110} and {010}, the zener anisotropy is labelled as $A_3$ [10]. The

hexagonal phase has anisotropies $A_1$ and $A_2$ which are given as;

$$A_1 = \frac{1}{2C_{44}} + \frac{C_{33} + 2C_{13}}{2(2C_{13}^2 - C_{33})(C_{11} + C_{12})} - \frac{1}{2(C_{11} - C_{12})}, \tag{4.33}$$

$$A_2 = \frac{1}{2C_{44}} + \frac{C_{11} + C_{12} + C_{13}}{2(C_{13}^2 - C_{33})(C_{11} + C_{12})}. \tag{4.34}$$

If $A_2$ is greater than $A_1$, then it means that contraction is easiest in any direction normal to the hexagonal axis [107].

### 4.3.5 Derivation of Bulk Modulus along Crystallographic Axes

Bulk modulus of a solid under compression, at volume $V$ and temperature $T$ is given as;

$$B = -V\left(\frac{\partial P}{\partial T}\right)_V$$

$$= V\left(\frac{\partial^2 E}{\partial V^2} -\right)_T - TV\left(\frac{\partial(\sigma B)}{\partial V}\right)_T + \frac{V}{2}\sum_i \hbar\left(\frac{\partial^2 v_i}{\partial V^2}\right)_T, \tag{4.35}$$

where $P = -\left(\frac{\partial E}{\partial V}\right)_T$ is the applied pressure, $E$ is the internal energy, $\sigma$ is the thermal expansivity and $v_i$ is a vibrational frequency. The last two terms in eqn.(4.35), are the finite temperature and zero point corrections, respectively. The corrections are usually small and are normally ignored [108].

From the independent elastic constants, it is possible to derive the bulk modulus along the crystallographic axes from the single crystal. In defining bulk modulus for the cases where the strains perpendicular to the stress directions are all equal, one obtains,

$$B_{relax} = \frac{\Lambda}{(1 + \sigma + \beta)^2}, \tag{4.36}$$

where $\Lambda = C_{11} + 2C_{12}\sigma + C_{22}\sigma^2 + 2C_{13}\beta + C_{33}\beta^2 + 2C_{23}\sigma\beta$. For cubic crystals, $\sigma = \beta = 1$, while for the tetragonal and hexagonal crystals $\sigma = 1$. For the

orthorhombic crystal, $\sigma$ and $\beta$ are given as [104];

$$\sigma = \frac{(C_{11} - C_{12})(C_{33} - C_{13}) - (C_{23} - C_{13})(C_{11} - C_{13})}{(C_{33} - C_{13})(C_{22} - C_{12}) - (C_{13} - C_{23})(C_{12} - C_{23})}, \tag{4.37}$$

and

$$\beta = \frac{(C_{22} - C_{12})(C_{11} - C_{13}) - (C_{11} - C_{12})(C_{23} - C_{12})}{(C_{22} - C_{12})(C_{33} - C_{13}) - (C_{12} - C_{23})(C_{13} - C_{23})}. \tag{4.38}$$

The bulk moduli along the **a**, **b** and **c** axes are thus defined as;

$$B_a = a\frac{dP}{da} = \frac{\Lambda}{1 + \theta + \vartheta}, \tag{4.39}$$

$$B_b = b\frac{dp}{db} = \frac{B_a}{\theta}, \tag{4.40}$$

$$B_c = c\frac{dP}{dc} = \frac{B_a}{\vartheta}, \tag{4.41}$$

where $\theta$ and $\vartheta$ are the relative change of the **b** and **c** axes as a function of the deformation of the **a** axis. From these relations, the linear bulk modulus can be calculated. Calculations of Voigt's and Reuss's shear modulus and other related mechanical properties can be found in Appendix A.

## 4.4 Calculation of Defects

### 4.4.1 Interstitial and Vacancy Formation

All the calculations for defects were done at ground-state conditions. For interstitial formation energy, the octahedral site, two bridge sites and four-fold hollow sites were considered [109].

To calculate the formation energy for interstitials, the total energy of the relaxed perfect crystal ($E_c$) was first calculated before introducing an interstitial. After introducing a single interstitial into the relaxed system, the crystal was again relaxed to calculate the total energy of the system with an interstitial, $E_i$. Thus

the interstitial formation energy is given as;

$$E_i^f = E_i - E_c - E_a, \tag{4.42}$$

where $E_a$ is the energy of the single atom in the vacuum [110] in the case of cation, and the energy of a $F_2$ molecule in vacuum in the case of anion. The energy $E_a$ of the free single atom was obtained by placing the atom of cation or anion in a large cubic box of 20 Bohr in size. Vacancy formation energies for both cation and anion were done by removing one atom of F or Ba and the lattice was then relaxed. If $E_v$ is the relaxed energy of the crystal containing the vacancy, then at a stable minimum the vacancy formation energy $E_v^f$ is given as;

$$E_v^f = E_v - E_c + E_a. \tag{4.43}$$

The Frenkel defect energy $E_F$, was calculated from the relation,

$$E_F = E_i + E_v - 2(E_c). \tag{4.44}$$

The separation between Frenkel defects are assumed to be infinite such that there is no interaction between them. To implement this separation distance, both vacancy and interstitial energies were calculated separately.

In order to compare results obtained in this study with those of other works, the Frenkel pair formation energy was also determined by creating an interstitial and a vacancy close to each other (in the same super-cell). The defect formation energy was determined by the energy difference between the bulk super-cell and the relaxed super-cell containing the cation or anion Frenkel defect ($E_{disp}$) as shown in eqn.(4.45);

$$E_F = E_{disp} - E_c. \tag{4.45}$$

$E_{disp}$ is the energy of the relaxed system when the atom is displaced and $E_c$ is the energy of the perfect crystal without defect. To ensure that interstitial and

vacancies do not recombine for cation, the second nearest neighbour was found to be stable, while for anion, we found that the defect was only stable at the third nearest neighbour just as reported for $CaF_2$ [109].

### 4.4.2 Vacancy Migration Energy

When vacancies migrate to a neighbouring site, they must pass through the saddle point. Migration energy was therefore determined as the difference between the total energy of the model lattice with an atom at the lattice point before the migration and that with the atom at the saddle point. The saddle point was defined as the place where the total energy of the model lattice is at its maximum for a particular migration route. The vacancy migration path is fairly direct and hence the difference between our calculation and the nudged elastic band NEB method is expected to be minimal [110].

## 4.5 Constructing Interatomic Potentials

In the Born-Oppenheimer approximation, the electronic and nuclei wavefunctions are decoupled as described in Chapter three section 3.1. The energy eigenvalue, $E$, of eqn.(3.1) can also be written as $V(\mathbf{R}_i)$ and will depend parametrically on the coordinates of the nuclei. This function $V(\mathbf{R}_i)$ is called *inter-atomic potential*. To design potential function $V(\mathbf{R}_i)$, the nuclei (atoms) are allowed to move and a functional is selected to mimic the behaviour of the true potential in realistic ways for specific materials. This is done by selecting an analytical form for the potential and finding an actual parametrization for the functions that constitute the analytical form that have been chosen. The analytical form chosen can have a number of parameters that need to be modeled.

## 4.6 Potentials for Barium Flouride

In our parametrization procedure, the empirical potentials were fitted into *ab initio* data as described by Tangney-Scandolo [99] in the parametrization of the

force field for silica. In their approach, the potential of Morse-Stretch form is used because of its transferability nature. Usually in the empirical approach, the potential is given as a function of coordinates of atomic positions. For the empirical approach to be accurate, the force field used should be able to represent the electronic effects which are important for ionic motions. A good force field should thus properly capture the electronic effects necessary for ionic motions.

### 4.6.1 Potential Parametrization

A classical polarizable potential with fixed point charges and atomic polarizables as implemented in the *Asap* code [99] was used in the parametrization of the potentials. Conditions for fitting were chosen at 1200 K with pressure set at zero. This temperature was chosen so as to give $BaF_2$ amorphous form and therefore different number of configurations that were used in the fit. Starting from a suitable potential (here Buckingham potentials [12] were used), a molecular dynamics run to obtain the initial configurations was done. The configurations are supposed to be far apart to minimize similarities between them. These configurations from MD runs were used in the *ab initio* studies to do a self-consistent calculation. The parameters of the potential were fitted to forces, stresses and total energies taken from these configurations using the force-matching approach [111]. In *ab initio* calculations, density functional theory (DFT) using pseudopotential method with generalized gradient approximation [65] was employed. All calculations were done on a supercell of 32 barium and 64 flourine atoms. An energy cut-off of 50 Ry was used for the convergence of the calculations of stress. In this scheme of potential parametrization, the function

$$\Gamma = w_f \Delta F + w_s \Delta S + w_E \Delta E, \tag{4.46}$$

was minimized to get the force field parameters. $\Delta F, \Delta S$ and $\Delta E$ are the differences between the classical and *ab initio* forces, stresses and energies, respectively [99]. The values $w_f, w_s$ and $w_E$ are the corresponding weights of the forces, stresses

and energies, respectively. Details of the results of minimization procedure in Appendix B.

# CHAPTER FIVE

# RESULTS AND DISCUSSIONS

## 5.1 Structural Optimization

Lattice constant of cubic $BaF_2$ was calculated and results compared with those in literature obtained using different approaches as shown in Table 5.1.

**Table 5.1: Structural optimizaton of the cubic phase of $BaF_2$ at ground state conditions.**

| Cubic (C1) | a(a.u.) | Ref. |
|---|---|---|
| Quantum espresso(GGA) | 11.53 | Present |
| ABINIT (LDA) | 11.43 | [30] |
| CRYSTAL (GGA) | 11.94 | [11] |
| Expt. (300K) | 11.72 | [36] |
| VASP (PAW) | 11.87 | [30] |

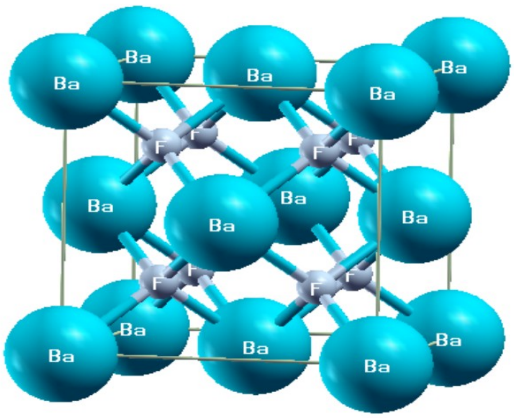


**Figure 5.1: Optimized structure of the cubic phase of $BaF_2$.**

Fig. 5.1 shows an optimized structure of cubic $BaF_2$. From the optimized structure, a plot of the system's total optimized energy versus lattice constant for the cubic phase of $BaF_2$ was plotted as shown in fig. 5.1, where it is seen that the equilibrium lattice constant occurs at a value of 6.10 Å. This shows a deviation of about 1.61% compared to experimental value and hence it compares well

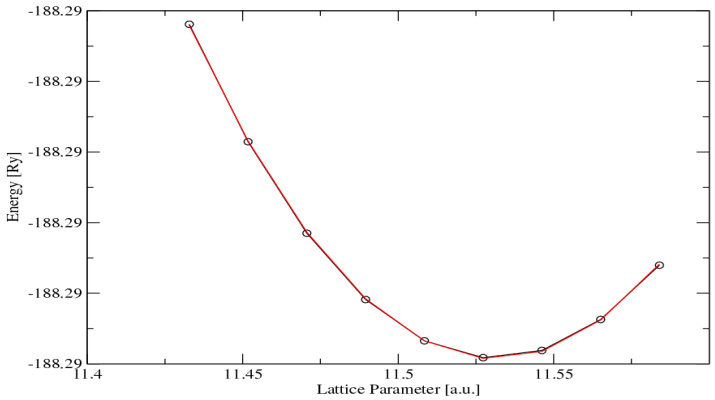


**Figure 5.2: Optimized plot of energy (in Ry) versus lattice constant (in a.u.). The optimized lattice constant is found at the minimum point of the curve at 11.529 Bohrs (1 a.u. = 0.5291 Å).**

with experimental observations and theoretical calculations from other codes as shown in Table 5.1. It is however known that LDA usually underestimates lattice constant while [112] GGA over-estimates them [112]. Owing to the fact that theoretical calculations are done at 0 K, the values obtained in this study were lower than those calculated experimentally at room temperature because of thermal-expansion effects, though such changes are expected to be minimal given that we are working on a solid. The good agreement between calculations involving our pseudopotential and the all-electron methods confirms that the pseudopotential used in the calculations here is reliable.

## 5.2 Electronic band structure

Figure 5.2 shows the calculated DFT-GGA band structure and density of states (DOS) of cubic $BaF_2$ where the calculated band gap for $BaF_2$ was found to be an indirect gap with a value of 7.2 eV. This value is however underestimated by

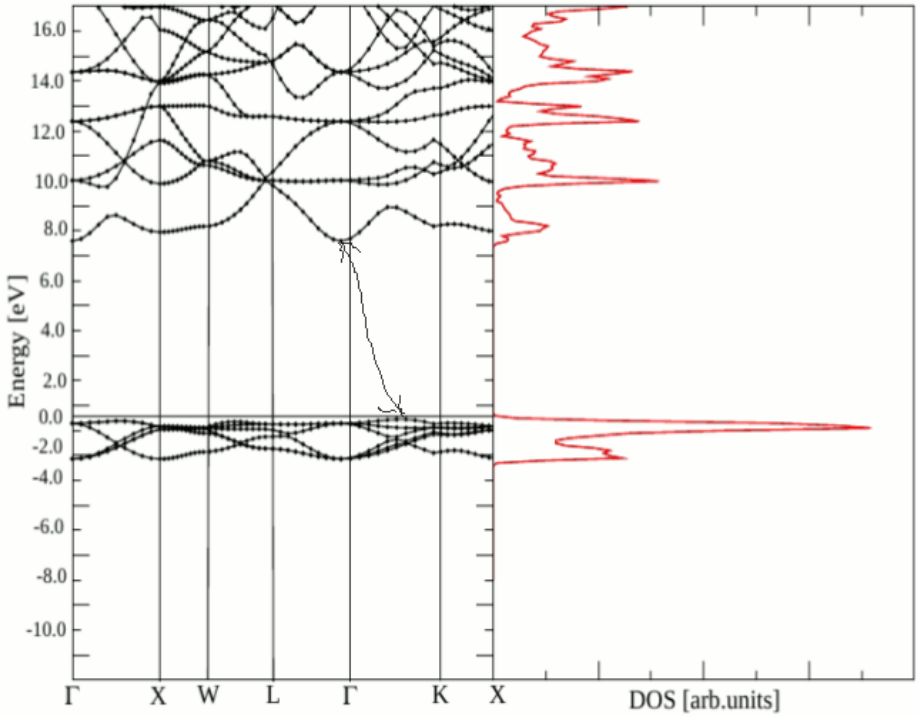


**Figure 5.3: Band structure and DOS of cubic phase of $BaF_2$.**

28% when compared to the experimental one of about 10 eV [30]. This arises from the well known phenomena from DFT calculations where GGA approximations always tend to underestimate the fundamental energy band gap [112] as a

result of approximations made in say the exchange-correlation functional. PAW pseudopotentials are not used in this current work though expected to improve on the results. The use of PAW pseuodopotentials are however more expensive computationally. The energy band gap was located between $\Gamma$ and $K$ as the top of valence band and the lowest point in the conduction band, respectively. Using WIEN97 (LDA), Schmalzl [30] obtained an indirect band gap of 7.197 eV, while TB-LMTO gave a value of 6.37 eV [30]. A summary of results for the band gap energies are given in Table 5.2, where our calculated value was closer to the experimental value when compared to other first principle studies reported so far. The band structures of the orthorhombic and hexagonal phases are presented in Appendix A.

**Table 5.2: Band gap energies (in eV) of c-$BaF_2$ in comparison with previous calculations and experiment.**

| Method | Direct | Indirect | Ref. |
|---|---|---|---|
| QE(GGA) | 7.25 | 7.20 | Present |
| WIEN97(LDA) | 6.70 | 7.19 | [30] |
| WIEN97(GGA) | 7.19 | 7.09 | [30] |
| LCAO-DFT(GGA) | 7.50 | | [11] |
| Exp.(300K) | 11.00 | 10.00 | [30] and ref. therein |

## 5.3 Phonons

Being a wide band gap material, $BaF_2$ undergoes the so-called LO-TO splitting (longitudinal and transverse optical) which occurs in insulating materials [113, 114]. This gives two transverse waves and one longitudinal wave. Frequency ($\omega$) dependence linearly on the lattice constant as shown in fig. (5.3). After 6.535 Å (12.35 a.u.), $\omega_{Raman}$ (the lower curve) would go to zero with any small variation. Other frequencies go to zero at much larger parameters.

Fig. 5.3 shows the phonon dispersion curves of cubic $BaF_2$, whereby with three atoms in the unit cell, nine branches of phonon dispersion are obtained. The transverse modes are degenerate in the [001] direction while $\Gamma$-point phonon frequencies

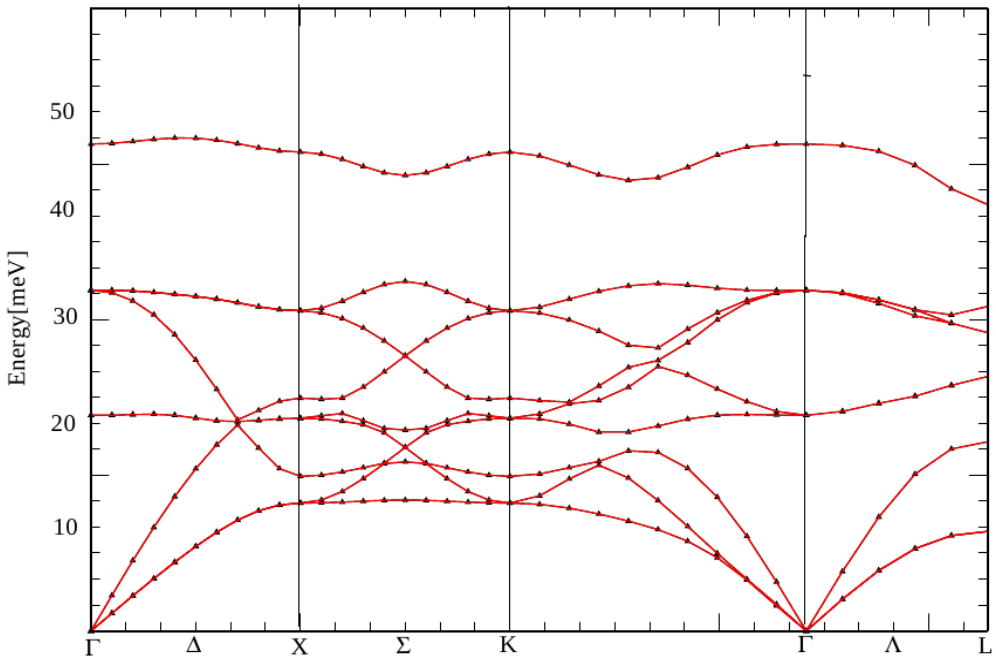


**Figure 5.4: Phonon dispersion curves for c-$BaF_2$ obtained from *ab initio* DFT theory.**

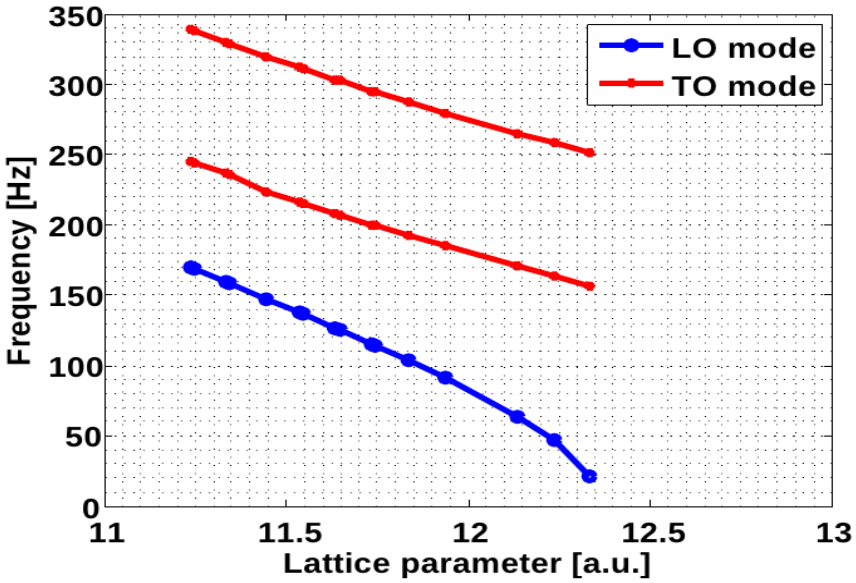


**Figure 5.5: Variation of Frequency versus lattice parameter.**

for the three vibration modes were computed to be $\omega_{TO}$=137.61cm$^{-1}$, $\omega_{Raman}$= 216.15cm$^{-1}$ and $\omega_{LO}$=311.81cm$^{-1}$. Available experimental values for phonon frequencies at 300K are $\omega_{TO}$=189cm$^{-1}$, $\omega_{Raman}$= 241cm$^{-1}$ and $\omega_{LO}$= 330cm$^{-1}$. These results are compared in Table 5.3, where it was established that although our values were under-estimated for all the three modes of vibration when compared to experimental ones, the trends are well reproduced, with $\omega_{TO}$ being the lowest in all cases and $\omega_{LO}$ is the highest mode. Phonons are known to be sensitive to pseudopotentials and our use of GGA and a convergence value that was not too small ($10^{-8}$ Hartree) are some of the expected reasons for the noticeable deviations from the experimental values. Vibrations at high temperature are expected to be higher than ours done at 0 K.

**Table 5.3: Theoretical and experimental optical gamma-point frequencies (in $cm^{-1}$).**

| Method | $\omega_{TO}$ | $\omega_{LO}$ | $\omega_{Raman}$ | Ref. |
|---|---|---|---|---|
| QE (GGA) | 137.61 | 311.81 | 216.15 | Present |
| ABINIT | 199.34 | 351.46 | 252.03 | [30] |
| Exp.(300 K) | 189.00 | 330.00 | 241.00 | [30] |

Normally when frequencies increase, the inter-atomic forces are weakened and the modes soften. As such, rates of weakening of modes depend linearly on the frequency modes at low frequency but exponentially, at higher frequencies as shown in Figure 5.3. Critical softening occurs beyond melting especially when further anharmonic processes contributing to phonon frequencies are ignored. The slopes of the curves, which in this case shows the increase in lattice parameter, agree with those of Schmalzl et al [30]. This shows that phonon-phonon processes contribute to the temperature shift of the $\Gamma$ - point frequencies. A plot of the frequency, $\omega$ vs lattice constant $a$ as seen in fig. 5.3 deviates from linearity due to further anharmonic contributions. The finding of this study compares well to those of $CaF_2$ [115] which shares the fluorite structure with $BaF_2$. Softening at X-point (and not $\Gamma-$ point) has been connected to transition to the superionic state of the fluorite system. In particular, softening is attributed to reduced restoring forces acting on

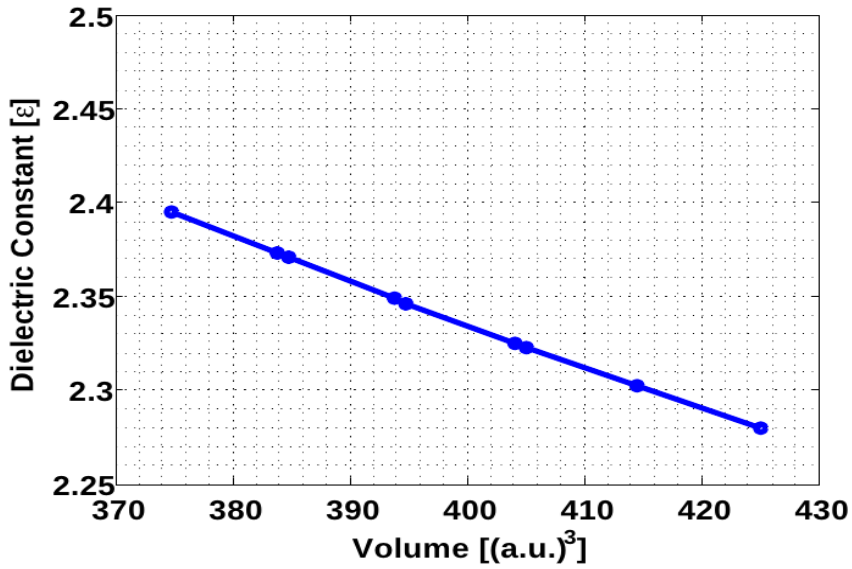


**Figure 5.6: Dielectric Charge variation with volume of $c-BaF_2$.**

displaced $F^-$ ions. In addition reduced barriers may also support individual $F^-$ ions hopping and this may lead to more mobile anions.

Table 5.3 shows the effective charge $z^*$ and high frequency dielectric constant of c-$BaF_2$ while fig. 5.3, shows the variation of dielectric constant with volume of c-$BaF_2$. Increase in volume reduces the inter-ionic forces thereby reducing the

**Table 5.4: Effective charge $z^*$ and high frequency dielectric constant $\epsilon_\infty$ of c-$BaF_2$.**

| Method | a(Å) | $z^*$ | $\epsilon_\infty$ | Ref. |
|---|---|---|---|---|
| QE(GGA) | 6.100 | 2.660 | 2.396 | Present |
| ABINIT | 6.050 | 2.634 | 2.472 | [30] |
| Exp.(300 K) | 6.184 | | 2.167 | [30] |
| WIEN97 | 6.233 | | 2.129 | [30] and ref. therein |

dielectric constant $\varepsilon$. In the case of $BaF_2$ electrons of Ba are more long-range in nature and thus more polarizable than in Ca, thus resulting in a more polarizable system and consequently into a slightly lower dielectric constant of 2.396 for $BaF_2$ which compares to 2.4 for $CaF_2$[115]. Calculated effective charge in this work was

$Z^* = 2.66$ but the experimental value is not available for comparison. The value obtained in this study compares well to those obtained using ABINIT and CRYSTAL calculations, which are 2.63 and 1.90, respectively although the one obtained from ABINIT is much lower by 36.8% [30]. The computed high-frequency dielectric constant, $\varepsilon_\infty$ of c-$BaF_2$ was 2.396, a value that agrees well to the experimental one at 300K of 2.167 while that obtained from ABINIT was 2.472. Results for WIEN97 were not available for comparison. Both calculations overestimate the dielectric constant by 9.6% and 12.3% in comparison to experiment and this is attributed to the inherent approximations made in the theory.

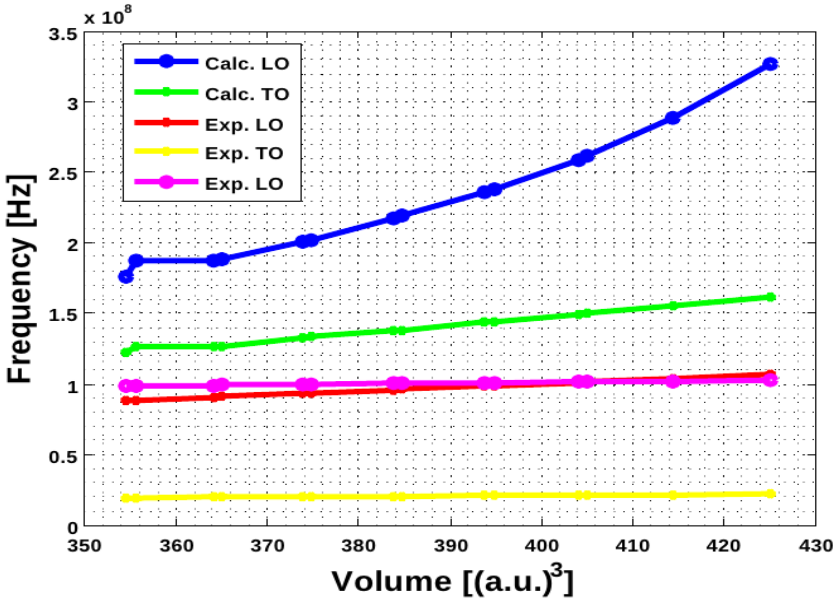


**Figure 5.7: Frequency dependence on volume.**

Figure 5.3 shows a variation of volume changes in c-$BaF_2$ with vibrations, whereby such changes are related with temperature. In particular, an increase in temperature results in an increase in volume and in this study, it was found out that at about 400 a.u.$^3$, there was a sudden increase in volume for all the three modes of vibrations. This implies that the shape and size of the crystal changes when the frequency applied is enough to expand the volume to about this size.

A good understanding of the variation of volume with vibration can therefore help in determining the melting point of a material and in this case $BaF_2$, as well as some of its thermal properties. However, this only applies to low temperature cases, where harmonic approximation is applicable, otherwise anharmonic terms will be required, and these are beyond the scope of this study.

### 5.4 Elastic Constants

Table 5.4 shows the elastic constants of the cubic phase of $BaF_2$ calculated using different theoretical methods as explained in section 4.3 and the results were compared with experimental data in all cases unless otherwise stated. Although

**Table 5.5: Elastic constants in gigapascals of cubic phase of $BaF_2$. The results are compared with other theoretical results and experimental ones.**

| Method | $C_{11}$ | $C_{12}$ | $C_{44}$ | Ref. |
|---|---|---|---|---|
| Quantum espresso | 88.20 | 34.3 | 19.6 | Present |
| ABINIT | 112.40 | 64.89 | 28.76 | [30] |
| Expt(300K) | 91.22 | 41.48 | 25.51 | Ref.[30] and refs. therein |
| Expt (0K) | 98.10 | 44.81 | 25.44 | Ref.[30] and refs. therein |

several works [30] have investigated the elastic constants of c-$BaF_2$, it was still necessary to calculate these values in the current work so as to validate the calculated elastic constants for the other phases of $BaF_2$ where experimental results were unavailable. Our calculated elastic constants for the cubic phase compare quite well with those of other works. For example, compared to the ABINIT calculations, our errors were lower relative to experimental data. In particular, the deviations for the $C_{11}$ constant in our case was 3.2% while that of ABINIT was $\sim$ 23%, compared to experimental value. For the $C_{12}$, our value deviated by 17% while that of the ABINIT value was 56% higher than the experimental one. Our $C_{44}$ value deviated by 23% compared with 13% for ABINIT from the experimental value. These deviations are occasioned by the fact that our use of GGA pseudopotentials gives lower values of the elastic constants.

Figure 5.4 shows the plots used to obtain parameters needed in the computation of the elastic constants for the cubic phase of $BaF_2$ while figs. 5.4 and 5.4 were used to calculate the elastic constants for the orthorhombic and hexagonal phases of $BaF_2$, respectively. Each one of the three figures shows the parabolic shape predicted by their respective equations as explained in chapter 4.

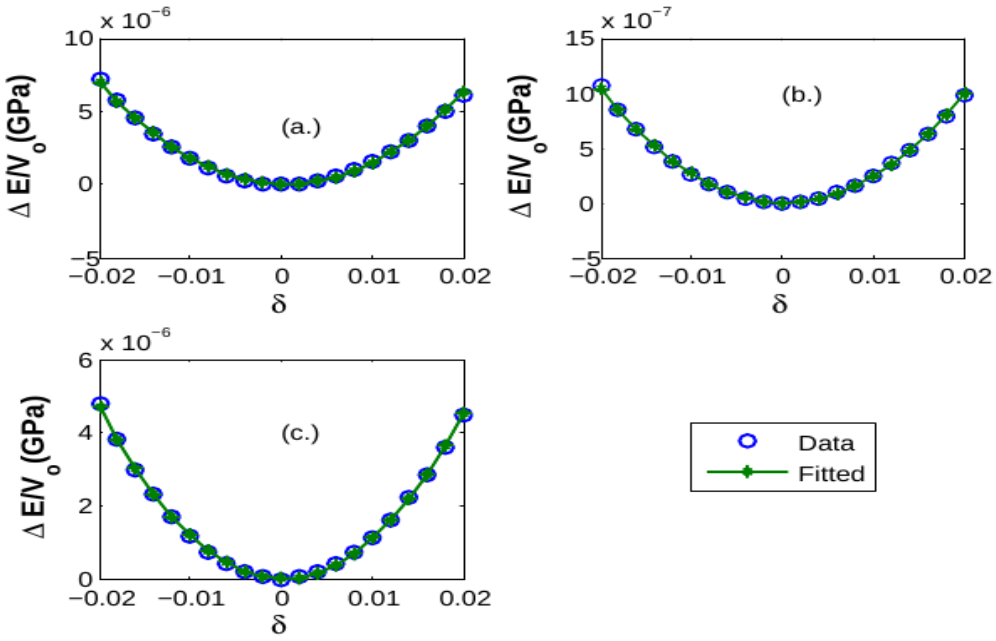


**Figure 5.8: Changes in the pressure ($\Delta E/V_o$) as a function of the strain ($\delta$) for the cubic phase of $BaF_2$. The open circles represent the calculated values and the solid lines are the polynomial fit. Fig (a) is to estimate $C_{44}$, fig (b) is for $C'$ and fig (c) is for bulk modulus $B$.**

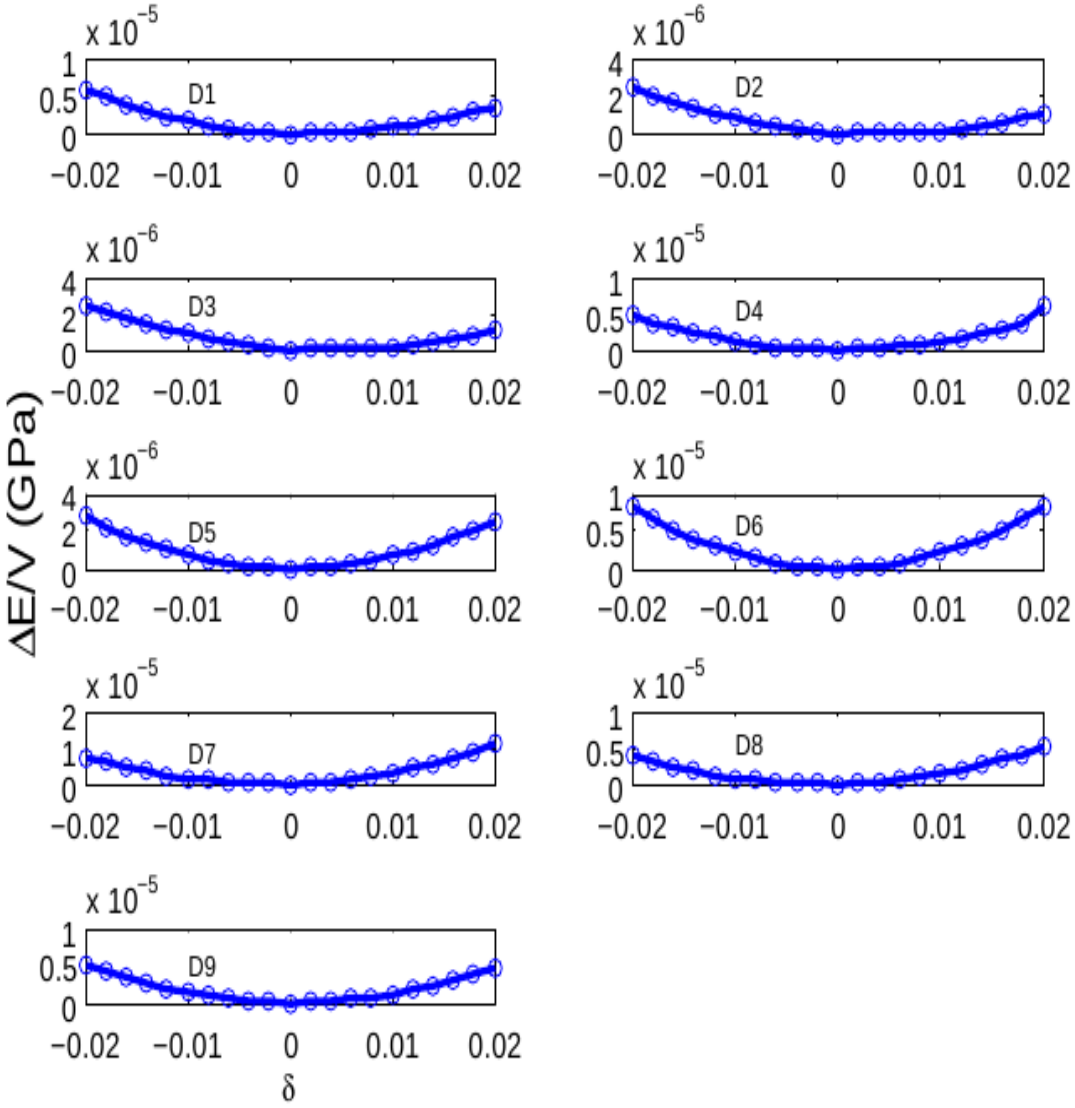


**Figure 5.9: Changes in the pressure ($\Delta E/V_o$) as a function of the strain ($\delta$) for the orthorhombic phase of $BaF_2$. The open circles represent the calculated values and the solid lines are the polynomial fit. $D_1$ to $D_9$ corresponds to the matrices given in section 4.3.2.**

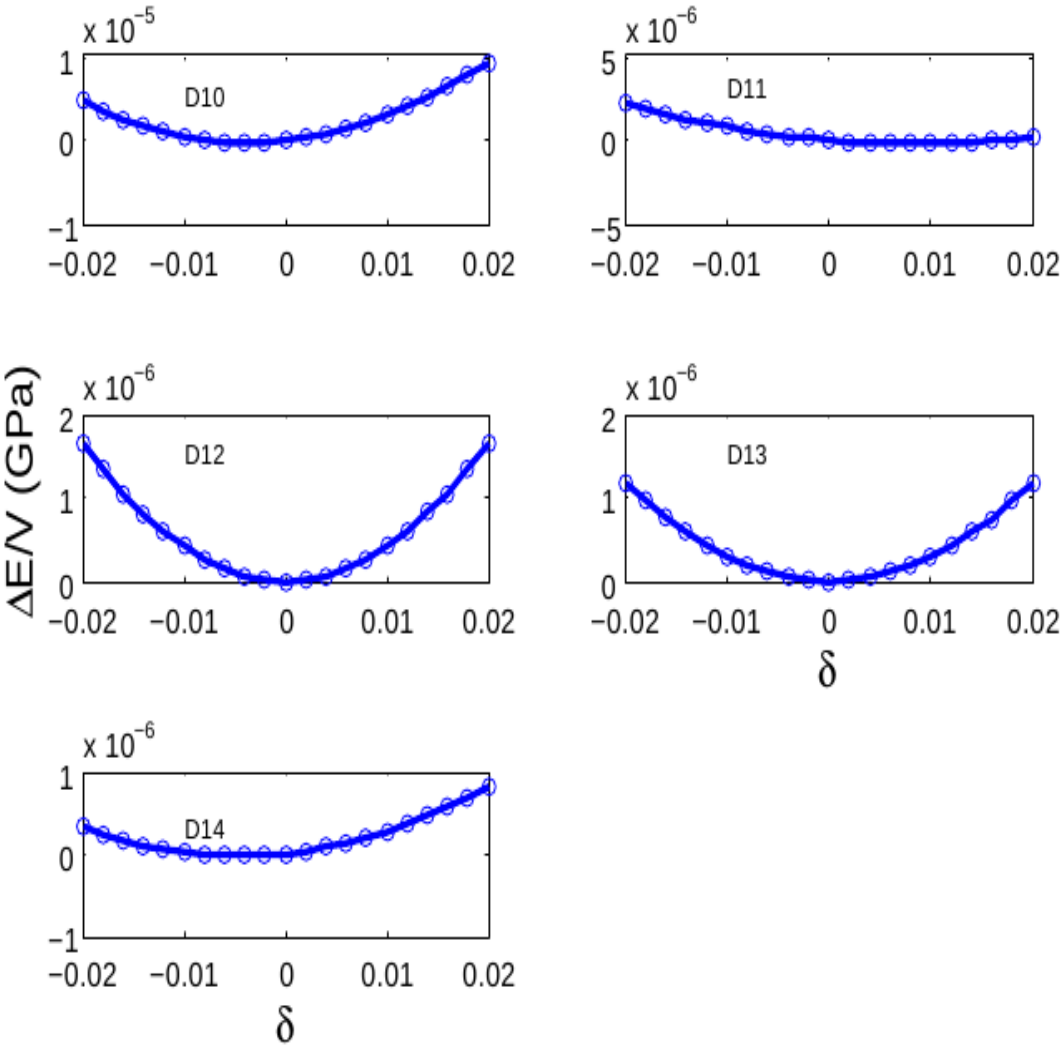


**Figure 5.10: Variation of Pressure ($\Delta E/V$) versus Strain $\delta$ for the calculation of elastic constants of the hexagonal phase of $BaF_2$. The open circles represent the calculated values and the solid lines are the polynomial fits while $D_1$-$D_{10}$ (section 4.3.3) represent the distortion matrices used in each case.**

**Table 5.6: Elastic constants for orthorhombic phase of $BaF_2$ given in GPa.**

| Elastic constant | $C_{11}$ | $C_{22}$ | $C_{33}$ | $C_{44}$ | $C_{55}$ | $C_{66}$ | $C_{12}$ | $C_{13}$ | $C_{23}$ |
|---|---|---|---|---|---|---|---|---|---|
| Quantum espresso | 275.5 | 346 | 126 | 91.7 | 47.2 | 147.5 | 32 | 39 | 60 |

Table 5.4 shows the values of the elastic constants for the orthorhombic phase of $BaF_2$. When compared to either the cubic or the orthorhombic phases of $BaF_2$, the hexagonal phase was found to have the largest values of the independent elastic constants $C_{11}$ and $C_{12}$ (see Tables 5.4, 5.4 and 5.4). Eqns. (4.36)-(4.41) show the formulae used for determining the bulk modulus. From table 5.4, the hexagonal phase has a bulk modulus of 161 GPa compared to 53.5 GPa and 108.8 GPa for the cubic and orthorhombic phases (see Tables 5.4.1 and 5.4.1), respectively. These suggest that the hexagonal phase is the most stiff of the three phases, confirming earlier observations of Jiang et al [11].

The derived bulk modulus from the elastic constants for the orthorhombic phase was found to be 94.5 GPa and by using the Murnaghan equation, the bulk modulus is 108.8 GPa. Jiang et al [11] calculated a value of 98 GPa. The deviation in these values of elastic constants in this current work can be attributed to estimations made in deformation formulae. This is because an independent elastic constant is a combination of many other constants which when estimated over-estimates or underestimates the final result. Given that the deviation is not much shows that the methods used in the calculation of the elastic constants in this current work were accurate.

**Table 5.7: Calculated bulk moduli for the cubic, the orthorhombic and the hexagonal phase of $BaF_2$ given in GPa compared with other approaches.**

| Bulk modulus | Cubic | Orthorhombic | Hexagonal |
|---|---|---|---|
| Present work (Murnaghan equation method) | 53.5 | 108.8 | 154 |
| Present work (using elastic constants) | 53.5 | 94.5 | 161 |
| LDA ([11]) | 57 | ... | ... |

**Table 5.8: Calculated elastic constants for the hexagonal phase of $BaF_2$ given in GPa.**

| Elastic constant | $C_{11}$ | $C_{12}$ | $C_{33}$ | $C_{55}$ | $C_{13}$ |
|---|---|---|---|---|---|
| Present work | 460 | 399 | 41 | 21.7 | 138.5 |

Table 5.4, shows that both the $C_{11}$ and $C_{12}$ values for the hexagonal phase were higher than those of the cubic phase of $BaF_2$. Using the elastic constants, a value of 161 GPa was obtained for the bulk modulus of hexagonal $BaF_2$ whereas the value obtained by fitting the values of energy and volume to the Murnaghan equation of state was 154 GPa. This indicates only a small deviation between values obtained using the two approaches. Xiaocui et al [33] have reported that the independent elastic constants $C_{11}$, $C_{12}$ and $C_{44}$ for $BaF_2$ increases with pressure, a property that is clearly confirmed by this present work since the elastic constants increase from cubic to orthorhombic to the hexagonal phase. These phases vary with pressure increase as has been shown in the Schmalzl et al [30].

### 5.4.1 Stability Parameters

The stability of a material can be obtained using constant $A$, which is obtained from eqn.(4.27). This parameter is also called the anisotropy parameter and when it is less than unity, the material is said to be anisotropic and vice versa. Table 5.4.1 gives the values of stability parameters of the cubic phase of $BaF_2$ whereby an anisotropy parameter $A = 0.727$ is obtained, compared to the one obtained using ABINIT code of 1.21 [33]. $BaF_2$ in cubic phase shows that it is anisotropic while ABINIT methods show that it is isotropic. It would be difficult to conclude exactly whether it is anisotropic or isotropic unless a third method is used to confirm.

**Table 5.9: Stability properties of cubic phase of $BaF_2$.**

| Phase | A | $\xi$ | $\Delta E_{Ba-F}$ in eV | Bulk Modulus B (GPa) |
|---|---|---|---|---|
| Cubic (present) | 0.727 | 0.56 | 24.87 | 53.5 |
| Cubic (ABINIT) | 1.21 | 0.732 | ... | ... |

**Table 5.10: Stability properties of orthorhombic and hexagonal phases of $BaF_2$.**

| Phase | $A_1$ | $A_2$ | $A_3$ | Bulk Modulus B (GPa) |
|---|---|---|---|---|
| Orthorhombic | 1.13 | 0.54 | 0.86 | 108.8 |
| Hexagonal | 0.015 | 0.023 | ... | 161 |

The fact that anisotropy parameter for the cubic phase of $BaF_2$ is less than unity shows that this phase is anisotropic. Other values shown in this table are the stiffness constant $\xi$ which gives the displacement of atoms from the central forces whereby, the smaller the value, the greater the displacement. In this calculation, the stiffness parameter for c-$BaF_2$ was 0.56 which was less than the value of 0.732 obtained earlier using the ABINIT computer code [116]. This value therefore shows that there is more displacement of atoms from the central forces than in the case of the ABINIT's calculation though the difference is within acceptable range.

The stability parameters for the orthorhombic and hexagonal phases are given in Table 5.4.1, whereby the orthorhombic phase is found to be less anisotropic (A$>$ 1), especially when the value of $A_1$ is compared to $A_2$ and $A_3$. Also from these calculations, the hexagonal phase was found to be more anisotropic ($A < 1$) as compared to the cubic or even the orthorhombic phases and in particular, in the $A_1$ ($\langle 100 \rangle$) and $A_2$ ($\langle 110 \rangle$) directions. Apart from the $A_1$ direction of the orthorhombic phase which is isotropic, all the other cases show that $BaF_2$ is generally an anisotropic material, with the value of the stability constant, $A$, being less that unity.

## 5.5 Defects

In this section, the theory derived in sections 2.2 and 3.10 is applied to calculate the formation energies of point defects in $BaF_2$. These defects are treated as either neutral or charged. While neutral defects are treated as periodic, a charged system is treated aperiodic as explained in section 3.10. This section also reports on the analysis of migration energies for both cations and anions in $BaF_2$.

### 5.5.1 Interstitial and vacancy formation energies

In this study, an octahedral site, two bridge sites and four-fold hollow sites were considered in the calculations of the interstitial formation energies as mentioned earlier. The values of the formation energies are shown in Table 5.5.1.

**Table 5.11: Interstitial and vacancy formation energies of $BaF_2$ in eV.**

| Ion | Interstitial | Vacancy |
|---|---|---|
| Ba | 3.14 | 15.64 |
| F | -0.62 | 8.73 |
| $Ba^{+2}$ | -18.28 | 21.27 |
| $F^-$ | 2.49 | -1.06 |

The study revealed that the anion was more stable in an octahedral site, which was in agreement with other studies done earlier on the interstitial position of F in $CaF_2$ [109] and therefore all calculations for the formation energies were done at the octahedral site. The formation energies of atoms bonded at octahedral sites were found to be -0.62 eV and 3.14 eV for F and Ba, respectively, as shown in Table 5.5.1. The more negative the energy, the easier it takes to form such a defect. It is therefore easier to form a neutral flourine interstitial than barium.

The vacancy formation energies were calculated as 8.73 eV for F and 15.64 eV for Ba. Due to the low formation energies of $F^-$ anions, this study suggests that F easily diffuses through the c-$BaF_2$ in comparison to Ba since the vacancy formation energy of a $F^-$ was lower than that of $Ba^{2+}$ by 6.91 eV. The vacancy formation energies were also greater than those of the same ions in $CaF_2$, which

were 15.64 eV for Ba compared to 13.75 eV for Ca cation. The value for $CaF_2$ anions was 8.34 eV against 8.73 eV for $BaF_2$. This difference between formation energies of $BaF_2$ and $CaF_2$ was attributed to the varied cation sizes between the cations of $CaF_2$ and $BaF_2$.

In addition to the defects considered so far, Frenkel defects are also possible in c-$BaF_2$ and these are defect pairs consisting of an interstitial and a vacancy created by the displacement of an atom from its stable crystal site to a different location in the crystal. The new position can be infinitely far or within a close neighbourhood. Charged cation and anion interstitial formation energies are given as -18.28 eV and 2.49 eV, respectively while vacancy formation energies for charged cation and anion are 21.27 eV and -1.06 eV, respectively. For neutral species, the Frenkel defect formation energies for $BaF_2$ are shown in Table 5.5.1. Anion-Frenkel formation energy of such a system at infinite separation was calculated to be 8.11 eV, while cation-Frenkel energy was 18.78 eV. For close separation, the values were calculated as 4.05 eV and 1.42 eV for cation and anion, respectively. Fig.

**Table 5.12: Frenkel formation energies for neutral cation and anion in cubic $BaF_2$ in eV.**

| Method | Cation Frenkel | Anion Frenkel |
|---|---|---|
| Present (infinite separation) | 18.78 | 8.11 |
| Present (close separation) | 4.05 | 1.42 |
| Experimental [117] | ... | 1.81 |

5.5.1 shows the calculated values of the interstitial formation energy for F and $F^-$ as a function of the Fermi energy. In this figure, the values of the interstitial formation energy for F and $F^-$ as a function of the Fermi energy are shown. In the case of neutral F the formation energy is independent of $E_F$ and is found to be -1.29 eV. For all values of $E_F$ however we find that $F^-$ is more stable than its neutral counterpart. We therefore conclude that the anion interstitial in $BaF_2$ is negatively charged.

As shown in Table 5.5.1, the formation energy of neutral F is -0.62 eV and this was independent of Fermi energy $E_F$. Some of the tables used in plotting figures

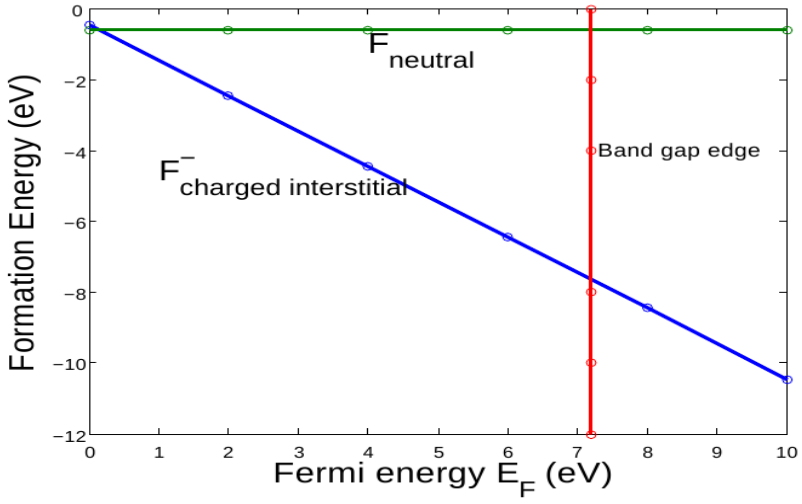


**Figure 5.11: Formation energy as a function of Fermi energy for F and $F^-$ interstitial defects in $BaF_2$.**

5.5.1 to 5.5.1 are shown in Appendix A. In fig 5.5.1, the vacancy formation energies of F and $F^-$ are plotted against the Fermi energy. The vacancy formation energies of the anion were calculated by removing a F atom or $F^-$ ion.

The findings of this study showed that the positively charged vacancy ($Ba^{2+}$) was more stable than the neutral anion in a large range of values up to about 6 eV. Since the calculated band gap was 7.2 eV, it was clear that the fluorine vacancy was positively charged except when the bulk was donor-rich.

Interstitial and vacancy formation energies for Barium are shown in figs 5.5.1 and 5.5.1, respectively. With respect to the Fermi level of $BaF_2$, it was observed that the formation energy of the $Ba^{2+}$ interstitial was lower than that of the neutral cation (see fig.5.5.1). The same case applied to the Ba vacancy where the charged vacancy $Ba^{2+}$ was more stable than the neutral vacancy Ba (see fig.5.5.1). Based on these observations, it was therefore concluded that the interstitial and the vacancy exist as charged species.

In the charged system and in the limit of infinite separation between vacancy and interstitial, the formation energy of a Frenkel defect is obtained by summing the formation energies of the interstitial and vacancy. It is thus argued from figs

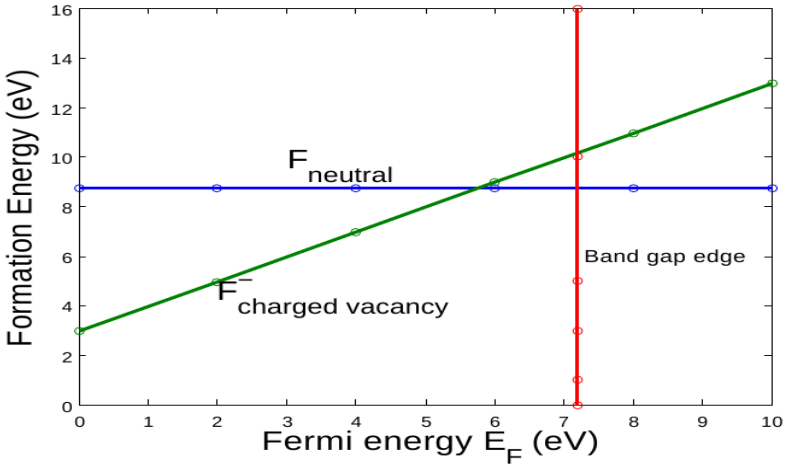


**Figure 5.12: Vacancy formation energies of anion as a function of Fermi energy for F and $F^-$.**

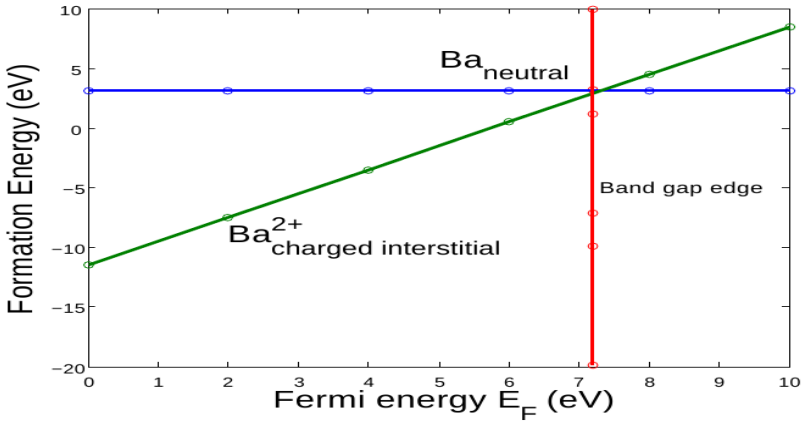


**Figure 5.13: Interstitial formation energies as a function of Fermi energy for Ba and $Ba^{2+}$.**

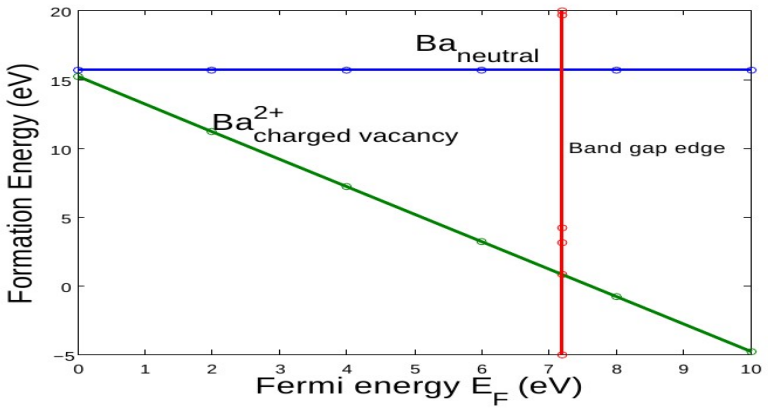


**Figure 5.14: Vacancy formation energy as a function of Fermi energy for Ba and $Ba^{2+}$ vacancy defects in $BaF_2$.**

5.5.1 and 5.5.1 that the flourine Frenkel defects are always composed of charged pairs, except when the Fermi level is close to the conduction band minimum $\sim 6$ eV, in which case the interstitial is charged and the vacancy is neutral. The formation energy of the F Frenkel defect was found to be 2.33 eV (see eqns.(A.0.13) and (A.0.14)) and approximately in the range of 0.8 eV when the Fermi level is close to the conduction band minimum. Using eqn.[5.1], $E_V$ is 4.09 eV and the Fermi energy $E_F$ is 4.83 eV (See Appendix B).

$$\Delta E = 21.27 + 0.45 - q(E_V + E_F). \tag{5.1}$$

This gives formation energy of 3.90 eV and these values compare reasonably well with the experimental data of Katsika [117] in ionic conductivity measurement who obtained a value of 5.9 eV. They are also in agreement with the calculation of the formation energies of the neutral Frenkel defects of Ref. [109].

Frenkel defects were also calculated with the interstitial and vacancy defects separated by one or two nearest-neighbour distances. It was found that when the interstitial was placed in an octahedral site adjacent to the vacancy site, the

atomic configuration was unstable and always relaxed back to the ideal crystal lattice. On the contrary, when the interstitial was placed in the second-nearest octahedral site from the vacancy site the atomic configuration was locally stable for the cation and it was still unstable for the anion. The anion became locally stable only when it was placed in the third nearest neighbour. The formation energies of the locally stable configurations were 1.4 eV for the anion and 4.1 eV for the cation. When these values were compared with the values obtained for the Frenkel defects at infinite separation, it was found that the cation Frenkel defects preferred to separate at distances larger than the second-nearest neighbour positions once formed, while the anion Frenkel defects preferred to reside at finite separation when formed.

### 5.5.2 Vacancy migration energy

Figure 5.5.2 shows the migration energy plotted against the migration path $\langle 100 \rangle$ for the anion $F^-$ vacancy. Although this is a plot for the anion, a similar graph is expected to be obtained for the cation ($Ba^{2+}$) but with different energy values.

The maximum energy point **S** is the saddle point and this is the only available migration energy available experimentally as shown in Table 5.5.2. Other directions may be difficult to measure experimentally though theoretically this can be attained as our data shows. Other directions are probably difficult to measure and therefore simulation becomes an appropriate tool. This is also the least vacancy migration energy in these calculations and is therefore the most preferred route for anion vacancy.

Vacancy migration energies were calculated for the anion ($F^-$) diffusion along three low index crystallographic directions, $\langle 100 \rangle$, $\langle 110 \rangle$, and $\langle 111 \rangle$, respectively (see Table 5.5.2). Similar to $CaF_2$, the lowest barrier for diffusion for the $F^-$ vacancy in $BaF_2$ was found to be along $\langle 100 \rangle$ (0.53 eV) a value that was in good agreement with experimental data (0.59 eV Ref.[117]). Anion vacancy migration energies in the $\langle 110 \rangle$ and $\langle 111 \rangle$ directions were established to be 1.17 eV and 1.15

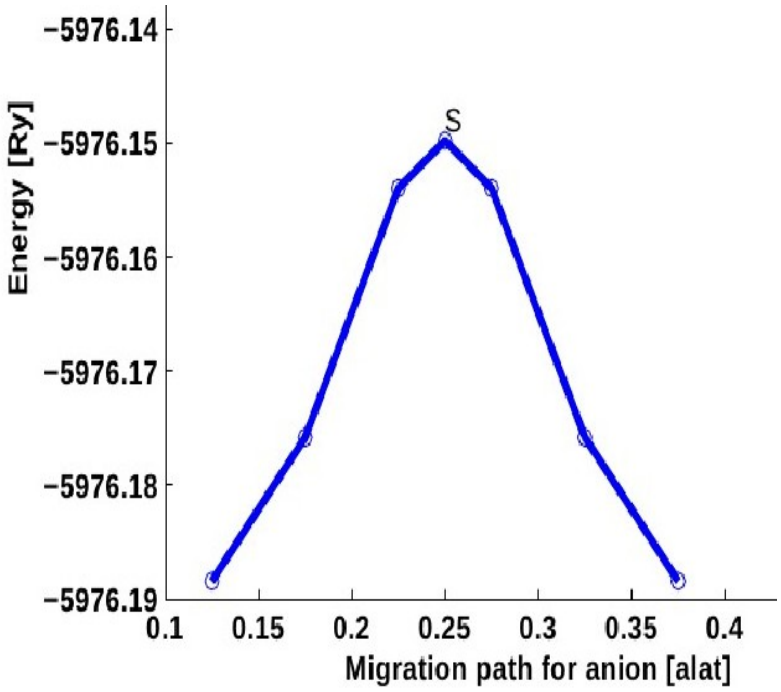


**Figure 5.15: Variation of anion vacancy migration energy with migration path $\langle 100 \rangle$. The saddle point S is the maximum energy point in this direction. The dots are the energy level against position joined by the line for all positions along the direction $\langle 100 \rangle$.**

**Table 5.13: Vacancy migration energy for cation $V_{Ba}$ and anion $V_F$ for $BaF_2$ in eV.**

| Direction | Present | Experimental |
|---|---|---|
| $V_F\langle 100 \rangle$ | 0.53 | 0.59 [117] |
| $V_F\langle 110 \rangle$ | 1.17 | ... |
| $V_F\langle 111 \rangle$ | 1.15 | ... |
| $V_{Ba}\langle 100 \rangle$ | 2.22 | ... |

eV, respectively, suggesting that these directions had almost equal energy.

Cation migration energy was only possible in the $\langle 100 \rangle$ direction. The $\langle 110 \rangle$ and $\langle 111 \rangle$ directions were found to be unlikely since the cation was moving too close to the anion when near the saddle point. It was thus concluded that the large size of $Ba^{2+}$ (ionic radius of 1.49 Å), prevents the cation from diffusing easily along either $\langle 110 \rangle$ or $\langle 111 \rangle$ directions. For example, a linear path along the $\langle 110 \rangle$ direction brings Ba at a distance of approximately 1.5 Å from the nearest fluorine.

As a result the migration energy was calculated only along the crystallographic direction $\langle 100 \rangle$, and it was found to be 2.22 eV. This was unlike recent calculations for $CaF_2$ where cation migration energies in the $\langle 100 \rangle$ and $\langle 110 \rangle$ directions were found to be 4.62 eV and 3.93 eV, respectively [109]. Therefore, for $CaF_2$, the $\langle 110 \rangle$ direction has least energy for cation migration, and this is presumably due to the substantial difference between the ionic radius of $Ba^{2+}$ (1.49Å) and $Ca^{2+}$ (1.14 Å).

## 5.6 Potentials for $BaF_2$

In sections 3.11.6 and 3.11.7, the process of fitting the parameters of classical molecular dynamics into those of *ab initio* calculations was discussed. The force marching process was done to bring as close as possible the forces, stresses and energies of the classical model to those obtained using the *ab initio* approach. This minimization process was stopped at an overall minimum value of 17%. For the forces, the required accuracy of 30% was attained, while for stresses it was 17% and 12% for the energies. The main parameter generated in this fitting process was the potential or in broader sense the force field.

### 5.6.1 Force Field and Phase Transition

The force field parameters generated using the ASAP code [99] are given in Table 5.6.1 whereby the data is related to eqns.(3.81), (3.82) and (3.83). The charge q for Ba was taken to be 1.612 C while for flourine it was -0.806 C. These values were close to the exact charge values of 2 and -1 C for Ba and F anions, respectively, and hence found suitable for the simulations.

**Table 5.14: Force field parameters for $BaF_2$. $q_F$ is charge of flourine and $q_{Ba}$ charge of barium. $D_{F-F}$, $D_{Ba-F}$ and $D_{Ba-Ba}$ are parametrization constants between F-F, Ba-F and Ba-Ba atoms, respectively. $\gamma_{F-F}$, $\gamma_{Ba-F}$ and $\gamma_{Ba-Ba}$ are the short range polarization parameters, respectively. $r_{F-F}$, $r_{Ba-F}$ and $r_{Ba-Ba}$ are the distances between different atoms and $\alpha$ is the polarization constant. The constants $b$ and $c$ are fitting parameters of the model.**

| $q_F$ | $q_{Ba}$ | $\alpha$ | $b$ | $c$ |
|---|---|---|---|---|
| -0.80595 | 1.61189 | 4.8281427 | 1.76615 | 3.86333 |
| $D_{Ba-Ba}$ | | $D_{Ba-F}$ | | $D_{F-F}$ |
| 1.7294x$10^{-2}$ | | 1.2765x$10^{-3}$ | | -8.2344x$10^{-02}$ |
| $\gamma_{F-F}$ | | $\gamma_{Ba-F}$ | | $\gamma_{Ba-Ba}$ |
| 7.0831 | | 8.4838 | | 5.5049 |
| $r_{F-F}$ | | $r_{Ba-F}$ | | $r_{F-F}$ |
| 4.6597 | | 8.0098 | | 3.6812 |

The comparison between the structural parameters of molecular dynamics of c-$BaF_2$ and those obtained from density functional theory are given in Table 5.6.1.

**Table 5.15: Lattice parameters and bond lengths obtained from molecular dynamics compared to DFT data for $BaF_2$. The DFT calculations used the steepest descent approximations.**

| | Molecular dynamics (Å) | DFT (Å) |
|---|---|---|
| lattice parameter, $a_0$ | 6.125 | 6.10 |
| Ba-Ba | 4.31 | 4.31 |
| Ba-F | 2.66 | 2.64 |
| F-F | 3.08 | 3.05 |

The results obtained from molecular dynamics simulations were found to be in good agreement with those obtained from the DFT calculations. The parameters shown in Table 5.6.1 were then used to run molecular dynamics simulation of $BaF_2$ in order to calculate some of its thermal properties. Some of these properties studied include the phase transition and melting point temperatures of $BaF_2$ which are important in determining the superionic transition temperatures. In fig 5.6.1, temperature dependence of the total energy is shown.

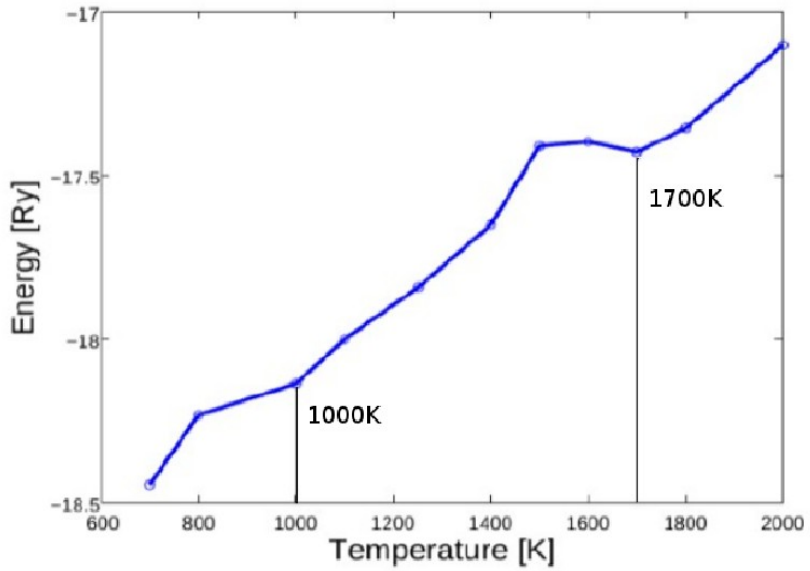


**Figure 5.16: The temperature dependence of the total energy of c-$BaF_2$.**

The variation of energy with respect to temperature is generally the specific heat capacity of the material. Figure 5.6.1 therefore shows that there are dips of phase transition, $C_p$, at T = 1000 K and melting temperature, $T_m$ = 1700 K. These two temperatures are lower than those calculated by Ivanov-shitz et al [12] which are reported as 1285 K and 1800 K, respectively. This difference is attributed to their use of classical molecular dynamics which tends to overestimate the melting point, since the experimental melting temperature of $BaF_2$ is 1641 K [118], a value which is much closer to our calculated value of 1700 K than the 1800 K predicted earlier by Ivanov et al [12]. The empirical potential constructed in this current work also considered the polarization effects which play an important role in the properties of flourides.

### 5.6.2 Ionic motion

At low temperatures, the cations and anions are in vibrational thermal motion, with the vibrational amplitude of the flourine atoms being higher than those of barium atoms due to their differences in sizes. Barium atoms continue vibrating in their equilibrium positions at higher temperatures while fluorine anions begin diffusing between nearest neighbour sites. It is therefore correct to assume that most of the thermodynamic properties of $BaF_2$ are as a result of the motion of the anions and to some extent this applies to other flourite structures e.g. $CaF_2$. In the following section we discuss the cation and anion motion using radial distribution function and anion motion using mean square displacement.

### 5.6.3 The Radial Distribution Function, g(r)

The radial distribution function gives the probability of finding a particle at a distance $r$ from another particle. In fig 5.6.3, the first (and large) peak occurs at around $r$ = 4.20 Å with the radial distribution function $g(r)$, having an intensity of about 2.25.

This value of 2.25 implies that it is 2.25 times more likely that two Ba-Ba ions

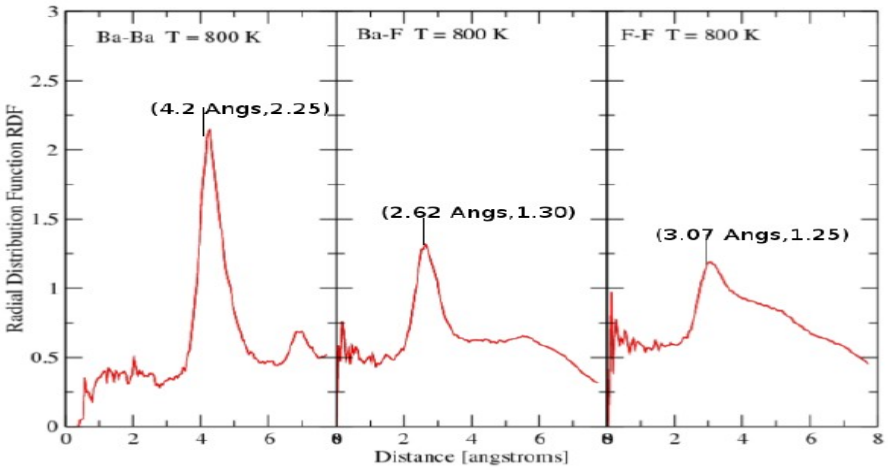


**Figure 5.17: The radial distribution function at 800 K. Both cation and anion are within their lattice site positions.**

would be found at this separation. This separation distance is in agreement with the value of 4.31 Å found from steepest descent calculations reported in Table 5.6.1. The distance between Ba-F is about 2.62 Å and that between F-F is 3.07 Å. At this temperature of 800 K and 1000 K as shown in fig 5.6.3, it was found that both ions were still vibrating at their mean lattice positions, since the Ba-Ba, F-F and Ba-F distances were unchanged. Radial distribution function on the other hand is reduced to 2.0 for Ba-Ba, 1.25 for Ba-F and 1.20 for 1.20. Figure 5.6.3

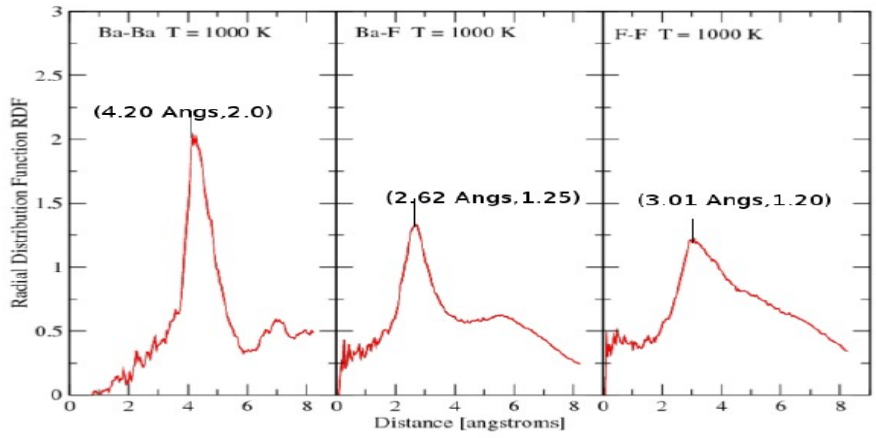


**Figure 5.18: The radial distribution function at 1000 K. Cations and anions are still in their mean lattice positions.**

gives the distance between Ba-F ions as about 2.62 Å with a low $g(r)$ (intensity) value of about 1.30 while the F-F distance at this temperature is 3.07 Å with a radial distribution function whose intensity is 1.25. The low intensity of F-F peaks when compared to those of Ba-Ba (2.25) and Ba-F (1.30) implies that flourine ions vibrate more and therefore the chances of finding F-F close to each other is the lowest. This is in agreement with the fact that anions diffuse more than the cations.

In figure 5.6.3 where the temperature is 1400 K, the distance between Ba-Ba appears still to be 4.2 Å but radial distribution function is reduced from 2.25 to 1.80. Ba-F and F-F radial distribution functions are 1.4 and 1.0, respectively.

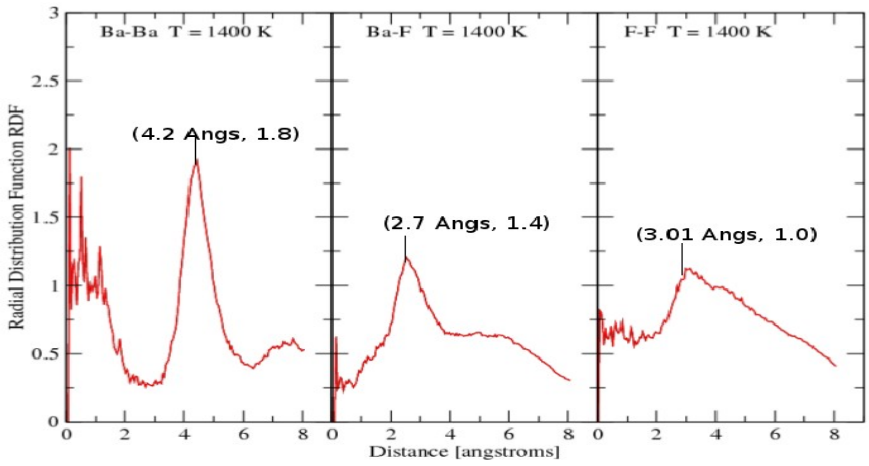


**Figure 5.19: The radial distribution function at 1400 K.**

Therefore, the chances of finding these two cations close to each other has somewhat reduced with increase in temperature. The intensity of Ba-F radial distribution function is below 1.4 at 1400 K while that of the F-F radial distribution function is below 1. (see Fig 5.6.3). It still appears that the distance between F-F is 3.01 Å. With the low radial distribution function and in comparison with mean square distribution discussed in sect. 5.6.3, it is apparent that flourine ions have started diffusing at 1000 K. In figures 5.6.3 and 5.6.3, it is seen that the intensity

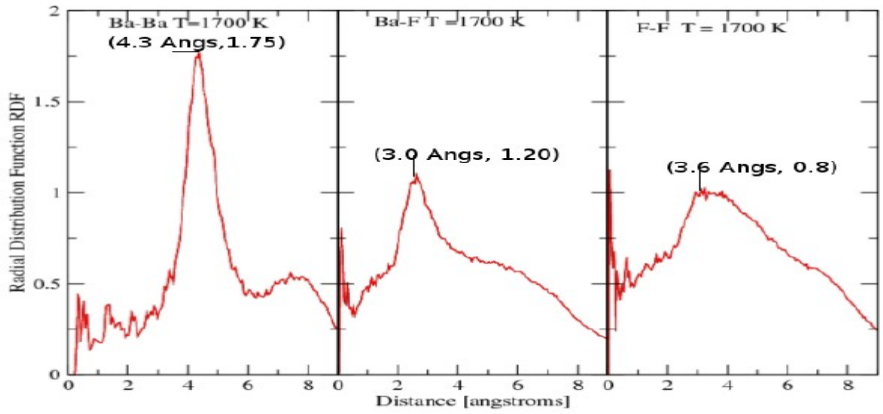


**Figure 5.20: The radial distribution function at 1700 K.**

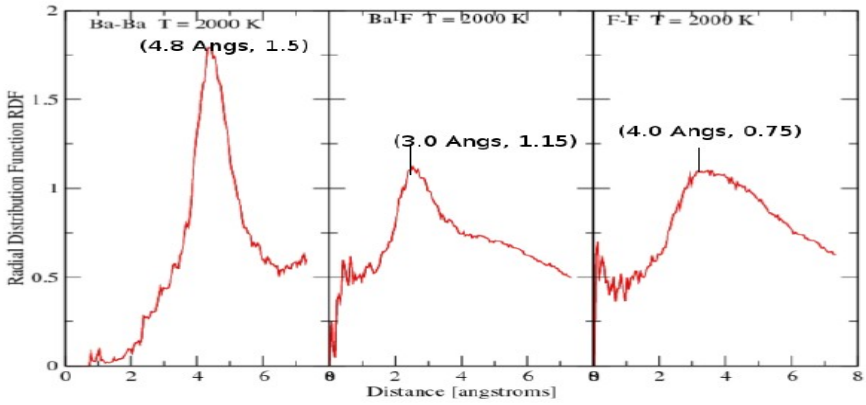


**Figure 5.21: The radial distribution function at 2000 K.**

of $g(r)$ for Ba-F and F-F is tending to one while that of Ba-Ba is at around 1.75. A radial distribution function of 1 indicates the absence of long-range forces. This is not the case in $BaF_2$ given that the interactions of cation-cation, cation-anion and anion-anion give values that are more than one even after melting point is achieved which is at 1700 K which is near experimental value of 1641 K. This is an indication of presence of long-range forces in $BaF_2$ which exists even after the F anions have transformed to molten form while Ba cations are still in their equilibrium lattice positions. This is in good agreement with classical molecular

dynamics reported by Ivanov et al [12].

### 5.6.4 Mean Square Displacement, MSD

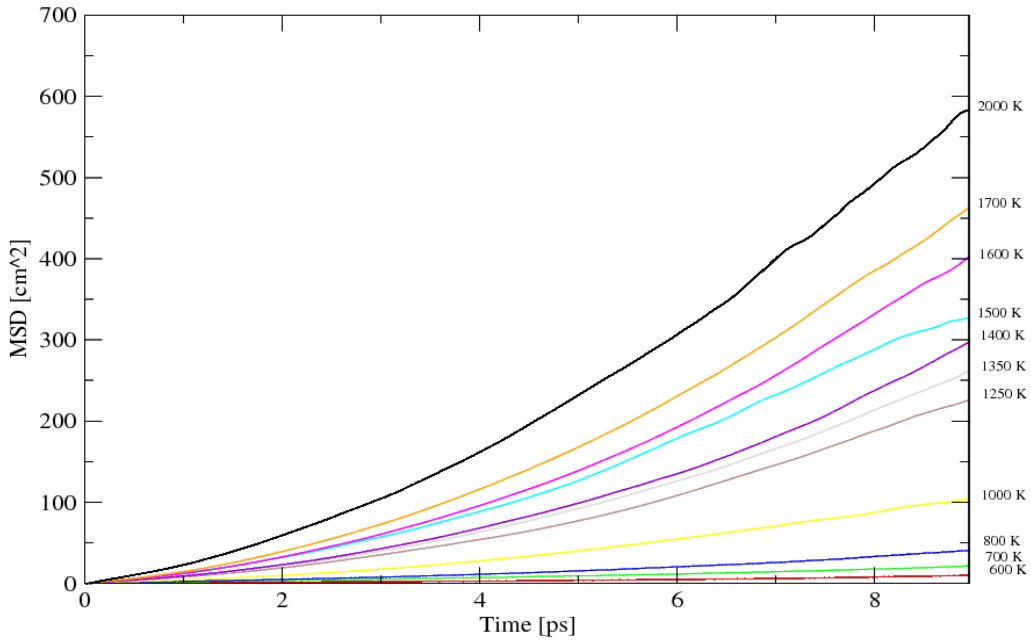


**Figure 5.22: Mean square displacement $\langle \triangle r^2 \rangle$ as a function of time in picoseconds.**

Fig. 5.6.4, shows a plot of the mean square displacement MSD against time. The figure shows that at about 1000 K, there is a jump which corresponds to the superionic phase transition predicted by this new potential. This value was in agreement with the results shown in fig 5.6.1 where superionic conductivity is predicted to start at 1000 K. There is another appreciable gap at 1700 K, which is in agreement with the results presented previously in fig 5.6.1 for the melting temperature of $BaF_2$. This gap is the liquid phase of $BaF_2$ where the anions are diffusing more freely.

This study reveals that the anions motion in the low-temperature phase of up

to 1000 K is vibrational in nature but are diffusing in the high temperature phase. The diffusion constant is in the range of 4.55x10$^{-5}$ cm$^2/s$ at 500 K to 1.52x10$^{-4}$ cm$^2/s$ at 1500 K. These values are typical of superionic conductors which is about $10^{-5}$ cm$^2/s$ [12].

# CHAPTER SIX

# CONCLUSIONS AND RECOMMENDATIONS

## 6.1 Conclusions

Electronic and mechanical properties of $BaF_2$ have been studied using density functional theory and density functional perturbation theory as implemented in the Quantum Espresso Computer code. Kinetic and thermodynamic properties were studied using molecular dynamics with parametrized force field. The new force field developed in this work is a major improvement from the other pair-wise potentials that have been used in other $BaF_2$ calculations.

The elastic constants for the cubic phase of $BaF_2$ were found to be in good agreement with both experimental and other theoretical works. All the elastic constants of the orthorhombic and hexagonal phases of $BaF_2$ have been calculated for the first time in this study. These values were used to calculate the bulk modulus of these phases and good agreement was established with other calculations. Stability of these phases show that the hexagonal phase has the least anisotropy in all directions indicating least stability. In fact, the anisotropy of this hexagonal phase was so low that it was nowhere near those of the cubic or even orthorhombic phases. This agrees well with the experimental findings which report that at about 17 GPa, $BaF_2$ exists only in hexagonal phase.

The calculated defect energies and vacancy migration energies show very good agreement with the available data. Most of the results were also found to be similar to those of calcium fluoride, since the electronic band structure of $BaF_2$ resembles that of $CaF_2$ although the atoms of $CaF_2$ are closer together than those of $BaF_2$. It was also established that the energy needed to create the cationic vacancy and interstitials for $BaF_2$ was greater than that needed to create an anion vacancy and interstitial. To create a cation vacancy requires five times more energy than to create a cation interstitial. Anion vacancy also required more energy to form than

anion interstitial. Anion formation energy was far much less than cation formation energy (-0.62 eV against 3.14 eV). Therefore it can be concluded that there was no cationic contribution to the conductivity of $BaF_2$ and this can be confirmed for other superionic materials also like in Ref. [35].

Cation Frenkel defects were found to be most stable at infinite separation while anion Frenkel defects were most stable in the third nearest neighbour. Charged Frenkel defects were more stable than neutral Frenkel defects for both cation and anion and they were locally stable only when the distance between vacancy and interstitial was at least 5 Å and 8 Å for cation and anion, respectively.

A major part of this study was to generate empirical potentials which were to be used in the molecular dynamics calculations of $BaF_2$. Molecular dynamics runs of $BaF_2$ containing 96 atoms were performed at a temperature of 1200 K to obtain the initial configurations for the fit. This temperature is close to the first transition temperature of $BaF_2$ and was appropriate for obtaining molten state of this material. The parameters from the classical molecular dynamics were matched to forces, stresses and energies from *ab initio* calculations using the force matching approach. This force matching was done until the percentage error between the parameters of *ab initio* calculations and those of the force field were small enough.

The new empirical potential generated was used to do a steepest descent run in order to obtain the lattice parameters and also the inter-ionic bond lengths. The values obtained were found to be in good agreement with experimental data as well as other *ab-initio* studies. These values confirmed that the current potential (developed in this study) was accurate and was therefore used to performe simulation of some of the thermodynamic properties of $BaF_2$.

The phase transition of $BaF_2$ was also investigated, and it was established that the superionic transition for this material is at about 1000 K. This value was found to be in agreement with earlier reports. The melting temperature was found to be at about 1700 K, which was close to the experimental value of 1641 K. This was a clear indication that the new potential was simulating the

thermodynamic properties of $BaF_2$ better than the classical potentials that have been used previously [12], which predicted a melting temperature of 1800 K.

Studies of the radial distribution function and mean square displacement showed that there were two positions of phase transition. These were superionic and melting point of $BaF_2$. The superionic transition was found to be due to anions which become more mobile just before melting.

## 6.2 Recommendations

It would be interesting to study the superionic properties of $BaF_2$ doped with Lanthanum or any other rare earth elements. Of more interest would be to look into the superionic properties of this doped $BaF_2$ with the parametrized force field. Classical molecular dynamics and electronic structure properties of flourites is known to improve by doping by trivalent atoms and there are possibilities of superionic transition temperature scaling down with introduction of a trivalent atom.

The experimental work by Ngoepe et al [119] has shown the change in transition temperature of $BaF_2$ when doped with $La^{+3}$. Theoretical studies of these transitions can be of interest since they have not been performed to the best of my knowledge.

Study of $H$ and $F$ centres can also be done on the doped $BaF_2$ as a follow up to the work done by Shi et al [120, 32].

In defects calculations, it can be more interesting to study the energetics of the trivacancy in this material. This is because in a radiation incident on a crystal more than one or two ions are displaced. This study can give real applications to compare the effect of irradiation on $BaF_2$.

## REFERENCES

[1] P. Schwerdtfeger, M. Dolg, W. Schwarz, G. Bowmaker, and P. Boyd, "Relativistic effects in gold chemistry. I. Diatomic gold compounds," *J Chem Phys*, (1989).

[2] Crankshaft, "Electronic properties of materials." `http://what-when-how.com/electronic-properties-of-materials.html`. Accessed July, 2012.

[3] B. Huang, J. Hong, Z. Xue, and X. You, "A novel $\beta$âĘŠ $\alpha$ phase transition of $PbF_2$ at ambient condition driven by fluoride ions," *Solid State Communications*, vol. **133**, no. 6, pp. 393–395, (2005).

[4] E. Morris, T. Groy, and K. Leinenweber, "Crystal structure and bonding in the high-pressure form of fluorite (CaF2)," *Journal of Physics and Chemistry of Solids*, vol. **62**, no. 6, pp. 1117–1122, (2001).

[5] K. Portella, K. Rattmann, G. De Souza, C. Garcia, M. Cantao, and R. Muccillo, "Characterization of $\alpha$ $\beta$ PbF2 phase transition by several techniques," *Journal of Materials Science*, vol. **35**, no. 13, pp. 3263–3268, (2000).

[6] N. Sata, K. Eberman, K. Eberl, J. Maier, *et al.*, "Mesoscopic fast ion conduction in nanometre-scale planar heterostructures," *Nature*, vol. **408**, no. 6815, pp. 946–948, 2000.

[7] A. Dubinin, B. Winkler, K. Knorr, and V. Milman, "Lattice dynamics and elastic properties of PbF and BaF from quantum mechanical calculations," *The European Physical Journal B-Condensed Matter and Complex Systems*, vol. **39**, no. 1, pp. 27–33, (2004).

[8] S. Wang and H. Ye, "Ab initio elastic constants of C, Si, Ge," *Journal of Physics: Condensed Matter*, vol. **15**, pp. 5307–5314, (2003).

[9] X. Yang, A. Hao, X. Wang, X. Liu, and Y. Zhu, "First-principles study of structural stabilities, electronic and elastic properties of $BaF_2$ under high

pressure," *Computational Materials Science*, vol. **49**, no. 3, pp. 530–534, (2010).

[10] P. Ravindran, L. Fast, A. Korzhavyi, and B. Johansson, "Density functional theory for calculation of elasic properties of orthorhombic crystals: Application to $TiSi_2$," *Journal of Applied Physics*, vol. **84**, no. 9, pp. 4891–4904, (1998).

[11] H. Jiang, R. Pandey, C. Darrigan, and M. Rerat, "First-principles study of structural, electronic and optical properties of $BaF_2$ in its cubic, orthorhombic and hexagonal phases," *Journal of Physics: Condensed Matter*, vol. **15**, p. 709, (2003).

[12] A. Ivanov-Shitz, A. Buchstab, S. Aityan, and H. Kohler, "Molecular dynamics simulation of the superionic conductor $BaF_2$," *Applied Physics A: Materials Science & Processing*, vol. **54**, no. 3, pp. 251–257, (1992).

[13] A. Wright and B. Fender, "The structure of superionic compounds by powder neutron diffraction. I. Cation distribution in $\alpha$-AgI," *Journal of Physics C: Solid State Physics*, vol. **10**, no. 13, p. 2261, 2001.

[14] R. Wilsey, "XXXI. The crystal structure of the silver halides," *The London, Edinburgh, and Dublin Philosophical Magazine and Journal of Science*, vol. **42**, no. 248, pp. 262–263, 1921.

[15] P. Knauth and H. Tuller, "Solid-State Ionics: Roots, Status, and Future Prospects," *Journal of the American Ceramic Society*, vol. **85**, no. 7, pp. 1654–1680, 2002.

[16] J. Bazan and E. Dayen, "EMF Measurements in the Cell Ag/AgI/I2 (g), C and the Hole Conductivity of AgI," *Zeitschrift für Physikalische Chemie*, vol. **105**, no. 12, pp. 63–74, 1977.

[17] C. Derrington, A. Lindner, and M. O'Keeffe, "Ionic conductivity of some alkaline earth halides," *Journal of Solid State Chemistry*, vol. **15**, no. 2, pp. 171–174, 1975.

[18] R. Bonne and J. Schoonman, "The Ionic Conductivity of Beta Lead Fluoride," *Journal of The Electrochemical Society*, vol. **124**, no. 1, pp. 28–35, 1977.

[19] A. Chadwick, "High-temperature transport in fluorites," *Solid State Ionics*, vol. **8**, no. 3, pp. 209–220, 1983.

[20] K. Koto, H. Schulz, and R. Huggins, "Anion disorder and ionic motion in lead fluoride ($\beta$-$PbF_2$)," *Solid State Ionics*, vol. **1**, no. 5, pp. 355–365, 1980.

[21] J. Goff, W. Hayes, S. Hull, and M. Hutchings, "Neutron powder diffusion study of the fast-ion transition and specific heat anomaly in beta-lead fluoride," *Journal of Physics: Condensed Matter*, vol. **3**, no. 21, p. 3677, 1999.

[22] A. Walker, M. Dixon, and M. Gillan, "Computer simulation of ionic disorder in high-temperature $PbF_2$," *Journal of Physics C: Solid State Physics*, vol. **15**, no. 19, p. 4061, 2000.

[23] W. Hayes, "Superionic conductors," *Contemporary Physics*, vol. **19**, no. 5, pp. 469–486, 1978.

[24] M. Aniya, "Superionicity as a local fluctuation of the chemical bond," *Solid state ionics*, vol. **70**, pp. 673–677, 1994.

[25] S. Hull, "Superionics: Crystal structures and conduction processes," *Reports on Progress in Physics*, vol. **67**, pp. 1233–1314, (2004).

[26] G. Rubloff, "Far-ultraviolet reflectance spectra and the electronic structure of ionic crystals," *Physical review B*, vol. **5**, no. 2, p. 662, 1972.

[27] J. Frandon, B. Lahaye, and F. Pradal, "Spectra of Electronic Excitations in $CaF_2$, $SrF_2$, and $BaF_2$ in the 8 to 150 eV Range," *physica status solidi (b)*, vol. **53**, no. 2, pp. 565–575, 1972.

[28] M. Scrocco, "Satellites in x-ray photoelectron spectroscopy of insulators. I. Multielectron excitations in $CaF_2$, $SrF_2$, and $BaF_2$," *Physical Review B*, vol. **32**, pp. 1301–1305, 1985.

[29] R. Poole, J. Nicholson, J. Liesegang, J. Jenkin, and R. Leckey, "Electronic structure of $ZnF_2$, $CdF_2$, and $HgF_2$ studied by ultraviolet photoelectron spectroscopy," *Physical Review B*, vol. **20**, no. 4, p. 1733, 1979.

[30] K. Schmalzl, "Volume and pressure dependence of ground-state and lattice-dynamical properties of $BaF_2$ from density-functional methods," *Physical Review B*, vol. **75**, no. 1, p. 14306, (2007).

[31] R. Jia, H. Shi, and G. Borstel, "The atomic and electronic structure of $CaF_2$ and $BaF_2$ crystals with H centers: a hybrid DFT calculation study," *Journal of Physics: Condensed Matter*, vol. **22**, p. 055501, (2010).

[32] H. Shi, R. Jia, and R. Eglitis, "First-principles simulations on the aggregation of *F* centers in $BaF_2$: R centers," *Solid State Ionics*, vol. **1**, (2011).

[33] X. Yang, A. Hao, X. Wang, X. Liu, and Y. Zhu, "First-principles study of structural stabilities, electronic and elastic properties of $BaF_2$ under high pressure," *Computational Materials Science*, vol. **49**, pp. 530–534, (2010).

[34] M. Dickens, W. Hayes, M. Hutchings, and C. Smith, "Investigation of anion disorder in $PbF_2$ at high temperatures by neutron diffraction," *Journal of Physics C: Solid State Physics*, vol. **15**, p. 4043, (1982).

[35] M. Gillan, "The simulation of superionic materials," *Physica*, vol. **131B**, pp. 157–174, (1985).

[36] J. Leger, J. Haines, A. Atouf, O. Schulte, and S. Hull, "High-pressure x-ray-and neutron-diffraction studies of $BaF_2$: An example of a coordination number of II in $AX_2$ compounds," *Physical Review B*, vol. **52**, no. 18, pp. 13247–13256, (1995).

[37] W. Bollmann, "Ionic conductivity of $BaF_2$ crystals," *Crystal Res. Technol*, vol. **16**, no. 1039, p. 4014, (1981).

[38] C. Catlow and A. Stoneham, "Ionicity in solids," *Journal of Physics C: Solid State Physics*, vol. **16**, p. 4321, (1983).

[39] J. Boyce and B. Huberman, "Superionic conductors: Transitions, structures, dynamics," *Physics Reports*, vol. **51**, no. 4, pp. 189–265, (1979).

[40] Z. Gadjourova, Y. Marero, K. Andersen, Y. Andreev, and B. P.G., "Structures of the Polymer Electrolyte Complexes PEO6: LiXF6 (X= P, Sb), Determined from Neutron Powder Diffraction Data," *Chem. Mater*, vol. **13**, no. 4, pp. 1282–1285, (2001).

[41] C. Derrington, A. Lindner, and M. O'keeffe, "Ionic conductivity of some alkaline earth halides," *Journal of Solid State Chemistry*, vol. **15**, no. 2, pp. 171–174, (1975).

[42] V. Carr, A. Chadwick, and R. Saghafian, "The electrical conductivity of $PbF_2$ and $SrCl_2$ crystals at high temperatures," *Journal of Physics C: Solid State Physics*, vol. **11**, pp. L637–L641, (1978).

[43] A. Azimi, V. Carr, A. Chadwick, F. Kirkwood, and R. Saghafian, "Point defect parameters for [beta]-$PbF_2$ from a computer analysis of measurements of ionic conductivity," *Journal of Physics and Chemistry of Solids*, vol. **45**, no. 1, pp. 23–31, (1984).

[44] R. Martin, "Electronic structure: basic theory and practical methods," pp. 130–140, (Cambridge University Press), (2004).

[45] D. Hartree, "The calculation of Atomic Structures," vol. **1**, pp. (18–30), New York Wiley and Sons, (1957).

[46] P. Hohenberg and W. Kohn, "Inhomogeneous Electron Gas," *Physical Review*, vol. **136**, pp. 864–871, (1964).

[47] D. K. G. V. John, F. and P. D. Mukunda, *Electronic Density Functional Theory; Recent Progress and New Directions*. Plenum Press, (1996).

[48] D. Joubert, "Density Functionals: Theory and Applications," pp. 101–120, (Springer Verlag), (1998).

[49] P. R.G. and Y. W., "Density-functional theory of the electronic structure of molecules," *Annual Review of Physical Chemistry*, vol. **46**, no. 1, pp. 701–728, (1995).

[50] L. Site, "Levy–Lieb constrained-search formulation as a minimization of the correlation functional," *Journal of Physics A: Mathematical and Theoretical*, vol. **40**, p. 2787, (2007).

[51] M. Levy, "*Universal variational functionals of electron densities, first-order density matrices, and natural spin-orbitals and solution of the v-representability problem*," *Proceedings of the National Academy of Sciences*, vol. **76**, no. 12, p. 6062, (1979).

[52] E. Lieb, "*Physics as Natural Philosophy: Essays in honor of Lazslo Tisza on his 75th Birthday*," p. 111, (1982).

[53] W. Kohn, L. Sham, *et al.*, "Self-consistent equations including exchange and correlation effects," *Phys. Rev*, vol. **140**, no. 4A, pp. A1133–A1138, (1965).

[54] R. Parr and W. Yang, "Density-functional theory of atoms and molecules," ch. **16**, pp. 201–202.

[55] W. Koch, M. Holthausen, and M. Holthausen, "A chemist's guide to density functional theory," vol. **2**, Wiley Online Library, (2001).

[56] P. Dirac, "Note on exchange phenomena in the Thomas atom," in *Mathematical Proceedings of the Cambridge Philosophical Society*, pp. 376–385, Cambridge University Press, (1930).

[57] D. Ceperley and B. Alder, "Ground state of the electron gas by a stochastic method," *Physical Review Letters*, vol. **45**, no. 7, pp. 566–569, (1980).

[58] F. Hamprecht, A. Cohen, D. Tozer, and N. Handy, "Development and assessment of new exchange-correlation functionals," *The Journal of chemical physics*, vol. **109**, p. 6264, (1998).

[59] M. Payne, M. Teter, D. Allan, T. Arias, and J. Joannopoulos, "Iterative minimization techniques for *ab initio* total-energy calculations: molecular dynamics and conjugate gradients," *Reviews of Modern Physics*, vol. **64**, no. 4, pp. 1045–1097, (1992).

[60] Paolo Giannozzi, et al, "Quantum espresso: a modular and open-source software project for quantum simulations of materials," *Journal of Physics: Condensed Matter*, vol. **21**, no. 39, p. 395502 (19pp), (2009).

[61] J. Perdew, "Density-functional approximation for the correlation energy of the inhomogeneous electron gas," *Physical Review B*, vol. **33**, no. 12, p. 8822, (1986).

[62] J. Perdew, "Density-functional approximation for the correlation energy of the inhomogeneous electron gas," *Physical Review B*, vol. **33**, no. 12, p. 8800, (1986).

[63] S. Kurth, J. Perdew, and P. Blaha, "Molecular and solid-state tests of density functional approximations: LSD, GGAs, and meta-GGAs," *International journal of quantum chemistry*, vol. **75**, no. 4-5, pp. 889–909, (1999).

[64] J. Perdew and Y. Wang, "Pair-distribution function and its coupling-constant average for the spin-polarized electron gas," *Physical Review B*, vol. **46**, no. 20, p. 12947, (1992).

[65] J. Perdew, K. Burke, and Y. Wang, "Generalized gradient approximation for the exchange-correlation hole of a many-electron system," *Physical Review B*, vol. **54**, no. 23, p. 16533, (1996).

[66] M. Molepo, "Computational study of the structural phase transitions and pressure dependent electronic structure of ZnO," in *PhD Thesis*, p. 51, (University of the Witwatersrand), (2012).

[67] J. Perdew, P. Ziesche, and H. Eschrig, "Electronic structure of solidsâĂŹ 91," *Akademie-Verlag, Berlin*, pp. 11–20, (1991).

[68] N. Ashcroft and N. Mermin, *Solid State Physics* . Springer, New York, 1976.

[69] H. Monkhorst, "Hartree-Fock density of states for extended systems," *Physical Review B*, vol. **20**, no. 77, pp. 1504–1513, (1976).

[70] S. Baroni, P. Giannozzi, and A. Testa, "Elastic constants of crystals from linear-response theory," *Physical review letters*, vol. **59**, no. 23, pp. 2662–2665, (1987).

[71] S. Baroni, S. de Gironcoli, A. Dal Corso, and P. Giannozzi, "Phonons and related crystal properties from density-functional perturbation theory," *Reviews of Modern Physics*, vol. **73**, no. 2, pp. 515–540, (2001).

[72] R. Feynman, "Forces in Molecules," *Physical Review*, vol. **56**, pp. 340–343, (1939).

[73] J. Harris and R. Jones, "Pseudopotentials in density-functional theory," *Physical Review Letters*, vol. **41**, no. 3, pp. 191–194, (1978).

[74] J. Phillips and Kleinman, "New Method for Calculating Wave Functions in Crystals and Molecules," *Physical Review*, vol. **116**, pp. 287–294, (1959).

[75] G. Bachelet, D. Hamann, and S. M., "Pseudopotentials that work: From H to Pu," *Physical Review B*, vol. **26**, no. 8, p. 4199, (1982).

[76] S. Louie, S. Froyen, and M. Cohen, "Nonlinear ionic pseudopotentials in spin-density-functional calculations," *Physical Review B*, vol. **26**, no. 4, pp. 1738–1742, (1982).

[77] D. Vanderbilt, "Soft self-consistent pseudopotentials in a generalized eigenvalue formalism," *Physical Review B*, vol. **41**, no. 11, p. 7892, (1990).

[78] P. Blöchl, "Generalized separable potentials for electronic structure calculations," *Physical Review B*, vol. **41**, p. 5414, (1990).

[79] H. Krakauer, M. Posternak, and A. Freeman, "Linearized augmented plane-wave method for the electronic band structure of thin films,"

[80] R. Pick, M. Cohen, and R. Martin, "Microscopic theory of force constants in the adiabatic approximation," *Physical Review B*, vol. **1**, no. 2, p. 910, (1970).

[81] A. Chadwick, "High-temperature transport in fluorites," *Solid State Ionics*, vol. **8**, no. 3, pp. 209–220, (1983).

[82] S. Limpijumnong and C. Van de Walle, "Diffusivity of native defects in GaN," *Physical Review B*, vol. **69**, no. 3, p. 035207, (2004).

[83] H. Rosenberg, "The Solid State," vol. **3**, pp. 36–41, Oxford science publications, (1990).

[84] G. Makov and M. Payne, "Periodic boundary conditions in ab initio calculations," *Physical Review B*, vol. **51**, no. 7, p. 4014, (1995).

[85] M. Leslie and N. Gillan, "The energy and elastic dipole tensor of defects in ionic crystals calculated by the supercell method," *Journal of Physics C: Solid State Physics*, vol. **18**, p. 973, (1985).

[86] P. Ewald, "Principles of the Theory of Solids," *Cambridge University Press*, vol. **64**, p. 253, (1964).

[87] M. Gaio and L. Pier, "Efficient calculation of Madelung constants for cubic crystals," *Physical Review B*, vol. **79**, p. 012102, (2009).

[88] F. Ercolessi, "A molecular dynamics primer," *Spring College in Computational Physics, ICTP, Trieste*, pp. 24–25, (1997).

[89] D. Rapaport, "The art of molecular dynamics simulation," pp. 134–140, Cambridge University Press, 1995.

[90] D. Frenkel and B. Smit, "Understanding molecular simulation; From Algorithms to Applications," pp. 40–60, Academic Press, (2002).

[91] S. Nose, "A unified formulation of the constant temperature molecular dynamics method," *J. Chem. Phys.*, vol. **81**, pp. 511–519, (1984).

[92] S. Nose, "A molecular dynamics method for simulation in the canonical ensemble," *Mol. Phys.*, vol. **52**, pp. 255–268, (1984).

[93] S. B. Frenkel, D., "Understanding molecular simulation; From Algorithms to Applications," pp. 147–153, Academic Press, (2002).

[94] M. Xavier, "Mean Square displacement analysis of single-particle trajectories with localization error: Brownian motion in an isotropic medium," *Physical Review E*, vol. **82**, p. 041914, (2010).

[95] M. Ribeiro and L. Almeid, "Validating a polarizable model for the glass-forming liquid CaK (NO) by ab initio calculations," *The Journal of Chemical Physics*, vol. **113**, p. 4722, (2000).

[96] E. Demiralp, T. Çağin, and W. Goddard III, "Morse stretch potential charge equilibrium force field for ceramics: Application to the quartz-stishovite phase transition and to silica glass," *Physical review letters*, vol. **82**, no. 8, pp. 1708–1711, (1999).

[97] J. Tersoff *et al.*, "Modeling solid-state chemistry: Interatomic potentials for multicomponent systems," *Physical Review B*, vol. **39**, no. 8, pp. 5566–5568, (1989).

[98] A. Rowley, P. Jemmer, M. Wilson, and P. Madden, "Evaluation of the many-body contributions to the interionic interactions in MgO," *The Journal of chemical physics*, vol. **108**, p. 10209, (1998).

[99] P. Tangney and S. Scandolo, "An ab initio parametrized interatomic force field for silica," *The Journal of Chemical Physics*, vol. **117**, p. 8898, (2002).

[100] D. Tom, Y. Darrin, and P. Lee, "Particle mesh Ewald: N-log(N) method for Ewald Sum in large systems," *Journal of Chemical Physics*, vol. **98**, p. 10089, (1993).

[101] J. Perdew and A. Zunger, "Self-interaction correction to density-functional approximations for many-electron systems," *Physical Review B*, vol. **23**, no. 10, p. 5048, (1981).

[102] J. Perdew, K. Burke, and M. Ernzerhof, "Generalized gradient approximation made simple," *Physical Review Letters*, vol. **77**, no. 18, pp. 3865–3868, (1996).

[103] Y. Wu, W. Hu, and S. Han, "First-principles calculation of the elastic constants, the electronic density of states and the ductility mechanism of the intermetallic compounds: YAg, YCu and YRh," *Physica B: Physics of Condensed Matter*, vol. **403**, no. 19-20, pp. 3792–3797, (2008).

[104] P. Ravindran, P. Vajeeston, R. Vidya, A. Kjekshus, and H. Fjellvåg, "Detailed electronic structure studies on superconducting $MgB_2$ and related compounds," *Physical Review B*, vol. **64**, no. 22, p. 224509, (2001).

[105] A. Zaoui, M. Ferhat, M. Certier, H. Aourag, and B. Khelifa, "Calculation of the elastic properties of CuCl," *Physics Letters A*, vol. **228**, no. 6, pp. 378–382, (1997).

[106] R. Martin, "Relation between elastic tensors of wurtzite and zinc-blende structure materials," *Physical Review B*, vol. **6**, no. 12, pp. 4546–4553, (1972).

[107] I. Ipatova, M. Lifchits, and A. Mastov, "Anisotropy for hexagonal phase," *11th International Symposium: Nanostructures Physics and Technology*, pp. 1–5, (2003).

[108] F. Birch, "Finite elastic strain of cubic crystals," *Physical Review*, vol. **71**, no. 11, p. 809, (1947).

[109] K. Li, H. Xiao, and L. Wang, "Computer simulation study of defect formation and migration energy in calcium fluoride," *Nuclear Instruments and Methods in Physics Research Section B: Beam Interactions with Materials and Atoms*, vol. **266**, no. 12-13, pp. 2698–2701, (2008).

[110] K. Sato, T. Yoshiie, T. Ishizaki, and Q. Xu, "Behavior of vacancies near edge dislocations in Ni and $\alpha$-Fe: Positron annihilation experiments and rate theory calculations," *Physical Review B*, vol. **75**, no. 9, p. 094109, (2007).

[111] F. Ercolessi and J. Adams, "Interatomic potentials from first-principles calculations: the force-matching method," *EPL (Europhysics Letters)*, vol. **26**, p. 583, (1994).

[112] H. Xiao and J. Jamil, "Local density and generalized gradient approximations," *Journal of Physics Letters*, vol. **23**, pp. 212–217, (2011).

[113] X. Gonze and C. Lee, "Dynamical matrices, Born effective charges, dielectric permittivity tensors, and interatomic force constants from density-functional perturbation theory," *Physical Review B*, vol. **55**, no. 16, p. 10355, (1997).

[114] G. Horton and A. Maradudin, "Dynamical properties of solids," *Physcal Review*, vol. **1**, p. 129, (1974).

[115] G. F. Ching, W.Y and M. Huang, "Electronic and optical properties of pure Ce3+-doped MgS single crystals: A first-principles prediction," *Physical Review*, vol. **52**, no. 222, p. 809, (1995).

[116] R. Dovesi, R. Orlando, B. Civalleri, C. Roetti, V. Saunders, and C. Zicovich-Wilson, "CRYSTAL: a computational tool for the ab initio study of the electronic properties of crystals," *Zeitschrift für Kristallographie*, vol. **220**, no. 5/6/2005, pp. 571–573, 2005.

[117] V. Katsika-Tsigourakou and E. Skordas, "Defect entropies and enthalpies in $BaF_2$," *Central European Journal of Physics*, vol. **8**, no. 6, pp. 900–904, (2010).

[118] Chemexper, "Catalog of chemical supplies." `http://www.chemexper.com/chemicals/supplier/cas/7787-32-8.html`. Accessed July, 2012.

[119] P. Ngoepe and J. Comins, "Measurements of elastic constants in super-ionic $Ba_{1-x}La_xF_{2+x}$," *Journal of Physics C: Solid State Physics*, vol. **19**, p. L267, (1986).

[120] H. Shi, W. Luo, B. Johansson, and R. Ahujia, "Electronic and elastic properties of $CaF_2$ under high pressure from ab initio calculations," *Journal of Physics: Condensed Matter*, vol. **21**, p. 415501, (2009).

[121] B. Mayer, H. Anton, E. Bott, M. Methfessel, J. Sticht, J. Harris, and P. Schmidt, "Ab-initio calculation of the elastic constants and thermal expansion coefficients of Laves phases," *Intermetallics*, vol. **11**, no. 1, pp. 23–32, (2003).

[122] Y. Ciftci, K. Çolakoglu, E. Deligoz, and H. Ozisik, "The first-principles study on the LaN," *Materials Chemistry and Physics*, vol. **108**, no. 1, pp. 120–123, 2008.

[123] I. Almaz Optics, "Barium fluoride." `http://www.almazoptics.com/html`. Accessed Aug., 2012.

[124] F. Murnaghan, "Finite deformations of an elastic solid," *American Journal of Mathematics*, vol. **59**, no. 2, pp. 235–260, (1937).

[125] C. Van de Walle and J. Neugebauer, "First-principles calculations for defects and impurities: Applications to III-nitrides," *Journal of applied physics*, vol. **95**, p. 3851, (2004).

[126] T. F. W. Smith and I. Todorov, "The dl-poly-2 user manual." `http://www.ccp5.ac.uk/uk`. Accessed Aug., 2012.

# APPENDIX A

## MECHANICAL PROPERTIES

The cubic phase is the most stable among the three phases of $BaF_2$. Its mechanical properties are therefore crucial. Elastic constants play an important role in the understanding of mechanical properties of materials. For the application in engineering, some of the properties like Young's modulus $E$ and Poisson's ratio $\gamma$ should be known. Young's modulus $E$ is the ratio between stress and strain and gives information on stiffness of material.

Larger value of $E$ shows that the material is more stiff. Poisson's ratio $\alpha$ indicates the bonding characteristic of a material. Poisson's ratio $\gamma$ of between 0.25 and 0.5, are the lower and upper limits of the central forces in solids, respectively [121, 33]. Poisson's ratio is given as;

$$\gamma = \frac{1}{2}\left[\frac{B-(2/3)G}{B+(1/3)G}\right], \tag{A.0.1}$$

where $G$ is the isotropic shear modulus in the form

$$G = \frac{(G_V + G_R)}{2}. \tag{A.0.2}$$

$G_V$ and $G_R$ are Voigt's and Reuss's shear modulus, respectively, given as [122],

$$G_V = \frac{C_{11} - C_{12} + 3C_{44}}{5} \tag{A.0.3}$$

and

$$\frac{5}{G_R} = \frac{4}{C_{11} - C_{12}} + \frac{3}{C_{44}}. \tag{A.0.4}$$

In the present work the Poisson's ratio was found to be 0.32 comparable to that on data base of 0.34 [123]. It can therefore be concluded that the interatomic forces of $BaF_2$ are central forces. This is in contrast to a value of 0.24, reported by X.Yang

et al [33]. In the same work of Ref.[33], it has also been shown that Young's modulus $E$ increases with increase in pressure, suggesting that the stiffness also increase with pressure.

For the orthorhombic phase, the bulk modulus was found to be 109 GPa and the isotropic shear modulus was 102.73 GPa, giving a Poisson's ratio of 0.141. This is an indication that the forces acting on orthorhombic phase of $BaF_2$ are less of the central forces in nature when compared to cubic phase. This also points at reduced stability of this phase.

In hexagonal phase, the bulk modulus derived from Murnaghan equation of state was 154 GPa while the Poisson's ratio was 0.42. It is again seen that the hexagonal phase just like the orthorhombic phase has internal forces that are not central. This indicates that these two phases were not stable compared to the cubic phase.

**Equation of State, EOS**

Equation of state provides information about the thermodynamic parameters of the crystal. The derivative of bulk modulus with pressure is given as;

$$B' = \left(\frac{\partial B}{\partial P}\right)_T, \tag{A.0.5}$$

and this changes little with pressure. At zero pressure, $B' = B'_0$ is a constant and therefore

$$B(P) = B_0 + B'_0 P \tag{A.0.6}$$

where $B_0$ is the bulk modulus at zero pressure. Equating to eqn.(4.35), and rearranging one obtains

$$\frac{dV}{V} = -\frac{dP}{B_0 + B'_0 P}. \tag{A.0.7}$$

On integrating, we obtain the Murnaghan [124] equation of state for pressure

$$P(V) = \frac{B_0}{B_0'}\left(\left(\frac{V_0}{V}\right)^{B_0'} - 1\right) \tag{A.0.8}$$

or equivalently, for volume

$$V(P) = V_0\left(1 + B_0'\frac{P}{B_0}\right)^{-1/B_0'}. \tag{A.0.9}$$

We then substitute eqn.(A.0.8) into $E = E_0 - \int PdV$ which results in the Murnaghan equation of state for energy

$$E(V) = E_0 + \frac{B_0 V}{B_0'}\left(\frac{(V_0/V)^{B_0'}}{B_0' - 1} + 1\right) - \frac{B_0 V_0}{B_0' - 1}. \tag{A.0.10}$$

Murnaghan equation is more accurate only when pressure tends to zero [66] as it is shown in the linearized bulk modulus-pressure relation of eqn.(A.0.6).

The calculation of bulk modulus in this work was done by using Birch-Murnaghan isothermal EOS [108]. This is given as;

$$P = \frac{3}{2}B_0\left[\left(\frac{V_0}{V}\right)^{\frac{7}{3}} - \left(\frac{V_0}{V}\right)^{\frac{5}{3}}\right]\left\{1 + \frac{3}{4}(B_0' - 4)\left[\left(\frac{V_0}{V}\right)^{\frac{2}{3}} - 1\right]\right\}. \tag{A.0.11}$$

Also, $E(V)$ is found by integrating the pressure;

$$E(V) = E_0 + \frac{9V_0B_0}{16}\left\{\left[\left(\frac{V_0}{V}\right)^{\frac{2}{3}} - 1\right]^3 B_0' + \left[\left(\frac{V_0}{V}\right)^{\frac{2}{3}} - 1\right]^2\left[6 - 4\left(\frac{V_0}{V}\right)^{\frac{2}{3}}\right]\right\}. \tag{A.0.12}$$

Using this relation, the equilibrium bulk properties $V_0$, $B_0$, and $B_0'$ as well as the total energy at equilibrium were calculated using GGA functionals by fitting the total energy as a function of unit cell volume data into the third-order-Murnaghan EOS eqn.(A.0.12). The values used are calculated around the equilibrium point at about 5% from equilibrium lattice point. The values from this approach are compared from the bulk modulus obtained from the derivation of elastic constants.

The structural properties of $BaF_2$ in the three phases are also studied by looking into the Young's modulus, strain and bulk modulus.

### Density of States and Band Structure

The density of states and band gap are given here separately. The size of the band gap for c-$BaF_2$ was 7.2 eV and 6.9 eV for the orthorhombic phase. The band gap for hexagonal phase was 6.47 eV. Though the decrease is small, we observe a general decrease in the band gap as the phase changes from cubic to orthorhombic to hexagonal phases. The density of states for the cubic, orthorhombic and hexagonal phases are shown in figures A-A. These figures clearly show that the width of the band gap is decreasing.

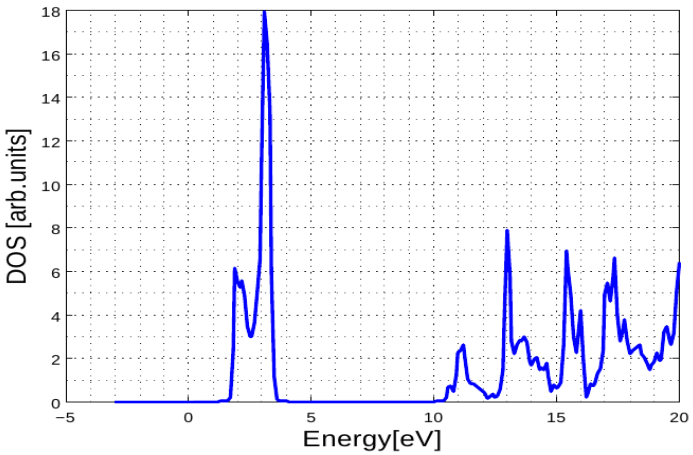


**Figure A.1: Density of states of the cubic phase of $BaF_2$.**

The band structures are presented in figures A-A. Band distribution is clearly seen in the cubic phase but the distribution becomes sparse as one goes from cubic to orthorhombic to hexagonal phases. Jiang et al [11] report no closing of the energy gap up to 50 GPa in their study of pressure variation with phase transition in $BaF_2$.

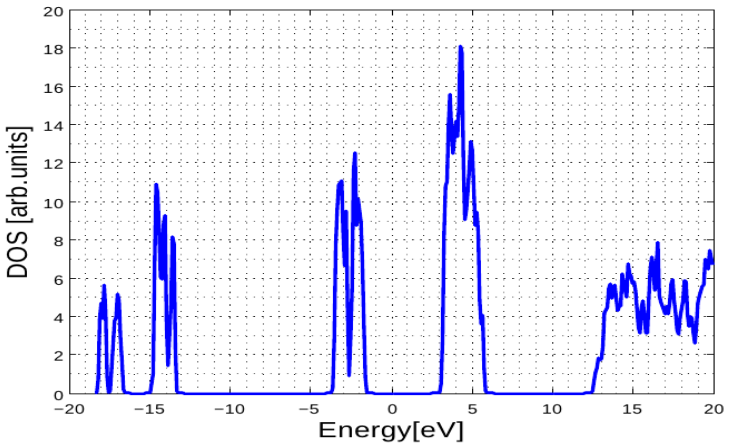


**Figure A.2: Density of states of the orthorhombic phase of $BaF_2$.**

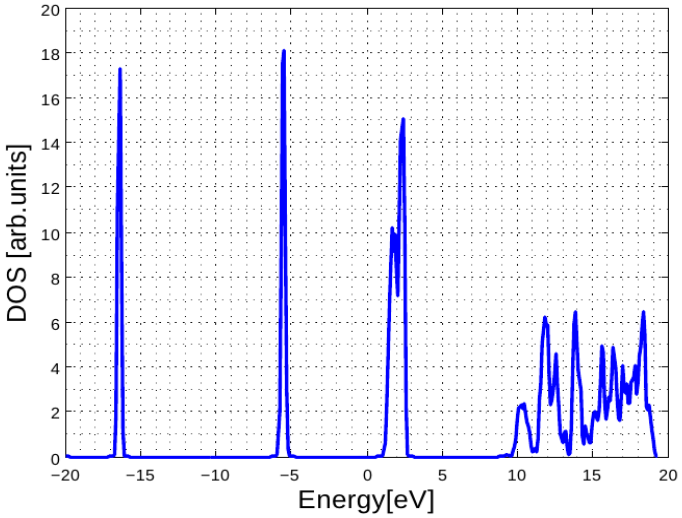


**Figure A.3: Density of states of the hexagonal phase of $BaF_2$.**

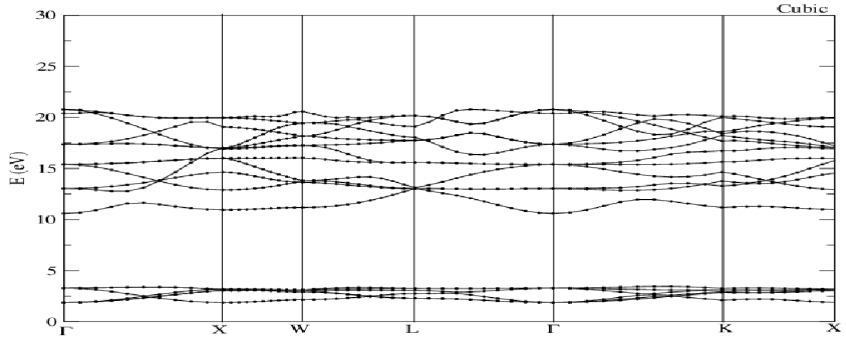


**Figure A.4: Band structures of the cubic phase of $BaF_2$.**

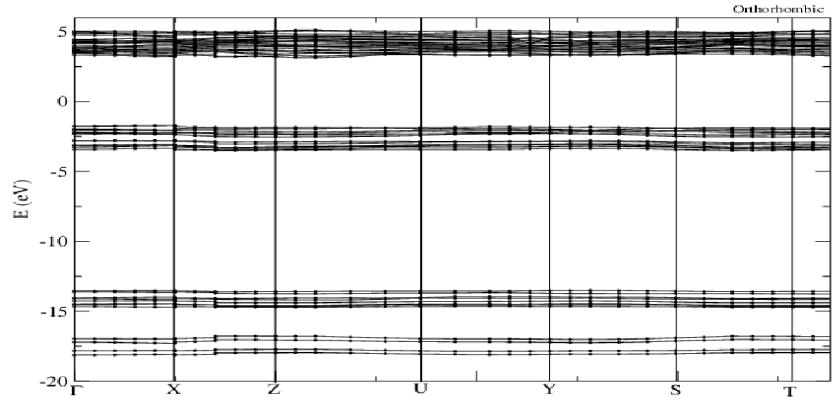


**Figure A.5: Band structures of the orthorhombic phase of $BaF_2$.**

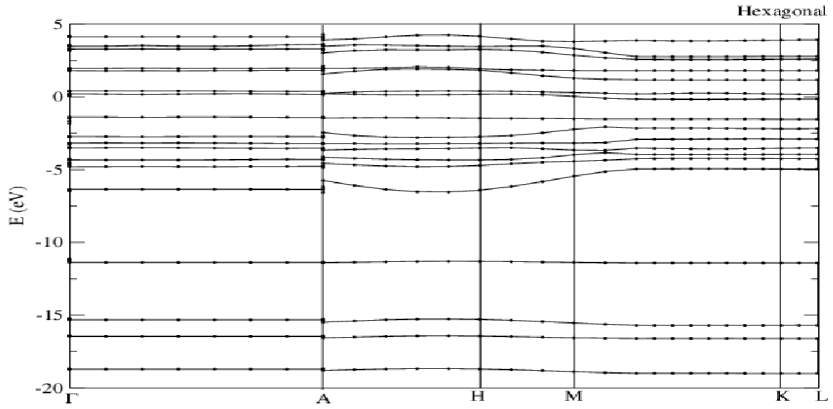


**Figure A.6: Band structures of the hexagonal phase of $BaF_2$.**

**Defects**

In the calculation of formation energy of a defect or impurity, the relation of Van de Walle and J. Neugebauer [125], was used and it reduced to eqn.(A.0.13). The calculated value for the neutral vacancy was found to be 15.64 eV and the Table A was derived from eqn.(A.0.13). Figures 5.5.1 to 5.5.1 of chapter 5 section 5.5 were all derived using similar formulation. Table A and A, are the charged cation vacancy and charged cation interstitials, respectively, used as examples to show how the charged system is treated to take care of the aperiodic crystal.

$$\Delta E = 21.27 + 0.45 - q(E_V + E_F). \tag{A.0.13}$$

**Table A.1: Variation of Fermi level against energy change for charged anion vacancy of $BaF_2$ at ground state conditions.**

| $E_F$ | $\Delta E$ |
|---|---|
| 0 | 15.2 |
| 2 | 11.2 |
| 4 | 7.2 |
| 6 | 3.2 |
| 8 | -0.8 |
| 10 | -4.8 |

The value for neutral cation was calculated at 3.14 eV. In the case of charged interstitial, the relation given below was used

$$-18.3 + 6.8 + 2E_F. \tag{A.0.14}$$

Using relation of eqn.(A.0.14), Table A was generated.

**Table A.2: Variation of Fermi energy against change in energy for charged cation interstitial of $BaF_2$ at ground state conditions.**

| $E_F$ | $\Delta E$ |
|---|---|
| 0 | -11.5 |
| 2 | -7.5 |
| 4 | -3.5 |
| 6 | 0.5 |
| 8 | 4.5 |
| 10 | 8.5 |

# APPENDIX B

## VALENCE AND FERMI ENERGIES FOR INTERSTITIAL $BA^{+2}$

End of self-consistent calculation

k = 0.2500 0.2500 0.2500 ( 73326 PWs) bands (ev):

-22.5805 -20.1345 -20.1345 -20.1345 -20.0718 -20.0327 -20.0327 -18.7560 -18.7212 -18.7212 -18.7094 -18.6994 -18.6994 -18.6892 -18.6829 -18.5317 -18.5317 -18.5120 -18.5046 -18.5046 -18.4835 -18.4741 -18.4564 -18.4564 -18.4257 -18.4257 -18.3922 -18.2571 -18.1630 -18.1630 -18.1621 -18.1112 -18.1112 -17.4337 -17.4337 -17.4336 -17.4142 -17.4142 -17.4139 -17.3206 -17.2095 -15.5636 -15.5636 -15.5460 -15.5457 -15.5457 -15.5449 -15.5423 -15.5423 -15.5367 -15.5367 -15.5324 -15.5248 -15.4994 -15.4994 -15.4979 -15.4979 -15.4908 -15.4750 -15.4608 -15.4608 -15.4530 -15.4334 -15.4334 -15.4012 -15.0881 -15.0881 -15.0827 -15.0788 -15.0742 -15.0742 -15.0706 -15.0706 -15.0680 -15.0670 -15.0670 -15.0625 -15.0398 -15.0398 -15.0381 -15.0381 -15.0367 -15.0241 -14.9792 -14.9792 -14.9751 -14.9751 -14.9697 -14.9512 -14.8687 -14.8687 -14.8685 -14.8497 -14.8497 -14.8488 -14.7938 -14.7487 -8.3505 -8.3505 -8.3505 -5.7149 -5.7149 -5.4419 -5.4277 -5.4277 -5.4277 -5.2703 -5.2702 -5.2702 -5.2337 -5.2337 -5.2335 -5.1264 -5.1263 -5.1263 -4.6797 -4.6796 -4.6796 -4.0955 -4.0632 -4.0620 -4.0620 -4.0273 -4.0273 -4.0172 -4.0172 -4.0039 -3.9869 -3.9690 -3.9690 -3.9479 -3.9433 -3.9426 -3.9285 -3.9285 -3.9189 -3.9115 -3.9115 -3.9081 -3.9081 -3.8938 -3.8938 -3.8879 -3.8795 -3.8795 -3.8672 -3.8672 -3.8625 -3.7751 -3.7730 -3.7730 -3.7705 -3.7696 -3.7696 -3.7372 -3.7372 -3.7290 -3.7254 -3.7209 -3.7209 -3.6952 -3.6952 -3.6802 -3.6692 -3.6692 -3.6608 -3.6531 -3.6387 -3.6365 -3.6365 -3.6249 -3.6249 -3.6108 -3.6076 -3.6076 -3.5780 -3.5748 -3.5748 -3.5321 -3.5321 -3.5319 -3.3926 -3.3894 -3.3894 -3.3841 -3.3841 -3.3829 -3.3795 -3.3738 -3.3738 -3.3708 -3.3591 -3.3591 -3.2197 -3.2196 -3.2196 0.5578 0.5578 0.5592 0.9045 0.9045 0.9902 1.0415 1.0415 1.0415 1.1138 1.1138 1.1165 1.1502 1.1502 1.1503 1.2885 1.2885 1.2887 1.2939 1.2939 1.2952 1.5237 1.5240 1.5240 2.4567 2.4615 2.4615 2.4989 2.4989 2.5295 2.5343 2.5469 2.5469 2.5778 2.5778 2.5810 2.6132

2.6280 2.6280 2.6452 2.6528 2.6528 2.6774 2.6774 2.6795 2.6946 2.7008 2.7008
2.7509 2.7601 2.7601 2.7884 2.7884 2.7976 2.8149 2.8149 2.8176 2.8250 2.8308
2.8308 2.8409 2.8438 2.8438 2.8618 2.8754 2.8754 2.8863 2.8961 2.8961 2.9033
2.9033 2.9102 2.9544 2.9544 2.9699 2.9837 2.9947 2.9947 3.0091 3.0091 3.0263
3.0523 3.0626 3.0626 3.0702 3.1120 3.1120 3.1195 3.1195 3.1306 3.1379 3.1734
3.1734 3.1916 3.2019 3.2019 3.2208 3.2208 3.2210 3.2228 3.2228 3.2340 3.2513
3.2513 3.2697 3.2697 3.2906 3.2925 3.2925 3.3183 3.3198 3.3198 3.3239 3.3828
3.4117 3.4152 3.4152 3.4299 3.4299 3.4303 3.4508 3.4508 3.4857 3.5036 3.5036
3.5123 3.5315 3.5315 3.5325 3.5496 3.5496 3.5685 3.5698 3.5698 3.5704 3.5953
3.5953 3.6026 3.6144 3.6226 3.6242 3.6242 3.6323 3.6544 3.6544 3.6628 3.6709
3.6744 3.6744 3.6747 3.6872 3.6872 3.7216 3.7284 3.7326 3.7326 3.7427 3.7427
3.7647 3.7647 3.7819 3.7918 3.7918 3.8158 3.8158 3.8172 3.8281 3.8281 3.8547
3.8622 3.8694 3.8694 3.8916 3.8959 3.8959 3.9132 3.9132 3.9279 3.9279 3.9372
3.9417 3.9417 4.0023 4.0161 4.0166 4.0166 4.0691 4.0788 4.0788 4.0933 4.0933
4.0952 8.6534 8.6534 10.2348 10.2350 10.2350 10.8837 10.9307 10.9307 11.1409
11.1409 11.1696 11.1900 11.1900 11.1904 11.3499 11.7359 11.7359 11.8196 11.8196
11.8341 11.8450 11.9981 11.9981 11.9985 12.0461 12.0461 12.1082 12.1320 12.1320
12.1464 12.1625 12.1979 12.1979 12.4263 12.4263 12.4330 12.4775 12.4775 12.4946
12.5567 12.5567 12.7440 12.7767 12.8729 13.0008 13.0008 13.0540 13.1456 13.1637
13.1637 13.2118 13.2825 13.2825 13.3734 13.3734 13.4396 13.4396 13.4988 13.5083
13.5083 13.5126 13.5188 13.5188 13.5530 13.6000 13.6114 13.6114 13.6458 13.6458
13.6800 13.7125 13.7156 13.7156 13.7420 13.7420 13.7628 13.7889 13.7889

the Fermi energy is 4.8326 ev

# APPENDIX C

## POTENTIAL PARAMETRIZATION

In order to generate the force field, the potential of Buckingham [12] was used to do classical molecular dynamics. This first procedure was carried out to generate the random positions of the system. These initial conditions were fixed at 1200 K and zero pressure which is about the superionic temperature of $BaF_2$. This was done to ensure that the parameters generated were not correlated in terms of bond geometry and other deformation properties thus enabling the force field to be applicable in wide range of temperatures.

The initial molecular dynamics trajectories were performed using the DL_POLY code [126] and ten configurations were chosen which were far apart. This separation was chosen to minimize the correlation between configurations. *Ab initio* calculations were performed on these initial configurations to obtain total forces, stress and energies. Using the force matching approach, the classical forces were matched to the *ab initio* forces. This procedure was done to fit the classical forces as close as possible to the *ab initio* ones. If the minimum was not reached as desired, the procedure was repeated by using the force field generated to produce positions for the DFT calculations. The parameters from the DFT runs were then used in the force matching until the minimum was achieved. The general procedure is shown in the flowchart of Fig.C.

In this current work, a run was done to minimize the forces, stresses and energies up to reasonable minimum. For example, our calculation was stopped at final values of $\Delta F = 0.175$, $\Delta S = 0.176$ and $\Delta E = 0.122$ which were sufficiently minimum. $\Delta F$, $\Delta S$ and $\Delta E$ are the percentage errors of forces, stresses and energies, respectively. The weight of force, $w_f$, weight of stress, $w_s$ and weight of energy, $w_E$ were at 1.0%, 0.01% and 0.08%, respectively, at the instant when the runs were stopped. At these minimum values, the force matching process slows down and any increase in efficiency seems insignificant. We used 28 different

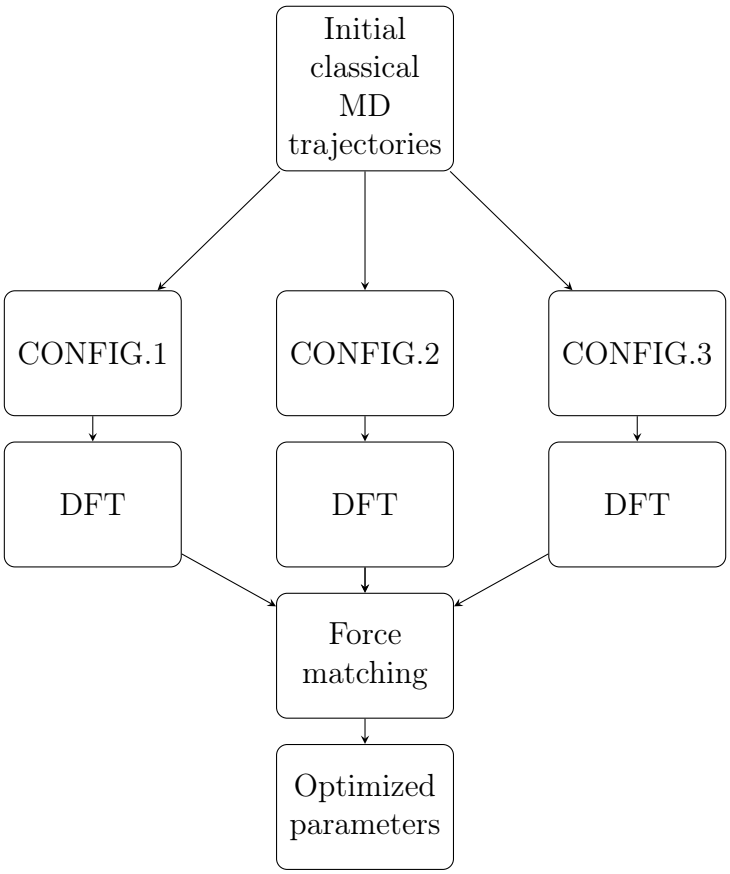


**Figure C.1: Force matching procedure.**

configurations in the minimization process. This new potential generated was then used to do molecular dynamics in order to study some selected thermodynamic properties of $BaF_2$. Detailed data showing various parameters is given on Table 5.6.1 of Chapter 5.6.1. In fig.C, it is shown that the forces distribution between the density functional theory are close to the parametrized ones. This is the main objective that, the error in the forces has to be as minimum as possible. The error in the two forces was about 17%, as mentioned earlier. A plot of temperature at 1350 K versus total number of steps is shown in fig C. The Nose thermostat method for thermal equilibration was used in all temperatures.

The equilibrium energy is found to be about -19.18 Ry and the equilibrium point was achieved after 20,000 steps or 29 ps which proved to be long enough.

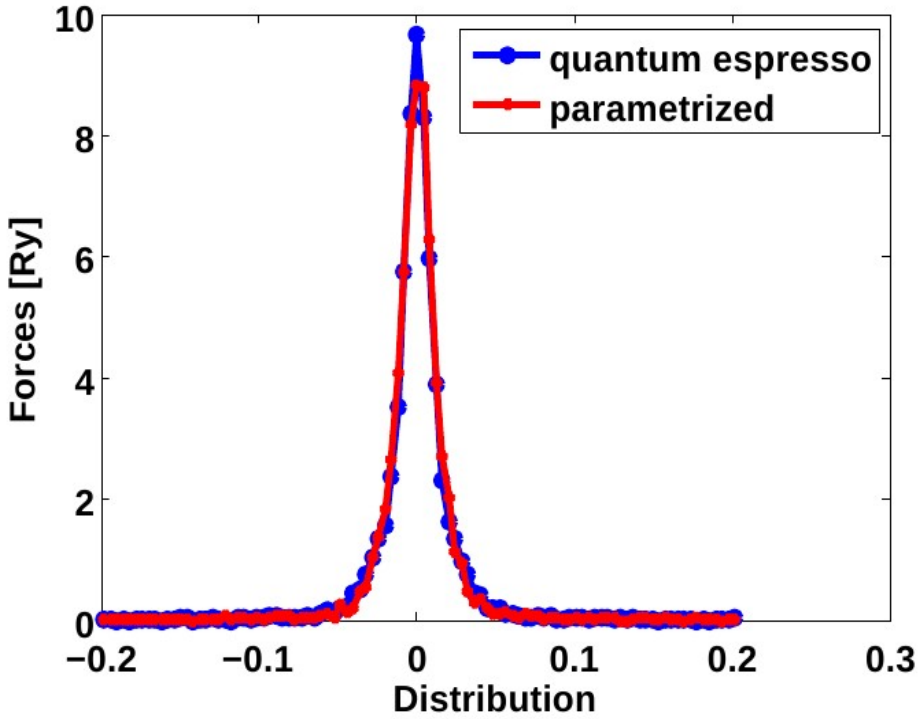


**Figure C.2: Comparison of the force distribution from density functional theory (blue in soft copy) to that minimized by the classical molecular dynamics of Asap Code (red). The two forces are very close indicating that the newly generated potential is close to the DFT forces.**

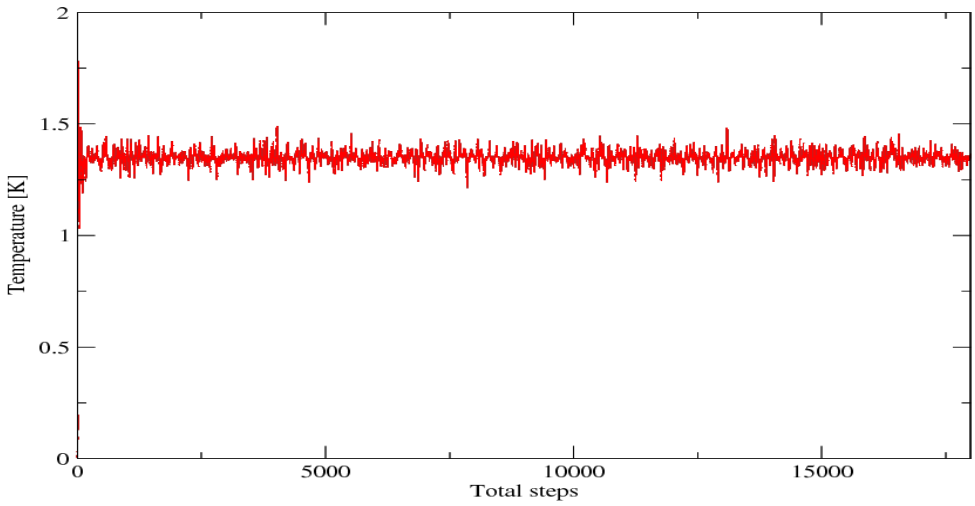


**Figure C.3: The temperature dependence of the total time steps.**

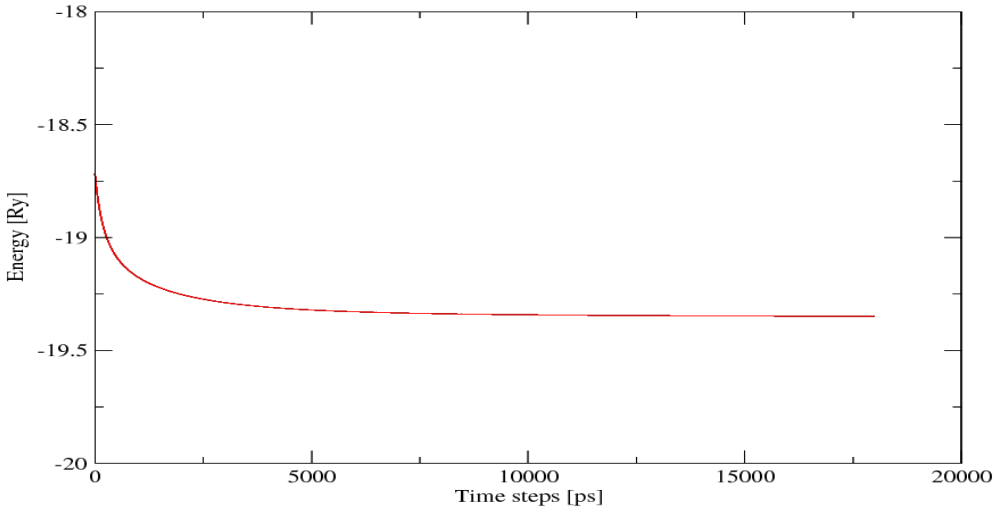


**Figure C.4: The energy dependence of the time steps.**

# APPENDIX D

## PUBLICATIONS

1. *First-Principle Calculations of the elastic constants of the cubic, orthorhombic and hexagonal phases of $BaF_2$*

   *P. W. O. Nyawere*[1,2,3] **, N. W. Makau*[1]*, and G. O. Amolo*[1]

   (Accepted: Physica B: Condensed Matter - October 2013).

2. *Ab-initio calculation of formation and migration energies of intrinsic defects in $BaF_2$*

   *P. W. O. Nyawere*[1,2,3] **, S. Scandolo*[3,4]*, N. W. Makau*[1]*, and G. O. Amolo*[1]

   (Accepted: Solid State Communications - 11th November, 2013).

3. *Molecular Dynamics Simulations of $BaF_2$ by parametrized force field (Under preparation)*

   *P. W. O. Nyawere*[1,2,3] **, S. Scandolo*[3,4]*, N. W. Makau*[1]*, and G. O. Amolo*[1]*.*

# APPENDIX E

## CONFERENCES

1. African School on Electronic Structure Methods - Cape Town South Africa 19th-31st July 2010.

2. African School on Electronic Structure Methods - University of Eldoret 31st May - 9th June 2012.

3. Kabarak International Conference - 2013 - Kabarak University Nakuru 15th - 18th October, 2013